DYNAMIC STALL OF RAPIDLY PITCHING AIRFOILS: MTV EXPERIMENTS AND NAVIER-STOKES SIMULATIONS

By

Charles Paul Gendrich

A DISSERTATION

Submitted to
Michigan State University
in partial fulfillment of the requirements
for the degree of

DOCTOR OF PHILOSOPHY

Department of Mechanical Engineering

1999

Dynamic stall
of attack, α_{ss}. Separat
ary layer's evolution in
the dynamic stall proce
rate have been observe
se in this work three d
low Mach number flow
sented of the flow field
ally constant rate. The
MTV), and an overvie
results.

Previous numeri
velocity, vorticity, and p
experimental results has
distribution or integrated
mismatch between the exp

ABSTRACT

DYNAMIC STALL OF RAPIDLY PITCHING AIRFOILS: MTV EXPERIMENTS AND NAVIER-STOKES SIMULATIONS

By

Charles Paul Gendrich

Dynamic stall occurs when an airfoil is rapidly pitched beyond its static stall angle of attack, α_{ss}. Separation is delayed well beyond α_{ss}, and an understanding of the boundary layer's evolution in the vicinity of the leading edge is essential to an understanding of the dynamic stall process. For uniformly subsonic flows, the dynamic effects due to pitch rate have been observed to outweigh the effects due to Mach number or Reynolds number, so in this work three different pitch rates are investigated using a low Reynolds number/ low Mach number flow. Boundary-layer resolved experimental measurements are presented of the flow field that results when the airfoil's angle of attack increases at a nominally constant rate. These measurements are made using Molecular Tagging Velocimetry (MTV), and an overview of the technique is presented in addition to the experimental results.

Previous numerical simulations of dynamic stall have provided insight into the velocity, vorticity, and pressure fields, but the validation of those simulations against experimental results has typically been restricted to a comparison of the surface pressure distribution or integrated loads. In many cases, validation has also been complicated by a mismatch between the experimental and computational parameters such as Reynolds num-

er or airfoil motic

Navier-Stokes solv

which are essentiall

In both the

ered in this study, a

region of positive vo

ity layer. However,

layer's growth rate.

between the positive

thicken very rapidly.

appears that the high

field is required to pr

Conventional

study were well reso

suggests that the grid

factor of eight before

which are of importan

Dynamic stall

study and debate for r

commonly accepted wa

theless, our experimen

simulations which indi

the frame of reference ro

ber or airfoil motion profile. In the present work a fully-compressible, two-dimensional Navier-Stokes solver is used to simulate the dynamic stall flow field using parameters which are essentially the same as those employed in the experiments.

In both the experimental and computational results for all of the pitch rates considered in this study, a detached shear layer first forms near the leading edge when a thin region of positive vorticity develops underneath the negative vorticity of the initial boundary layer. However, this detached condition does not significantly increase the boundary layer's growth rate. A very small second region of negative vorticity subsequently forms between the positive vorticity zone and the wall, after which the boundary layer begins to thicken very rapidly. Although the initial detached shear layer is absolutely unsteable, it appears that the higher rate of instability amplification present in the three-layer vorticity field is required to produce the formation, growth, and shedding of the dynamic stall vortex.

Conventional grid resolution studies indicated that the computational results of this study were well resolve, but a comparison of the experimental and computational results suggests that the grid resolution in the streamwise direction must be increased by at least a factor of eight before the computations will actually be able to resolve the length scales which are of importance in this flow field.

Dynamic stall is a specific example of unsteady separation, a topic of extensive study and debate for many decades. The Moore-Rott-Sears criterion is perhaps the most commonly accepted way to determine where and when unsteady separation occurs. Nevertheless, our experimental and computational results both agree with previously published simulations which indicate that MRS points do not exist in the dynamic stall flow field if the frame of reference rotating with the airfoil is the correct one.

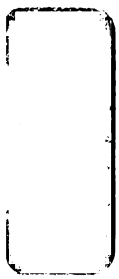

To Jodi and Cindy f

To Jodi and Cindy for giving me the encouragement I needed to complete this project.

You two are the greatest! ☺

ACKNOWLED

As with any

Most heartfelt thank

good friend, mentor,

other members of m

F. Foss and C. Y. Wa

Air Force Base, and

expertise and insight

course of this project

pas mistakes which I

Weber, Sharon Some

schedules to read and

ing mistakes are mos

thoughtfully examine

valuable suggestions

with the final manuscr

Figure 1.3 is co

Figure 4.5 is u

volume 19, copyright

Figures 4.13 an

Ghosh Choudhuri, P.,

Unsteady Leading-Edge

Figure 4.24 is

ACKNOWLEDGMENTS

As with any large-scale project, this work is the result of many people's efforts. Most heartfelt thanks are due to my advisor, Dr. M. M. Koochesfahani, who has been a good friend, mentor, and role model during my tenure in his lab. Thanks, Manooch! The other members of my advisory committee certainly deserve the same recognition: Drs. J. F. Foss and C. Y. Wang at Michigan State University, Dr. M. R. Visbal at Wright-Patterson Air Force Base, and Dr. D. G. Nocera at the Massachusetts Institute of Technology. Their expertise and insightful comments provided me with invaluable assistance throughout the course of this project. Six other people also proofread this manuscript to find the numerous mistakes which I had made. I would like to thank Jodi, Ron, and Jan Gendrich, Burt Weber, Sharon Somerville, and Dr. Ellen Pierce for taking time away from their busy schedules to read and comment on the various revisions of this document — any remaining mistakes are most certainly my fault and not theirs! Richard Cohn and Doug Bohl thoughtfully examined many different versions of the figures in this work and provided valuable suggestions on how to improve them. Rich also provided essential assistance with the final manuscript preparation and submission. Thanks, Rich!

Figure 1.3 is copyright © 1995 AIAA — reprinted with permission.

Figure 4.5 is used with permission from the Annual Review of Fluid Mechanics, volume 19, copyright ©1987, by Annual Reviews.

Figures 4.13 and 4.14 contain data that are used with the authors' permission from Ghosh Choudhuri, P., Knight, D. D., and Visbal, M. R. (1994) Two-Dimensional Unsteady Leading-Edge Separation on a Pitching Airfoil. *AIAA J.* **32**(4): 673-681.

Figure 4.24 is reprinted with the authors' permission from Oshima, H. and

Ramaprian, B. R. (199

119-126.

Mr. Dave Grav

able advice regarding

reated. Mr. Clint Jon

ng the molds themsel

I would also li

ided computational r

9-0417, and F49620-

Engineering Center (N

ber under award numb

Ramaprian, B. R. (1997) Velocity Measurements over a Pitching Airfoil. *AIAA J.* **35**(1): 119-126.

Mr. Dave Graves at AutoAir Composites in Lansing, Michigan provided invaluable advice regarding the design and use of the molds in which our airfoil sections were created. Mr. Clint Jones at Lansing Community College did a wonderful job of constructing the molds themselves. Mr. Todd Brown created the airfoil used in these experiments.

I would also like to acknowledge the support of the U. S. Air Force, which provided computational resources and funding through grants F49620-86-C-0127, AFOSR-89-0417, and F49620-95-1-0391. This work made use of Materials Research Science and Engineering Center (MRSEC) shared facilities supported by the National Science Foundation under award number DMR-9400417.

LIST O
LIST O
LIST O

CHAPT
INTRO
1.1
1.2
1.3
1.4

CHAP
THE E
(MTV
2.1
2.2
2.3
2.4
2.5
2.6

CHAPT
COMPU

TABLE OF CONTENTS

LIST OF TABLES x

LIST OF FIGURES xi

LIST OF SYMBOLS xiv

CHAPTER 1

INTRODUCTION 1

1.1 Experimental Studies 2

1.2 Computational Studies 18

1.3 Unsteady Separation 27

1.4 Contents of the Present Work 34

CHAPTER 2

THE EXPERIMENTAL METHOD: MOLECULAR TAGGING VELOCIMETRY (MTV) 36

2.1 The Chemistry of MTV 41

2.2 Tagging 45

2.3 Detection 50

2.4 Image Pair Analysis 57

2.5 Post-processing 64

2.6 The Experimental Facility 71

CHAPTER 3

COMPUTATIONAL PROCEDURE 80

CHAPTER 4
RESULTS AND DI
4.1 Experimen
4.2 Frame of R
4.3 Measureme
4.4 Computatio
4.5 Pitch-Rate I

CHAPTER 5
CONCLUSIONS AN

REFERENCES . . . .

APPENDIX I
EXPERIMENTAL H

CHAPTER 4

RESULTS AND DISCUSSION 89

4.1 Experimental "Repeatability" 90

4.2 Frame of Reference 95

4.3 Measurements of Dynamic Stall, $\Omega^* = 0.1$ 100

4.4 Computations of the $\Omega^* = 0.1$ Flow Field 110

4.5 Pitch-Rate Effects 122

CHAPTER 5

CONCLUSIONS AND FUTURE WORK 133

REFERENCES 139

APPENDIX I

EXPERIMENTAL HARDWARE OPERATIONAL PARAMETERS 149

Table 1 Beam b
Table 2 Exposu
delay ti
Table 3 Wing a
studies.
Table 4 Initial a
Table 5 Xybion
Table 6 Camera
Table 7 Camera
Table 8 SRS DG
Table 9 Airfoil n

LIST OF TABLES

Table 1 Beam blocker configurations. 55

Table 2 Exposure times, delay times, and change in angle of attack during the delay time for all fields of view and pitch rates. 68

Table 3 Wing aspect ratio and tunnel height-to-chord ratios for nominally 2D studies. 76

Table 4 Initial angle of attack at which a feature is detected. 119

Table 5 Xybion ISG-350-GW3 camera switch settings. 149

Table 6 Camera control unit (CCU) rear panel switch settings. 149

Table 7 Camera control unit (CCU) front panel switch and knob settings. 150

Table 8 SRS DG535 digital delay generator (DDG) parameter settings. 150

Table 9 Airfoil motion control parameters. 151

Figure 1.1 Idealized
tion peri
given Ω
(π/6 and

Figure 1.2 Hydroge
NACA (
sponding

Figure 1.3 Velocity
portions

Figure 1.4 Termina
sel, et al

Figure 2.1 Sample
placed g

Figure 2.2 The cher
CD), the
tional gl

Figure 2.3 Emissio
ited in th
green ph
the addi
phoresc

Figure 2.4 Total ph
differen
CD. . . .

Figure 2.5 The velo
method
velocity
manner.

Figure 2.6 Optical
develop
blocker

Figure 2.7 Typical
beam bl
side-vie
increase
region o

LIST OF FIGURES

Figure 1.1 Idealized constant-pitch rate motion profile. Initial and final acceleration periods are both T_a. T_c is the time required to pitch from 0° to 60° given Ω^* in the limit of inifinite acceleration. The constant multipliers ($\pi/6$ and $90/\pi$) are needed to convert between units properly. 4

Figure 1.2 Hydrogen-bubble flow visualizations of the suction surface on an NACA 0012 airfoil undergoing dynamic stall, $\Omega^* = 0.2$, and the corresponding integrated loads computed as part of the present study 6

Figure 1.3 Velocity fields from the second study of Shih, et al. (1995). Important portions of the near-wall velocity field were not measured. 16

Figure 1.4 Terminal boundary-layer structure schematic (not to scale), after Cassel, et al. (1996). 32

Figure 2.1 Sample experimental MTV grid. (a) just after laser tagging. (b) displaced grid 6 ms later. 37

Figure 2.2 The chemical structure of cyclodextrins. Glucosyl-β-cyclodextrin (gβ-CD), the molecule used in the present study, is a β-CD with an additional glucose added to increase solubility in water..... 42

Figure 2.3 Emission from 1-BrNp in gβ-CD (a) Only blue fluorescence is exhibited in the absence of an appropriate alcohol (ROH); (b) A bright green phosphorescence plus a reduced initial fluorescence is seen upon the addition of ROH, which prevents the quenching of 1-BrNp phosphorescence by O_2. 43

Figure 2.4 Total phosphorescence emission from 1-BrNp · gß-CD · ROH for three different types of alcohol at fixed concentrations of 1-BrNp and gß-CD. 44

Figure 2.5 The velocity at point 1 is $\underline{U}$. Using the line center displacement method gives a lateral velocity estimate $\underline{u}$, with error $\Delta\underline{u}$. The vertical velocity component cannot be estimated with the flow tagged in this manner. 46

Figure 2.6 Optical devices to create patterned illumination: (a) a beam divider as developed by Falco and Chu (1987); (b) an example of one beam blocker configuration. 47

Figure 2.7 Typical laser optics arrangement. Inset shows a region tagged using beam blockers with uniform slot width and spacing. Both top- and side-views are shown of the cylindrical lens arrangement which increases the beam aspect ratio by reducing the beam depth Δz in the region of interest. 49

Figure 2.8
Figure 2.9
Figure 2.1
Figure 2.1
Figure 2.
Figure 2.
Figure 2.
Figure 2
Figure 2
Figure 3
Figure 3
Figure 3
Figure 3

Figure 2.8 2-camera optical arrangement. Both cameras view the same image plane from either side of the test section. Synchronization between the two cameras and the laser is provided by a digital delay generator. 51

Figure 2.9 Electronic interconnections between camera control units (CCUs), digital delay generator (DDG), laser, and airfoil motion controller, plus a diagram showing the timing of events. 54

Figure 2.10 Airfoil target, coordinate directions, and the different regions imaged for each field of view (indicated by Roman numerals). The airfoil is depicted at $\alpha = 0°$; outlines of the airfoil are shown in 5° increments.... 56

Figure 2.11 Spatial correlation technique schematic. (a) Tagged region at time $t = t_1$. (b) Correlation of the source window with one portion of the roam window at time $t_2 = t_1 + \Delta t$; dashed lines indicate the original location of the region, while the shaded region indicates the displaced intersection. The correlation procedure works best when distortions caused by vorticity and strain are negligible during the delay interval Δt. 58

Figure 2.12 Experimental grid intersection. (a) Source window 20 μs after laser pulse. (b) Roam window from an image of the same molecules 6 ms later. (c) Correlation coefficient field. 61

Figure 2.13 (a) Original data measurement locations for one representative angle of attack ($\alpha = 19°$, $\Omega^* = 0.1$). (b) The regular grid onto which those data points are mapped. 66

Figure 2.14 Water tunnel schematic. Locations of the cameras, image plane, and pitch axis are shown in the plan view. Test-section dimensions are given in (cm). 72

Figure 2.15 Airfoil assembly schematic. 75

Figure 2.16 (a) Motion history and (b) pitch rate for all of the experimental data presented in this work. The standard deviation in Ω^* is approximately 0.004 for all three pitch rates once the initial acceleration is damped out. 77

Figure 3.1 Computational grid in the vicinity of the airfoil. Leading-edge and trailing-edge details are also shown. 82

Figure 3.2 The effects of Reynolds number on lift, drag, and moment coefficients..... 84

Figure 3.3 The effects of damping on lift, drag, and moment coefficients. 87

Figure 3.4 Lift, drag, and moment coefficients at $\alpha = 0°$ while computing the steady-state flow field. 88

Figure 4.1

Figure 4.2

Figure 4.3

Figure 4.4

Figure 4.5

Figure 4.6

Figure 4.

Figure 4.

Figure 4

Figure 4

Figure 4

Figure

Figure 4.1 Original measurement locations for two representative angles of attack. The repeatability data plotted in subsequent figures are drawn from narrow bands such as those illustrated here. 91

Figure 4.2 Irregularly-spaced data depicting velocity profiles for when the reversed flow front has reached approximately $\xi = 0.05$. (a) $\Omega^* = 0.1$, $\alpha = 15°$; (b) $\Omega^* = 0.2$, $\alpha = 19.75°$; (c) $\Omega^* = 0.4$, $\alpha = 25.5°$..... 92

Figure 4.3 Unmodified data depicting velocity profiles during the boundary layer eruption which separates the DSV from its feeding vortex sheet. (a) $\Omega^* = 0.1$, $\alpha = 19°$; (b) $\Omega^* = 0.2$, $\alpha = 23.5°$; (c) $\Omega^* = 0.4$, $\alpha = 27°$..... 93

Figure 4.4 Unmodified data depicting velocity profiles from the growth period of the DSV after its initial formation. (a) $\Omega^* = 0.1$, $\alpha = 22°$; (b) $\Omega^* = 0.2$, $\alpha = 28°$; (c) $\Omega^* = 0.4$, $\alpha = 33°$. 93

Figure 4.5 (a) Streamline patterns that define the various critical points in a flow field, and (b) the formation of a closed recirculation region from a vorticity field experiencing non-axisymmetric stretching. (copyright © 1987 by Annual Reviews — reprinted with permission). 97

Figure 4.6 Computational results for $\Omega^* = 0.4$, $\alpha = 36°$. Although the velocity vector field varies only slightly between (a) an inertial frame of reference (x', y') and (b) the rotating frame of the airfoil (X, Y), the streamline patterns vary significantly between those two frames as seen in (c) and (d), respectively. 99

Figure 4.7 Flow visualizations and vorticity field during the initial stages of leading-edge separation. 101

Figure 4.8 Flow visualizations and vorticity field during the growth and convection of the DSV. 103

Figure 4.9 Velocity vectors, tangential velocity and vorticity contours, plus streamline patterns during the initial stages of leading-edge separation. One third of the available vectors are shown. 105

Figure 4.10 Velocity vectors, tangential velocity and vorticity contours, plus streamline patterns during the growth and initial convection of the DSV. One third of the available vectors are shown. 108

Figure 4.11 Convective vorticity flux above the suction surface through the onset of leading-edge separation. 109

Figure 4.12 Computational grid spacings (a) along the airfoil surface, and (b) in the η-direction within a quarter chord of the surface. Dashed lines indicate the corresponding experimental grid sizes. 111

Figure 4

Figure 4

Figure 4

Figure 4

Figure 4

Figure 4.

Figure 4.

Figure 4.

Figure 4.

Figure 4.

Figure 4.

Figure 4.

Figure 4.13 (a, b) Streamline patterns for $\alpha = 14.5°$ based (a) the velocity field as originally computed and (b) the computed velocity field after it has been remapped onto the regularized measurement grid. (c) Computational results from ref. 40 at $\alpha = 15.01°$. In all of these plots, the x-axis scale is approximately 10 times the y-axis scale. 112

Figure 4.14 Vorticity contours and streamline patterns from the present computations and the structured-grid results of Ghosh Choudhuri, et al. (1994)..... 114

Figure 4.15 (a-d) Experimental versus (e-h) computational vorticity fields and streamline patterns. 116

Figure 4.16 Experimentally observed genesis of the dynamic stall vortex. Vorticity contours have the same scale as in figure 4.15. 118

Figure 4.17 Computed vorticity contours after the development of the reversed-flow region but before the onset of leading-edge separation. 124

Figure 4.18 Computed vorticity contours at the formation of the secondary recirculating region..... 125

Figure 4.19 Computed vorticity contours after the onset of leading-edge separation. Vorticity contour levels are the same as in figures 4.17 and 4.18, but a larger field of view is visible in this figure. 126

Figure 4.20 Experimental vorticity field and streamline patters just after the reversed-flow region forms. 128

Figure 4.21 Boundary layer developments just prior to the onset of leading-edge separation. 129

Figure 4.22 Streamlines and vorticity contours at the visually detected onset of leading-edge separation..... 130

Figure 4.23 Formation of the secondary and tertiary recirculation regions (not observed for $\Omega^* = 0.4$). 131

Figure 4.24 Experimental results from Oshima and Ramaprian (1997). 132

LIST OF SYMBOLS

Vector quantities are indicated by an underscore; e.g., see the definition of $\underline{U}$ below.

A	wing surface area
AR	wing aspect ratio, $AR \equiv b/C$
a	speed of sound
α	airfoil angle of attack
$\dot{\alpha}$	pitch rate, $\partial\alpha/\partial t$
α^+	dimensionless pitch rate, $\alpha^+ \equiv \dot{\alpha}\, C/U_\infty = 2\Omega^*$, see below
α_{sep}	angle of attack at which the flow over the leading edge begins to separate
b	wing length
C	airfoil chord length
c	airfoil chord length divided by 1000
C_d	drag coefficient, $C_d \equiv 2(\text{drag force})/\rho U_\infty^2 A$
C_l	lift coefficient, $C_l \equiv 2(\text{lift force})/\rho U_\infty^2 A$
C_m	moment coefficient about the quarter chord
C_p	pressure coefficient, $C_p \equiv 2(p - p_\infty)/\rho U_\infty^2$
$C_{p,\,min}$	magnitude of the suction peak, typically the peak produced by the dynamic stall vortex
$\partial C_p/\partial s$	pressure gradient along the airfoil surface

δ^* displacement thickness, $\delta^* \equiv \int_0^\infty \left(1 - \frac{u}{U_\infty}\right) dy$

δx, δy errors in an x- or y- displacement estimate;
$\delta x \equiv (\Delta x)_{\text{estimated}} - (\Delta x)_{\text{actual}}$, and similarly for δy

δq magnitude of the displacement error, $\delta q \equiv [(\delta x)^2 + (\delta y)^2]^{1/2}$

$(\delta q)_{0.95}$ the 95% confidence interval of δq is defined to be $[0: (\delta q)_{0.95}]$

$D_x(x,y)$, $D_y(x,y)$ apparent displacement due to camera alignment errors; see Section 2.3

$\Delta x, \Delta y$ displacements in the x- and y-directions

Δt 1) computational time step size; 2) the time between earlier and later MTV images; or 3) the time elapsed between two events

e dimensionless acceleration period, $e \equiv (T_a/T_c)$

H test section height

I illumination intensity, $I = I_0\, e^{(-t/\tau)}$, where t is the time since a laser pulse and e is the natural logarithm base.

I_0 initial illumination intensity

k reduced pitching frequency of a sinusoidal oscillation, $k \equiv \omega C/2U_\infty$

λ illumination wavelength

M_∞ freestream Mach number, $M_\infty \equiv U_\infty/a$

p pressure

Re_c Reynolds number based on chord length, $\text{Re}_c \equiv U_\infty C/\nu$

Ω^* dimensionless pitch rate, $\Omega^* \equiv \dot{\alpha} C/2U_\infty$

ω pitching frequency

ω_z vorticity component in the z-direction

t time with respect to the start of an experiment

τ 1) non-dimensional time, $\tau \equiv tU_\infty/C$; 2) decay time constant for a radiative process (see *I* above); or 3) shear stress, $\tau \equiv \partial v/\partial x + \partial u/\partial y$.

T_a time required to accelerate to the desired pitch rate

T_c time required to move from 0^o to 60^o given an infinite acceleration rate

θ (1) local flow direction, $\theta \equiv \tan^{-1}(v/u)$; (2) momentum thickness, $\theta \equiv \int_0^\infty \left(\frac{u}{U_\infty} - \left(\frac{u}{U_\infty}\right)^2\right) dy$

u, v, w velocity components in the x, y, and z directions, respectively

U_∞ freestream velocity

$U_{tan, norm}$ velocity components tangential and normal to the airfoil surface

$|\underline{U}|$ magnitude of the velocity vector, also called $q = |\underline{U}| = (u^2 + v^2)^{1/2}$

X, Y Cartesian coordinates attached to the airfoil. The X-axis is collocated with the mean camber line, and the Y-axis is perpendicular to it, with $Y>0$ passing through the suction surface. $(X, Y) = 0$ at the same place that $(x, y) = 0$.

x, y, z Cartesian coordinate directions in the downstream, vertical, and span-wise directions, respectively. For the NACA 0012 airfoil we define $(x, y) = (0,0)$ to be on the mean camber line one quarter chord from

the leading edge, i.e., at the quarter-chord pitch axis location.

x', y' fixed Cartesian coordinates rotated through an angle of $-\alpha$ with respect to (x, y); see Section 4.2

x_0, y_0 location of the airfoil pitch axis

ξ, η airfoil-fixed coordinates in the surface-tangent and -normal directions, respectively, normalized by the chord length. For the NACA 0012 airfoil we define (ξ, η) = (0, 0) to be at the leading edge; at the trailing edge (ξ, η) are approximately (1.02, 0).

Chapter 1

INTRODUCTION

By the middle of this century, it was recognized that steady airfoil theory could not predict the performance of compressors experiencing rotating stall, airfoils undergoing stall flutter, or helicopter rotors being subjected to the effects of dynamic stall, so accommodations were sought which would allow steady airfoil theories to predict unsteady phenomena. In the 1960's it was widely recognized that new experimental data were required before adequate theoretical predictions could be formulated, and this was the beginning of research into the unsteady separation phenomena which result in dynamic stall. Since then significant progress has been made toward understanding the physical processes associated with rapidly pitching an airfoil beyond its static stall angle of attack. The reviews of McCroskey (1982),[79] Reynolds (1985),[103] Carr (1988),[12] Visbal (1990b),[130] and Doligalski, et al. (1994)[24] summarize much of the current research on this topic. McCroskey (1982)[79] defines dynamic stall as follows:

> Stall flutter refers to oscillations of an elastic body that are caused by separated flow which would be nominally steady in the absence of any motion of the body, but which is made unsteady by the flow-induced body oscillations. The term dynamic stall, on the other hand, usually refers to unsteady separation and stall phenomena on airfoils that are forced to execute time-dependent motion, oscillatory or otherwise, or to cases where flow-field perturbations induce transitory stall. Stall flutter and dynamic stall share many common features; the primary fluid-dynamic difference is that the amplitude of the motion is often smaller in stall flutter.

Dynamic stall is observed in helicopters when large movements of the cyclic and

collective controls cause the rotor blades to exceed their static stall angle of attack during some portion of the rotational period. Dynamic stall can also be produced over compressor and fan blades in turbine-powered aircraft as a consequence of large excursions in angle of attack that result from variations in the velocity vector over the area of the engine inlet. The many complex and interacting phenomena which produce unsteady separation have made this a difficult subject to investigate theoretically, numerically, or experimentally; consequently, it remains an important topic of basic and applied research to this day.

1.1. Experimental Studies

Since very early investigations into dynamic stall were concerned with the cyclic phenomena mentioned above, those studies dealt with airfoils undergoing sinusoidal oscillations. The parameters of importance for those motions are the reduced pitching frequency, $k \equiv \omega C/2U_\infty$; the mean angle of attack, α_0; and the amplitude of the pitching cycle, $\Delta\alpha$. The angle of attack, α, varies in time according to: $\alpha(t) = \alpha_0 + \Delta\alpha\sin(\omega t)$. Studies involving helicopter rotors must also consider the effects of plunge and heave, plus the effects of a periodic variation in the freestream velocity, because the rotor flexes and experiences a constantly varying relative wind when the helicopter is in forward flight. Additionally, the interactions between the various effects also need to be investigated. The complete parameter space for the oscillating airfoil problem is truly immense!

Airfoil shape is another factor which must be considered. In 1982 McCroskey, et al.[81] published an experimental study of seven different airfoils undergoing oscillatory motions. Regarding their use of the NACA 0012 airfoil, they wrote, "The NACA 0012

served primarily as a standard reference section; the six modern helicopter sections were chosen as representative of contemporary designs from several different companies and research organizations." Despite the fact that the NACA 0012 was a *de facto* standard, many researchers decided to use NACA 0015 airfoils in their experiments because its increased thickness and more gradual leading edge curvature provided more space inside the airfoil for pressure taps and transducers. Nevertheless, Cebeci, et al.[14] wrote in 1995, "(The NACA 0012) airfoil was the standard helicopter airfoil during the early period of development of helicopters and has become a benchmark for comparison of computation and experiment." Since one of the purposes of this work is to produce a set of computational and experimental data for comparison, the NACA 0012 airfoil section was used for the present study.

At about the time of McCroskey's 1982 review,[79] constant pitch-rate motions started to receive a great deal of attention because of their potential applications to super-maneuverable aircraft. In constant pitch-rate studies the airfoil is initially at rest at $\alpha = 0$. The motion ideally consists of an initial acceleration period until the desired pitch rate is attained, then the airfoil continues to pitch at that rate until a large angle of attack is reached (typically $\alpha = 60°$). At this point it is brought to rest, see Figure 1.1. As with the "deep dynamic stall" case of the sinusoidal motions initially studied, the flow is observed to remain attached until well beyond the static stall angle of attack; then at some point the flow near the leading edge begins to separate, and a large vortex is observed to form and convect downstream. The dynamic stall vortex (DSV) produces a strong suction peak ($C_{p,min}$) on the upper surface of the airfoil, and as long as that suction is present, the levels of lift produced are much higher than those obtained in the static case.

Fig. 1.

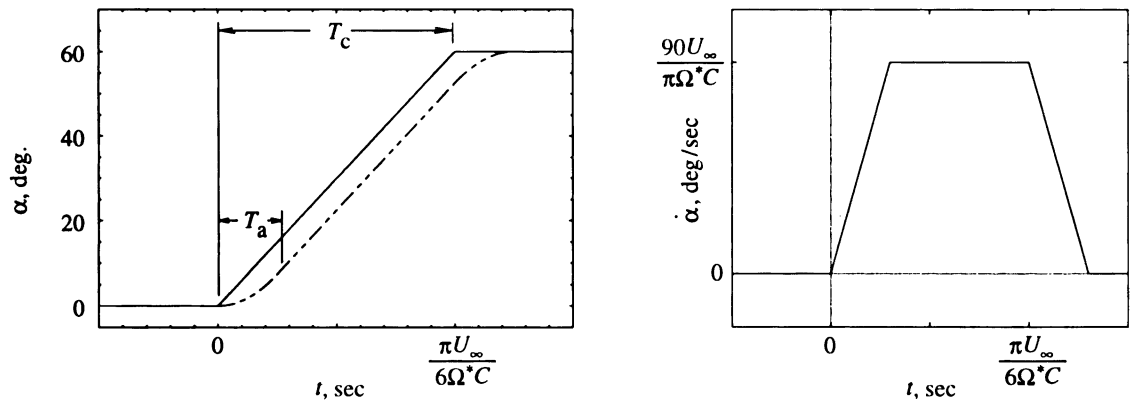

Fig. 1.1: Idealized constant-pitch rate motion profile. Initial and final acceleration periods are both T_a. T_c is the time required to pitch from 0° to 60° given Ω^* in the limit of infinite acceleration. The constant multipliers ($\pi/6$ and $90/\pi$) are needed to convert between units properly.

For these motions a non-dimensional pitch rate, $\Omega^* \equiv \dot{\alpha}C/2U_\infty$, has been introduced as the principal governing parameter; $\dot{\alpha} \equiv \partial\alpha/\partial t$ refers to the pitch rate during the constant pitch-rate period, C represents the airfoil chord, and U_∞ is the freestream speed. Because the present work deals extensively with dimensions that are much smaller than the airfoil chord length, C, we will use the symbol c to refer to one thousandth of a chord, $c \equiv C/1000$. Although one might initially consider the duration of the acceleration period at the start of the motion to be an important parameter, it has been demonstrated by Koochesfahani and Smiljanovski (1993)[68] and Gendrich, et al. (1995)[38] that as long as the acceleration period ends at least a short time before leading-edge separation begins, the precise details of that acceleration have very little effect on the dynamic stall process (see also Chapter 3). Since this is the case, it is possible to use constant pitch-rate motions to study the dynamic stall process as a function of one parameter (Ω^*) instead of many (k, α_0, $\Delta\alpha$, etc.).

It should be noted that a number of parameters are common to the oscillatory and constant pitch-rate studies, including Reynolds number, Mach number, airfoil shape, and

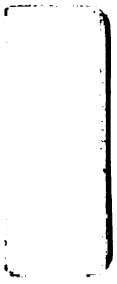

pitch axis. Additionally, if the initial angle of attack is non-zero, it can also be a factor, especially if it is close to the static stall angle of attack. While the constant pitch-rate motion profile simplifies the problem, it does not reduce it to a single-parameter study.

Figure 1.2 depicts a hydrogen-bubble flow visualization of the suction surface on an NACA 0012 airfoil as it undergoes the constant pitch-rate dynamic stall process, in addition to lift, drag, and moment time histories computed using the method outlined in Chapter 3. To date investigators have studied a wide range of pitch rates, with Ω^* values from 10^{-3} to 0.5. In the present work we will restrict ourselves to the upper part of that range, $0.1 \leq \Omega^* \leq 0.4$; the pitch rate in Figure 1.2 is 0.2. In that figure no signs of separation are seen at $\alpha = 12^o$, the static stall angle of attack for the NACA 0012 airfoil ($\alpha_{s.s.}$). Between 12° and 18°, the boundary layer thickens significantly over more than 95% of the suction surface. Near the leading edge the maximum boundary layer thickness increases from approximately $20c$ to $45c$ (i.e., $20 \times 10^{-3}C$ to $45 \times 10^{-3}C$), while at mid-chord it grows from approximately $10c$ to $20c$, and near the trailing edge it remains constant at about $85c$. At $\alpha = 18.3°$ we see a disturbance near the leading edge pinching off the boundary layer, and this is the start of a disturbance that rapidly propagates downstream. By 28° the rolled-up shear layer has split into two separate regions, a collection of small shear layer vortices over the aft half of the airfoil and a large, coherent vortical structure near the leading edge that continues to grow and accumulate circulation. Ultimately this body of fluid becomes what researchers refer to as the dynamic stall vortex (DSV).

The core of the DSV is a region of very low pressure, the effects of which dominate the pressure field on the suction surface of the airfoil. While the DSV remains near the leading edge, lift continues to increase with angle of attack. After a time, however, the

DSV begins to convect downstream (at about 0.35 U_∞, see ref. 42), and once its effects no longer influence the airfoil, an abrupt and powerful loss of lift and shift in pitching moment occurs.

Similar to the "light dynamic stall" and "deep dynamic stall" cases noted in oscillatory investigations, Acharya and Metwally (1990)[2] have observed two different pitch

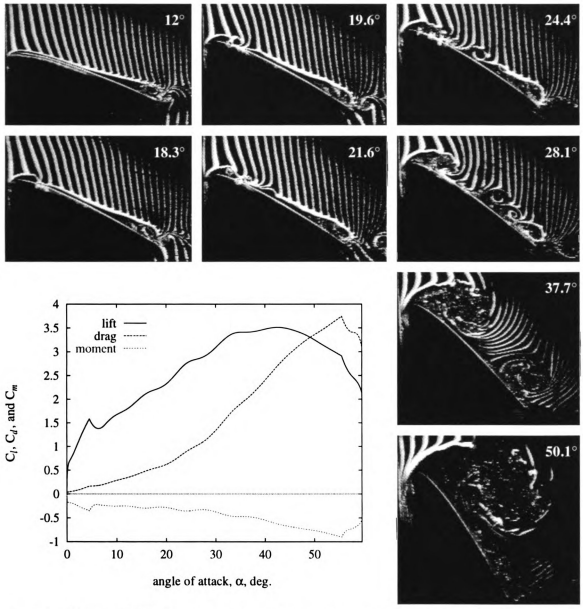

Fig. 1.2: Hydrogen-bubble flow visualizations of the suction surface on an NACA 0012 airfoil undergoing dynamic stall, $\Omega^* = 0.2$, and the corresponding integrated loads computed as part of the present study.

rate regimes in which the dynamic stall effects are radically different. The "class A" or low pitch rate regime is characterized by a small DSV and correspondingly weak variations in lift, drag, and moment. In the "class B" or high pitch rate regime, the onset of leading edge separation is delayed significantly beyond $\alpha_{s.s.}$; a strong and coherent dynamic stall vortex forms; and large fluctuations are observed in the integrated loads, especially the lift and moment coefficients. The present work is concerned with high pitch-rate motion profiles which fall well above the lower bound of Acharya and Metwally's[2] class B motions.

Many investigators have studied the constant pitch-rate dynamic stall process experimentally using a range of pitch rates similar to those which will be considered in the present work. At first, global parameters such as lift, drag, and moment were measured directly using load sensors (see, for example, Carr and McAlister, 1983[11]), but researchers quickly realized that such data quantify the gross effects of dynamic stall but not what or why those effects occur. The next development was, therefore, the use of pressure taps to measure the pressure field at many points along the surface. Symmetric airfoils like the NACA 0012 continued to be used so that models could be pitched both up and down, enabling pressure and suction surface measurements to be made without having to instrument two sides of the airfoil. Such a study was conducted by Francis and Keesee[32] in 1985, using 19 pressure taps and stepper motors to control the angle of attack. The Reynolds number in that study was 85,000. A similar study was performed by Graham and Strickland (1986),[41] whose Reynolds number values were 100,000 and whose angle of attack varied between 0° and 90°. The ultimate in surface pressure spatial resolution was achieved by Reda[102] in 1991 using a liquid crystal coating to measure the pressure field

over the

techniq

betweer

Strickla

was tha

pitch ra

angle o

can be

tions.

pitch a

attack r

layers,

bounda

Althou

has bee

et al. [3

numbe

observe

especia

Carta

ized ab

over the entire surface of an airfoil oscillating in pitch. Unfortunately the liquid crystal technique has never been applied to study the constant pitch-rate dynamic stall problem.

Helin and Walker (1985)[47] were among the first to investigate the relationship between the pitch rate and the location of the pitch axis. This study was echoed in 1986 by Strickland and Graham[119] and in 1989 by Jumper, et al.[59] The conclusion of those studies was that moving the pitch axis aft of the quarter chord caused an increase in the effective pitch rate. In addition Graham and Strickland (1986)[41] demonstrated that the effective angle of attack at the nose, which is a function of both pitch rate and pitch axis placement, can be used to compare results derived from experiments with different pitch axis locations. The computational study of Visbal and Shang (1989)[133] showed that any arbitrary pitch axis location can be combined with the pitch rate to produce an effective angle of attack relative to any other pitch axis location regardless of the airfoil section used.

Unless tripped, low Reynolds number flows have laminar or transitional boundary layers, and this was expected to result in a sooner and more abrupt breakdown of the boundary layer when compared to the more stable fully turbulent boundary layer. Although flight Reynolds numbers are typically 10^6 and higher, a great deal of research has been done with Reynolds numbers as low as 5,000. A very important study by Walker, et al.[136] in 1985 addressed growing concerns about the applicability of low Reynolds number dynamic stall experiments. For a wide range of pitch rates, $0.025 \leq \Omega^* \leq 0.3$, they observed that the Reynolds number had a very limited effect on the surface pressure field, especially when compared to the effects of the pitch rate itself. In 1988 Lorber and Carta[73] published the first constant pitch rate pressure measurements from 36 taps distributed about an SSC-A09 airfoil (used for helicopter rotors) at "realistic combinations of

Reynolds and Mach numbers." The results from this low pitch-rate study, $0.001 \leq \Omega^* \leq 0.02$, were seen not to vary a great deal from previous low Reynolds number experiments, as long as the high Re_c flow remained subsonic throughout. In a dual study using a whole-field interferometric technique, Wilder, et al. (1993)[138] and Chandrasekhara, et al. (1993)[15] quite effectively addressed the effects of transition and compressibility on class A constant pitch-rate motions, concluding that as long as the entire flow remained subsonic (e.g., $M_\infty < 0.2$, so that $M_{max} < 1$), compressibility effects were quite limited. Furthermore, as long as the compressibility effects were small, transition played no role in the development of the dynamic stall flow field. They even noticed that the opposite effect sometimes occurred, i.e., that the stall was accelerated instead of being delayed by an earlier transition to turbulence.

McAlister and Carr (1978)[78] measured the unsteady pressure field of an oscillating NACA 0012 airfoil while visualizing the flow with hydrogen bubbles. Koochesfahani's group (Smiljanovski, 1990[114]; Brown, 1992[10]; and Koochesfahani and Smiljanovski, 1993[68]) used a combination of dye and hydrogen bubbles to visualize how the entire dynamic stall flow field changed as a function of pitch rate and the initial acceleration period. The Reynolds numbers were low (between 8,000 and 20,000), but their conclusions supported existing surface pressure measurements, indicating that the onset of leading edge separation was delayed at higher pitch rates and that the instantaneous pitch rate was the most important parameter governing when boundary layer breakdown occurred. As mentioned earlier, the initial acceleration was found not to affect when or how dynamic stall occurred, as long as that acceleration period had ended some time ($\Delta\tau \geq 0.25$) before leading edge separation began.

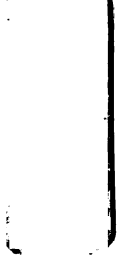

Acharya's group pursued a combination of surface pressure measurements in conjunction with smoke wire flow visualizations to extend their knowledge of the constant pitch-rate dynamic stall process beyond the surface and into the flow field. Although visualizations such as those in Figure 1.2 had showed that the boundary layer thickens with angle of attack, they revealed very little about the motions within the boundary layer itself. Karim and Acharya (1991)[61] and (1994),[62] in a study with Reynolds numbers ranging between 30,000 and 118,000, employed smoke from a wire affixed to the airfoil to visualize this region. Excellent visualizations were produced, which clearly depicted the development of the dynamic stall vortex and hinted at the presence of a very thin region of reversed flow near the surface at the leading edge. Computations of the dynamic stall flow field (to be discussed later) had indicated the presence of such a reversed-flow region, but integrated loads and surface-based measurements were incapable of confirming its existence. A number of other research groups have also attempted to detect this reversed-flow region, which was thought to play an important role in the unsteady leading-edge separation process. Smoke wires were used by Helin and Walker (1985),[47] Acharya and Metwally (1990),[2] Karim and Acharya (1991),[61] and Huang and Lin (1995)[53] to visualize regions of flow reversal. Surface-mounted or near-surface sensors have also been deployed at a couple of points along the suction surface. McAlister and Carr (1978)[78] were the first to use surface-mounted hot films in conjunction with their surface pressure measurements and hydrogen bubble flow visualizations. Helin and Walker (1985)[47] are the only authors to publish data from several hot films suspended 2 mm above the surface of their airfoil in an attempt to make near-surface velocity measurements. Lorber and Carta (1988)[73] and Leishman (1990)[69] used surface-mounted hot films to detect flow

reversals.

Some authors have attempted to use integrated loads, surface pressure, and/or flow visualizations to develop methods to prevent or control the dynamic stall process. Modi, et al. (1981)[86] replaced the leading edge of their NACA 63-218 airfoil with a cylinder. They were able to prevent dynamic stall and achieve large values of lift at high angles of attack by spinning the cylinder very rapidly. Carr and McAlister (1983)[11] considered the performance of a VR-7 airfoil, which they modified by adding a backwards-facing step at $x/C = 0.3$ or vortex generators at $x/C = 0.2$ or a leading-edge slat. The step and vortex generators had no effect on the dynamic stall process, but the slat completely suppressed the dynamic stall vortex for oscillatory motions with $\alpha_{max} < 30°$. Concluding that only leading-edge effects had a significant impact in regulating dynamic stall, Karim and Acharya (1994)[62] investigated leading-edge suction magnitude and timing, slot size, and slot location for constant pitch rate motions with $0.036 \leq \Omega^* \leq 0.16$ and $\alpha_{max} = 45°$. Alrefai and Acharya (1996)[4] extended this study to lower pitch rates, $\Omega^*_{min} = 0.003$, applying suction only at $x/C = 0.02$. Both of these studies concluded that if sufficient suction was applied, the signature of the dynamic stall vortex could be eliminated from the surface pressure field up to any desired angle of attack within the range which they considered. Yu, et al. (1995)[141] investigated a fixed leading-edge slat, a drooped leading edge, and blowing, concluding that none of these devices were conclusively better than the others.

From a basic physics perspective the foregoing studies indicate that a thorough understanding of the flow field near the leading edge is crucial to the formulation of an optimal method to reduce or eliminate the effects of dynamic stall. Probes fixed in space cannot be employed to measure this near-wall flow because the moving airfoil would

impact the motionless probe. Probes affixed to the surface of the airfoil are intrusive, difficult to reposition for measurements from various locations, and generate data which cannot be interpreted without extremely precise knowledge of the airfoil's location and velocity at all instants in time. Laser-Doppler Velocimetry (LDV) could be used to obtain 1-, 2-, or 3-component velocity measurements at individual points non-intrusively, but it would require a Herculean effort to probe enough different locations over enough runs to generate a statistically significant representation of the dynamic stall flow field. Furthermore, there are difficulties associated with using particles to measure this flow field (discussed below).

Several research groups have attempted to use simultaneous multi-point non-intrusive techniques to measure the (u,v)-velocity field around an airfoil undergoing dynamic stall, unfortunately without any special efforts to resolve the leading-edge flow field. In addition to the pulse-diffraction interferometric technique of Chandrasekhara and his coworkers (refs. 15, 126, and 138), Particle Image Velocimetry (PIV) has been applied by three different research groups to study the dynamic stall process. However several difficulties must be overcome before particles can be used successfully to accurately measure the unsteady separating boundary layer. Experimental uncertainties associated with measuring flows using particles have been investigated by Adrian (1991),[3] Thomas, et al. (1993),[121] Lourenco and Krothapalli (1995),[74] Leishman (1996),[70] and others. The two most serious problems as far as dynamic stall measurements are concerned involve the difficulty in getting an acceptable particle density in the boundary layer, other highly vortical regions, and the freestream simultaneously, plus the fact that the movement of a particle differs from that of the surrounding flow field in the presence of strong velocity or pres-

sure

with

ticle

$\frac{dy}{dt}$

wi

an

In th

ertie

$\Delta y =$

due

the f

part

neg

of th

the p

that

it is

ideal

the

part

sure gradients and/or unsteady drag forces.

A consideration of the forces on a particle illustrates these difficulties. If we start with the derivation of Thomas, et al.[121] and assume Stokes flow over non-interacting particles, the drag coefficient on a particle will equal $24/\mathrm{Re}_D$ to first order, and we can write:

$$\frac{d\underline{u}_P}{dt} = \frac{18\mu_F}{d^2\rho_p}\Delta\underline{u} - \frac{1}{\rho_p}\nabla p + \frac{1}{2}\frac{\rho_F}{\rho_P}\frac{\partial}{\partial t}\Delta\underline{u} + \frac{9}{\pi d}\sqrt{\pi\rho_F\mu_F}\int_0^t \frac{\frac{\partial}{\partial t}\Delta\underline{u}}{\sqrt{t-\tau}}d\tau - \Delta\rho\underline{g} \qquad (1)$$

where $\Delta\underline{u} = \underline{u}_F - \underline{u}_P$ (2)

and $\Delta\rho = \rho_F - \rho_P$ (3)

In these equations the subscript F refers to the properties of the fluid, P refers to the properties of a particle, d is the diameter of a particle, and $t = 0$ is the most recent time when $\Delta\underline{u} = 0$. The first forcing term models the viscous drag on the particle; the second term is due to pressure gradients within the flow field; the third term is an apparent mass effect; the fourth term is the Basset history integral; and the fifth term is due to buoyancy of the particle. For typical particles in most flows, the history and buoyancy terms can be neglected (Adrian[3] and Thomas, et al.[121]).

As seen in Equation (1), the more massive a particle, the less it accelerates because of the forces acting on it; the viscous drag term is particularly sensitive to the diameter of the particle, varying inversely with d^2. Furthermore, when a particle's density varies from that of the surrounding fluid, the pressure gradient's effect is different on the particle than it is on the fluid (and the buoyancy term is non-zero). From a response perspective, the ideal particle has the same density as the fluid and the smallest possible diameter; on the other hand, the larger a particle is, the easier it is to detect. The researcher must choose the particle's density and mean diameter to meet the response requirements of a particular

experiment.

Neglecting all but the viscous drag term, Adrian[3] computes that the slip velocity, Δu, of typical particles in planar regions of strong shear is about 4% of the velocity change across the shear layer. Thomas, et al. (1993)[121] present a model of the variation in average and RMS velocity measurements because of finite particle size in the presence of large velocity gradients, and as expected, the variation increases with the square of the average particle diameter. Leishman (1996)[70] documents the errors associated with using 0.6 μm particles to measure the velocity of air inside wing-tip vortices induced by helicopter rotor blades. He notes that pressure gradients and high levels of centripetal acceleration cause fewer particles to be present within a vortex core, and these problems are exacerbated when smaller models are used, as a result of the higher spatial gradients.

Raffel, et al. (1995)[101] used PIV to study dynamic stall over an oscillating airfoil. The first PIV study of the constant pitch-rate dynamic stall flow field was published by Shih, et al. in 1992[113] along with a follow-up article in 1995![112] In those studies an NACA 0012 airfoil with an aspect ratio of 5.5 was pitched about its quarter chord from 0° to 30° in a water towing tank after an impulsive start followed by one chord's travel at $\alpha = 0°$; it was implicitly assumed that the flow field had achieved a steady state before the pitch-up motion began. The pitch rate was $\Omega^* = 0.066$, and the Reynolds number was 5,000 in both of the studies. Film was used to record two exposures of 11 μm particles with a specific gravity of $\rho_p = 2.6$ on each frame, and in order to prevent problems with directional ambiguity, an optical shift was applied to the second exposure by a rotating mirror to produce unidirectional velocity vectors. A focused laser beam interrogated the film, producing Young's fringes which were automatically converted to velocities. The

interrogation region had an effective diameter of $6.25c$ (i.e., $6.25 \times 10^{-3}C$) for both studies; in the 1992 study[113] the step size was $12.5c$, while the step size was reduced to $5.0c$ (less than the probe diameter) for the 1995 study![112]

Their 1% accuracy estimate is a best-case value based on "towing the camera carriage at a constant speed," i.e., in the absence of any particle motion, unsteady or vortical velocity fields, or pressure gradients in the tow tank itself. However, these unsteady effects were all present during their dynamic stall experiments, producing reductions in accuracy caused by the particle motion and analysis method, as discussed above and by Lourenco and Krothapalli (1995),[74] respectively.

Shih, et al.[112,113] are the only authors to note high run-to-run variability in their results, based primarily on the development of post-DSV isovorticity contours. The velocity fields which they present are the result of phase-averaging multiple runs. Some of those results from their 1995 paper are shown in Figure 1.3. The features in these plots are larger than those in the visualizations of Figure 1.2, because of the lower pitch rate and lower Reynolds number. Although not apparent from Figure 1.3, Shih, et al.[112,113] attempted to capture the entire flow field with each image, rather than imaging smaller portions of the airfoil separately to obtain better resolution in critical regions. Consequently neither the 1992 nor the 1995 study has sufficient spatial resolution to capture the near-wall features which the present study shows to be an essential part of the dynamic stall process. Since an understanding of the near-wall flow field close to the leading edge appears to be very important component of the dynamic stall process, and since that leading-edge region is the focus of this work, the studies of Shih, et al.[112,113] appear not to be suitable for comparison with the present work.

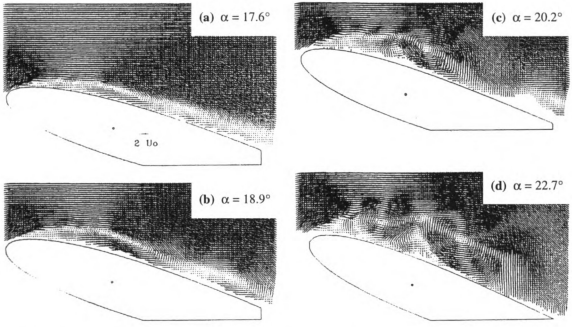

Fig. 1.3: Velocity fields from the second study of Shih, et al.[112] (copyright © 1995 AIAA — reprinted with permission). Important portions of the near-wall velocity field were not measured.

One of the most thorough studies of the constant pitch-rate dynamic stall process was recently undertaken by Ramaprian's group at Washington State University. Conger and Ramaprian (1994)[19] performed pressure measurements at 41 taps over the surface of their NACA 0015 airfoil with pitch rates in the range of $0.018 \leq \Omega^* \leq 0.1$ and Reynolds numbers between 52,000 and 220,000. Their data supported the conclusions of Wilder, et al. (1993)[138], i.e., that Reynolds number effects were extremely limited, at least up to the point when the dynamic stall vortex began to form. On the other hand, they did note a strong Reynolds number dependence in the magnitude of the DSV suction peak, $C_{p,min}$, but this might be attributable to the high level of blockage in their tunnel at those angles of attack (e.g., 17% at 30°). Although the flow over their airfoil was more likely to experience three-dimensional effects related to the low aspect ratio of the model ($AR = 2$, see Table 3, p. 76) and a gap between one end of the airfoil and the tunnel side wall, in fact the

flow field remained very two dimensional and extraordinarily repeatable, at least up until the inception of the dynamic stall vortex.

At the same time and in the same facility as Conger and Ramaprian's surface pressure study,[19] Oshima and Ramaprian (1997)[92] measured the velocity field in the vicinity of the pitching airfoil using PIV. Velocity fields were measured for one pitch rate, $\Omega^* = 0.036$, and three different Reynolds numbers, $Re_c = 18{,}000$, 54,000, and 150,000. Three different fields of view were photographed in order to obtain better near-surface and near-leading edge resolution. Unfortunately, they elected to switch from the 2 μm particles used for the $Re_c = 18{,}000$ study to 30 μm particles for the higher Reynolds number flows, thereby significantly increasing errors caused by unsteady effects. (Their particle densities were unreported, so it is not possible to quantify those errors here.) Nonetheless, a growing region of separated flow was detected for all Reynolds numbers, expanding from the trailing edge toward the leading edge. Although they report that the topological developments for their $\Omega^* = 0.036$ experiment were quite similar to what Ghosh Choudhuri, et al. (1994)[40] had computed for a much higher pitch rate, $\Omega^* = 0.1$, they did not see the reversed-flow region expanding to cover most of the suction surface before the DSV began to form. This contradicts the experimental observations of Karim and Acharya (1991),[61] Shih, et al.,[112,113] and the computations of Ghosh Choudhuri, et al.[40] and Gendrich, et al. (1995).[38] This may, however, be a result of the very early transition to turbulence in Oshima and Ramaprian's study, which they attribute to a 1.5% freestream turbulence intensity and externally imposed unsteadiness. Based on their observations, those researchers concluded that a thin reversed-flow region near the leading edge is <u>not</u> a proximate cause of the DSV formation. The results of the present work (Chapter 4) indi-

cate the existence of this reversed-flow region for all pitch rates.

1.2. Computational Studies

Computations have long been used in conjunction with experimental results to provide insight into the physics of a problem and to predict the performance of a design on the basis of limited experimental data. In the case of dynamic stall, computational efforts have focussed especially on Reynolds number and Mach number effects, and those studies have provided data which have been difficult or impossible to obtain experimentally. As noted above, whole-field measurements of the dynamic stall process are scarce. In fact the only computations which have compared against whole-field measurements are those of Van Dyken, et al. (1996)[126] and Shih, et al. (1992); every other computationalist has had to rely on integrated load and/or surface pressure measurements for comparison purposes.

A great many algorithms have been developed to model viscous flows around two- and three-dimensional bodies. The simplest models solve the inviscid equations of motion for the flow field outside of the near-wall viscous layer, while using boundary-layer assumptions to simplify the Navier-Stokes equations and make the near-wall solution tractable. The difficulty with using this approach is that the boundary-layer assumptions do not hold when the flow undergoes separation. Theoretical investigations into unsteady separation in the mid-1950's employed these models, although the performance of an airfoil was typically predicted using circulation-based models that required knowledge about where the flow was and wasn't attached. Sears (1956)[109] gives a good review of the unsteady airfoil theory of that time. The use of these methods continues to the present day

for approximating the performance of airfoils at fixed angles of attack in low and high Reynolds number flow fields; for example, Cebeci, et al. (1995)[14] have developed an interactive boundary-layer method to estimate the performance of NACA 0012 airfoils at fixed angles of attack, and their results agree well with experimental measurements of lift, drag, skin friction, and surface pressure.

Several different vortex methods have been developed, especially for use in simulating two-dimensional external flows. Shih, et al. (1992)[113] used a discrete vortex, random walk statistical method to produce computations which corresponded to their experimental measurements. Unfortunately their computational results had "typical random fluctuations of 10%" which, coupled with the lack of supporting near-wall experimental data, adversely impacts the significance of their results. Lin, et al. (1997)[72] divided their NACA 0015 airfoil surface into 80 panels, from which up to 4,000 vortices were released and convected through the wake. One significant advantage to this grid-free approach is that computations only need to be performed at the surface points and at the center of each vortex. One must, however, correctly model the surface vorticity distribution and decide when, where, and how strong each vortex is as it is released from the surface. The results from the study of Lin, et al. (1997)[72] compare fairly well with the corresponding experimental measurements of normal force and moment coefficient, and they were achieved using a fraction of the computational resources required for a full Navier-Stokes simulation.

The thin-layer simplification of the Navier-Stokes equations has sometimes been applied to simulations of the flow field around lifting bodies; in static cases it appears to do reasonably well, but dynamic cases are more problematic. For example, the thin-layer

method was applied by Degani and Marcus (1997),[23] who indicate that it produces results which are just as good as a full Navier-Stokes computations when used to simulate an ogive at fixed high angles of attack. It has also been applied by Van Dyken, et al. (1996)[126] in a joint computational and experimental effort to study the oscillating airfoil dynamic stall problem. Unfortunately their computational results did not always agree very well with the corresponding whole-field experimental measurements, especially on the down stroke during times of peak velocity and the formation of the dynamic stall vortex. In that study the freestream Mach number was 0.3, so turbulence and compressibility certainly influenced the experimental flow field as indicated by Chandrasekhara, et al. (1993),[15] requiring a good turbulence model and a well-refined grid to resolve the embedded shocks.

In 1986 Wu, et al.[140] used a vorticity formulation of the Navier-Stokes equations to compute the constant pitch-rate dynamic stall problem with $\Omega^* = 0.08$ and 0.09. Their simulations did not compare very favorably with the experimental pressure measurements of Francis and Keesee (1985),[32] indicating the need for increased grid resolution and an improved computational method.

Visbal and his co-workers were among the first to attempt a simulation of the constant pitch-rate dynamic stall problem using the fully compressible two-dimensional Navier-Stokes equations. Details of the numerical implementation are presented in Visbal (1986a),[127] while time step, artificial damping, grid resolution issues, and acceleration effects are discussed in Visbal (1986b).[128] Visbal and Shang (1989)[133] presented additional grid resolution studies plus a comprehensive analysis of the flow field around an NACA 0015 airfoil with $Re_c = 10{,}000$ and $M_\infty = 0.2$ pitching at $0.05 \leq \Omega^* \leq 0.3$ with pitch

axes in the range $0 \leq x_0/C \leq 0.75$. Similar to what is observed experimentally, higher pitch rates delayed the onset of leading-edge separation and resulted in a more abrupt stall with smaller structures forming nearer to the leading edge. Visbal (1991)[131] wrote that "the DSV is seen to start from the roll-up of the shear layer created by the appearance of the thin reversed-flow region. The vortex is not initiated in this case by the growth or burst of a separation bubble nor by the sudden eruption of fluid from the wall." In other words, their computations supported the view that the presence of the thin reversed-flow region was essential to the dynamic stall process because of the instabilities inherent in the resulting shear layer. Chapter 4 reveals that this thin reversed-flow region is present before the onset of leading edge separation for all of the pitch rates investigated, both computationally and experimentally.

Gendrich, et al. (1992)[37] added the ability to track "virtual hydrogen bubbles" to Visbal's code, enabling more direct comparisons to be made between computations and experimental flow visualizations of hydrogen bubbles. The visually detected onset of leading-edge separation was found to agree to within about 2.5°, with the experimental detection consistently occurring prior to the computational one. In addition, the size of the boundary layer and the movement of dye injected near the trailing edge just before the pitch-up maneuver all agreed quite well until the DSV began to form. At that point, the size of the computational structures was found to grow significantly faster and larger than was observed experimentally.

One problem faced by every computationalist is that of matching the simulated motion profile either to the ideal case ($T_a \rightarrow 0$ in Figure 1.1) or to an experimentally measured profile. The ideal profile, with its instantaneous transitions between the motionless

and moving states, has discontinuities in the first derivative of α. Even the idealized real profile, with $T_a \neq 0$, has a discontinuous acceleration history. Although all of the derivatives are continuous in experimentally measured motion profiles, those profiles are difficult to represent analytically. In order to have a motion profile without discontinuities in the angle of attack or its derivatives, an exponential acceleration profile was chosen by Visbal (1986a,[127] b[128]) even though this did not correspond to the motion profiles produced by any experimental apparatus. Gendrich, et al. (1995)[38] modified Visbal's code to use a constant acceleration profile, corresponding to the experiments of Koochesfahani and Smiljanovski (1993),[68] and it was found in all cases that the effects of the acceleration period only lasted until a short time after the acceleration had ended, regardless of the specifics of the acceleration used.

Ghosh Choudhuri, et al. (1994)[40] compared an implicit unstructured grid approach to the results of Visbal's structured grid solver, employing considerably finer resolution than Visbal (1991)[131] had been able to achieve because of computer limitations at that time. Again, the flow conditions were taken to be $Re_c = 10{,}000$ and $M_\infty = 0.2$, but this time an NACA 0012 airfoil was pitched at $\Omega^* = 0.1$. At higher levels of resolution, the two computational approaches produced practically identical results, and the bulk of reference 40 is devoted to a study of the streamline patterns and isovorticity contours as viewed in a frame of reference rotating with the airfoil. Initially only one sign of vorticity is seen over practically the entire suction surface, but the aforementioned thin region of reversed flow grows from the trailing edge as the airfoil pitches up to cover 93% of the upper surface at $\alpha = 14.5°$. By $\alpha = 15°$ two new critical points (see also Section 1.3) have formed inside the upper region of vorticity, one of which becomes the center of the DSV. The

authors comment briefly on the formation of secondary and tertiary recirculating regions underneath the primary one, noting that:

> ... a three-layer structure appears near the wall. The bottom layer near the wall has forward flow. The intermediate layer has reversed flow, whereas the top layer has forward flow. The formation of the secondary recirculating region precedes the sudden ejection of the particles in a direction approximately normal to the airfoil surface, which indicates the boundary-layer separation.

Although they detect the tertiary recirculating region, a very thin near-wall region of vorticity having the same sign as the uppermost shear layer, the eruption of boundary layer fluid is attributed principally to an interaction between the secondary and primary recirculating regions as suggested by Peridier, et al. (1991a,[93] 1991b[94]).

Like Van Dyken, et al.,[126] Ghia, et al. (1991)[39] also chose to use a third-order upwind-biased implicit integration scheme, but unlike the former study, they used it to integrate the convective vorticity terms in a two-dimensional vorticity/streamfunction formulation of the Navier-Stokes equations. They simulated the flow field about an NACA 0015 airfoil pitching at $\Omega^* = 0.1$ with Reynolds numbers of 10,000 and 45,000. The third-order accurate solver with finer grid resolution was implemented in an effort to reduce oscillations and improve the quality of the results, yet their integrated loads, which comprise the bulk of the results from this study, still display considerably higher levels of oscillation than comparable experiments or computations.

Accurate simulation of high Reynolds number flows requires the use of either extraordinarily high-resolution grids (i.e., a DNS approach) or a turbulence model. Many such models have been developed over the years, and the three most frequently used are the Baldwin-Lomax zero-equation model after Baldwin and Lomax (1978),[6] the Spalart-Allmaras one-equation model after Spalart and Allmaras (1992),[115] and the k-ε two-equa-

tion model after Jones and Launder (1972).[58] Visbal (1990a)[129] used the Baldwin-Lomax model to simulate transonic dynamic stall processes. His results for fixed angles of attack compared very favorably with experimental integrated load measurements, and the dynamic stall results compared favorably with all available experimental data, at least up to the point of leading-edge separation. Discrepancies noted for $\alpha > \alpha_{sep}$ were attributed to "deficiencies in the turbulence model and/or three-dimensional effects present in the experiments." Rizzetta and Visbal (1992)[104] considered the performance of the Baldwin-Lomax and k-ε models when simulating the constant pitch-rate dynamic stall flow field, concluding that neither method worked consistently well, especially after separation. Ko and McCroskey (1997),[65] in a computational study of the oscillating airfoil problem at $Re_c = 1.95 \times 10^6$ and $M_\infty = 0.3$, attempted to identify a turbulence model which would produce data that agrees well with experimental gross features like the lift-, drag-, and moment-coefficient time histories. They investigated all three of the models listed above and found that none of them produced consistently good results even for attached flow, let alone for light or deep dynamic stall conditions.

Ekaterinaris and Menter (1994)[27] noted that, "For an untripped high-Reynolds-number flow, it was found necessary to take into account the leading-edge transitional flow region to capture the correct physical mechanisms that lead to dynamic stall." While their best results are indeed based on computations that take these factors into consideration, in general the agreement is only fair between their computations and the oscillating airfoil experiments of Piziali (1994).[96] Regarding their simulations, Ekaterinaris (1995)[26] wrote:

> It was found that turbulence models which involve boundary-layer length scales in their formulation are not suitable for the prediction of unsteady flows with large sepa-

> ration. (...) It was generally observed that none of the turbulence models could predict accurately the hysteresis effect during the downstroke. In addition, turbulence models which suppress separation, such as the k-ε model, do not predict increase of drag and pitching down moment during the downstroke and lead to premature flow reattachment. Among the (8) models tested, (...) the predictions obtained with the Baldwin-Barth[5] one-equation turbulence model, even though far from being perfect, were in reasonably good agreement with the experiment.

The best results obtained by Ekaterinaris were for the two-dimensional oscillating airfoil problem using the Baldwin-Barth model, a time step that scaled inversely with the pitch rate, and subiterations between each time step.

Like several of the authors noted above, Yu, et al. (1995)[141] also used a Navier-Stokes solver which was developed with the vorticity vector as the primary variable to study the dynamic stall process. Their focus was a challenging simulation of the $Re_c = 200{,}000$ flow over oscillating NACA 0012, VR-7, and VR-12 airfoils with fixed slats, drooped leading edges, and blowing, for which hydrogen bubble flow visualizations and integrated load data were available. Their ZETA code used the Baldwin-Lomax turbulence model, and they achieved limited success in matching the results of their computations to the available experimental data.

One important requirement for any computational model is the validation of that model against experimental results. Regarding CFD code validation, Marvin (1995)[77] writes that one requires:

> ... detailed surface- and flowfield comparisons with experimental data to verify the code's ability to accurately model the critical physics of the flow. Validation can occur only when the accuracy and limitations of the experimental data are known and thoroughly understood and only when the accuracy and limitations of the code's numerical algorithms, grid density effects, and physical basis are equally known and understood over a range of specified parameters.

Furthermore, although many have argued that this definition of validation is "too restrictive, especially for the complex applications associated with realistic geometries, never-

theless NASA has maintained the definition as a goal of its validation process." One of the greatest difficulties associated with code validation is acquiring accurate, quantitative, experimental flow field data.

Quite a few computationalists have attempted to match their computational conditions to those of an experiment. Oscillating airfoil studies in this category include the works of Ekaterinaris and his co-workers (refs. 27, 26, and 126), Yu, et al. (1995),[141] and Ko and McCroskey (1997).[65] In general, surface pressure and/or load cell measurements of global quantities such as lift, drag, and moment comprise the experimental data used, except for reference 126, which compared against whole-field interferometric data. In the realm of constant pitch-rate studies, Visbal (1986b,[128] 1990a,[129] and 1991[131]) and Visbal and Shang (1989)[133] made particularly noteworthy efforts before the availability of whole-field measurements to match their computations to existing experiments and compare the resulting data sets. Shih, et al. (1992)[113] computed and compared against their own whole-field PIV measurements. Lin, et al. (1997)[72] used the same Reynolds number and pitch rate in their experiments and simulations, and they compared the resulting normal force time series. The results and deficiencies of those studies and comparisons have already been discussed above.

Consequently we can conclude that although computational methods have been used for many years, an adequate set of experimental flowfield data has been unavailable to use for the validation of those codes. None of the experiments published to date have provided boundary-layer resolved measurements of the unsteady separation process, especially near the leading edge. Hence the critical underlying physical phenomena deduced from computations remain without experimental validation. The present computations are

performed using essentially the same conditions as the corresponding experiments, and the validation of those computations follows from a comparison of the detailed whole-field measurements with the computed flow fields.

1.3. Unsteady Separation

Prandtl (1904)[99] described separation as the phenomenon wherein "a fluid-sheet projects itself into the free flow and effects a complete alteration of the motion." Consensus was reached long ago on a definition of the separation point in steady flow over a motionless wall: separation (or reattachment) occurs where the wall shear stress is zero. On the other hand, a suitable definition for unsteady separation has been under debate for decades. Since the dynamic stall process is intimately connected with the unsteady separation of the flow near the leading edge, it is logical to consider how the various definitions of unsteady separation relate to our computational and experimental flow fields. In addition, knowledge of where separation occurs would permit simpler, circulation-based estimates to be made of the integrated loads during a dynamic stall event (e.g., see Sears, 1956[109]).

In his seminal paper on the unsteady separation of laminar boundary layers, Moore (1958)[87] argues that dynamic stall is a quasi-steady event, and that therefore using the steady separation criterion, $\tau_{wall} = 0$, is a valid way to locate the unsteady separation point. Moore's analyses are based on either a steady boundary layer in a moving frame of reference, in which case the frame is transformed, or a quasi-steady boundary layer and stationary frame of reference, in which case a perturbation analysis is used. In both cases

"Goldstein-type" singularities in the boundary layer equations are used to locate the separation point. With respect to the moving-wall problem, applicable to the dynamic stall phenomenon, Moore hypothesizes the existence of a "bubble separated from the rest of the boundary layer," and the farthest-upstream extent of the bubble is defined to be the separation point, a point which in general is not located at the wall. Furthermore, he suggests that if the boundary layer is steady in a slowly-moving frame of reference, then the separation point can be defined as that location where $\underline{U} = \tau = 0$. The discussion which followed the presentation of Moore's paper highlights the lack of consensus on what constitutes unsteady separation:

> A very expansive discussion on the concept of 'separation' in unsteady flows followed the presentation. In particular, M. B. Glauert, C. C. Lin, G. I. Taylor, and H. Görtler represented their points of view using instructive examples and pointed out the many difficulties associated with defining 'separation.' On one hand the more formal point of view was expressed that 'separation' should be defined as a concept that depends on the frame of reference. Arguments on the other hand were based on a physical perspective in which 'separation' was said to be the result of upstream motions that originate far downstream. It is quite understandable that a consensus was not reached on a usable definition of 'separation.' The session chairman, J. Ackeret, observed, "It seems to me that a new symposium could be held just to dispute the concept of 'separation.' "

In 1956 Rott[107] presented a theoretical solution of Hiemenz flow in the vicinity of a laterally oscillating plate. He observed no indications of separation in the vicinity of the point where $\tau_{wall} = 0$, and therefore concluded that this criterion is unsuitable when one is dealing with unsteady separation. Sears (1956)[109] suggested that "...the appearance of a stagnation point and a dividing flow trajectory between boundary-layer and wake fluids in the flow seen by an observer moving with the separation point" is the correct definition of unsteady separation. He continued:

> The reasoning behind this suggestion is simply that 'separation' is presumed to mean the breaking away of the boundary layer from the surface, invalidating the boundary-

> layer approximations, and that (by analogy with the steady case) this will be caused by wake fluid thrusting itself under the boundary layer and deflecting it away. Thus the appearance of a dividing streamline (trajectory) between wake fluid and boundary-layer fluid should be a necessary feature of separation, and this can surely have meaning only when viewed from the moving frame of reference.

The combination of these three papers led to the development of the Moore-Rott-Sears (MRS) unsteady separation criteria, which Williams (1977)[139] states as follows: "The unsteady separation point is characterized by the simultaneous vanishing of the shear and velocity, in a singular fashion, at some point in the boundary layer, as seen by an observer moving with the separation point." The primary difficulty associated with applying this criterion to experimental data is obvious: one must know the motion of the separation point before the separation point can be located.

Although Moore (1956)[87] and Sears and Telionis (1975)[110] very carefully specified that zero shear is one condition of the generic MRS criterion, they sometimes wrote $\partial u/\partial y = 0$, when it was clear that they were referring to a value of the shear stress at a solid wall, where $\tau = \partial u/\partial y|_{y=0}$. This fact has been overlooked by some researchers, along with the requirement that the stagnation point must be found in a frame of reference moving with the separation point, leading to highly unsatisfactory results (e.g., see Inoue, 1981[56] and Cassel, et al., 1996[13]). Noting that the shear stress is invariant under a uniform shift in the velocity field or the addition of an arbitrary solid body rotation, an algorithm could be developed to locate MRS points on the basis of experimental data or full Navier-Stokes computations, but it would be a highly complex and iterative procedure.

Sears and Telionis (1975)[110] clarify that the purpose of the MRS criterion is to use the boundary layer equations themselves to locate where the boundary layer assumptions no longer hold. At MRS points some aspect of a numerical solution of the boundary layer

equations becomes unbounded, but the physical significance of those points remains dubious. Sears and Telionis themselves write, "To be sure, the singularities are features of the boundary-layer equations and not of the full Navier-Stokes equations: infinities do not occur either in the solutions of the full equations or in experiments." Furthermore, it is not expected that an MRS point in a simulation will be located exactly at a separation point, since the motion of the MRS point is based upon boundary layer assumptions which are in the process of becoming invalid. We therefore conclude that although the MRS criteria may be satisfied in the neighborhood of an unsteady separation point, direct application of the MRS criteria to experimental or computational data is not a suitable way to locate such a point.

We turn then to Moore's (1958)[87] contention that dynamic stall is a quasi-steady event, and therefore that the locations of zero wall shear define the unsteady separation (or reattachment) points. This contrasts with Rott's (1956)[107] observations and with those of Sears and Telionis,[110] who note that

> ... reversal of flow direction at the wall therefore has no special significance in boundary-layer flows other than steady flow past a fixed wall. It does not signal the end of the boundary layer and the beginning of a wake or separated 'bubble.' Clearly, unsteady effects make it possible for flow direction to reverse without destroying the boundary-layer character of the flow.

Is the dynamic stall flow field unsteady enough so that zero wall shear does not indicate the point at which "a complete alteration of the motion" is effected? McCroskey (1982, Figure 2, p. 290)[79] shows that quasi-steady assumptions cannot be used for even the simplest models of the dynamic stall load coefficients. Visbal (1990b)[130] points out that the ratio between the viscous time scale and motion time scales is typically greater than unity even for very low pitch rates, so the flow must be considered unsteady from the viscous

perspective. Conger and Ramaprian (1994)[19] note that the shift in their lift coefficient data is one indication of "the departure of the flow from quasi-steady behavior, which should be expected to become significant as the Strouhal number, α^+, becomes larger." It has also been shown that the presence of a thin region of reversed flow does not automatically alter the "boundary-layer character of the flow." We therefore conclude that our flow cannot be modeled using quasi-steady assumptions and that $\tau_{wall} = 0$ is not a suitable indicator of the unsteady separation point in our flow field.

Shen's (1978)[111] Lagrangian model of unsteady separation led to the conclusion that the Goldstein-type singularity was caused by a "piling up" of the boundary layer fluid, which made the vertical extent of the boundary layer "unbounded." He wrote, "We concur with Sears and Telionis that the boundary layer equation could serve to predict separation approximately, provided of course the imposed pressure gradient is essentially correct up to the vicinity of the separation location." Van Dommelen and Shen (1983)[125] also suggested that,

> ... when for sufficiently high Reynolds number the concept of a thin boundary layer can meaningfully be introduced, it becomes possible to define separation in the sense that this boundary layer is no longer in the immediate vicinity of the wall as compared to its thickness. And it is this distinction in the location of the boundary layer that will make the physically crucial difference in other flow characteristics as well: wall pressure gradient, wall shear, Kelvin-Helmholtz instability, roll-up, etc.

The works cited above in conjunction with those of Van Dommelen and Cowley (1990)[124] suggest that an unsteady separation point might be defined on the basis of the boundary layer thickness, δ, the displacement thickness, δ^*, or the momentum thickness, θ, relative to their initial values at $\alpha = 0$.

Walker, Smith, and their co-workers (Walker, 1978[134]; Elliott, et al., 1983[28]; Elliott and Smith, 1987[29]; Peridier, et al. 1991a,[93] b[94]; Cassel, et al., 1996[13]; and others)

have also investigated the near-wall behavior of unsteady separation, both analytically and numerically, first using an interactive boundary layer method, then formulating the problem in Lagrangian coordinates, which allows the solution to be advanced beyond the time of singularity formation in the continuity equation. They conclude, like Shen and his colleagues, that a terminal boundary-layer structure forms (see Figure 1.4), which is "independent of the specific form of the external adverse pressure gradient that initiated the eruptive process at some earlier time. Therefore this terminal structure is believed to be generic and to apply to most cases of unsteady boundary-layer eruptions in two-dimensional incompressible flow." They propose displacement thickness, in particular, as a suitable metric for detecting this eruption of boundary-layer fluid.

One problematic aspect of this model when applying it to the dynamic stall flow field is that it doesn't allow for the formation of opposite-sign vorticity prior to the eruption of boundary layer fluid. In the experiments of Gendrich, et al. (1997),[33] the development of opposite-signed vortical regions was intimately connected with the unsteady

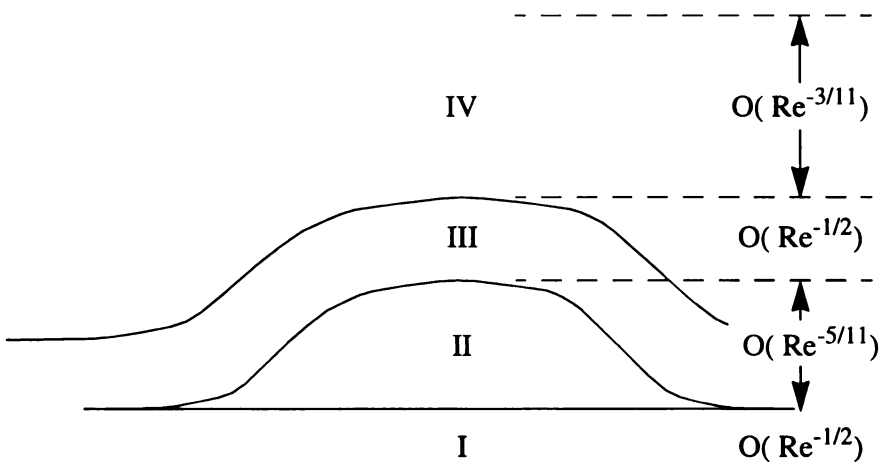

Fig. 1.4: Terminal boundary-layer structure schematic (not to scale), after Cassel, et al. (1996)[13].

separation associated with a vortex ring impinging upon a solid wall, although similar developments were not observed in the simulations of Walker, et al. (1987).[135] Similarly, many past experiments, computations, and the results of the present work all document the formation of a thin region of opposite-signed vorticity underneath that being shed from the leading edge well in advance of any boundary layer breakdown, suggesting that this terminal boundary layer structure is in fact not generic. This will be discussed further in Chapter 4.

A different approach is taken by Ghosh Choudhuri, et al. (1994),[40] who hold that topological developments in the streamline pattern yield information not only on the location of separation streamlines but also on the formation of foci, which indicate the birth of new recirculating regions. This is certainly correct, but the principal difficulty with this approach lies in the selection of an appropriate frame of reference in which to compute the streamlines. Even a constant shift applied to the velocity field produces significant changes in the streamline pattern; adding constant-body rotation can also cause large changes in the existence and location of critical points and the surrounding streamlines. (This is, of course, one of the difficulties associated with finding MRS points, as discussed above.) Ghosh Choudhuri, et al.[40] decided to use the rotating frame of the airfoil for their analysis, because of "the seemingly intuitive advantage for physical interpretation of 'forward' and 'reverse' flow relative to the airfoil."

A direct consideration of the vorticity field is not subject to problems associated with the frame of reference: constant velocity shifts have no effect at all on the vorticity field, and adding solid-body rotation equivalent to the pitch rate of the airfoil shifts the vorticity values by much less than the accuracy of our measurements. The development of

an opposite-signed vortical region under the original shear layer is an unambiguous indication of the change from a wall-bounded shear flow to a free shear layer and the concomitant reduction in the stability of the system. Furthermore, Reynolds and Carr (1985)[103] and Visbal (1990b)[130] suggest that a local accumulation of vorticity is responsible for the boundary layer growth and subsequent unsteady separation in the dynamic stall process. Analyses of the vorticity field will be presented in Chapter 4 as another indicator of the developing dynamic stall flow field.

1.4. Contents of the Present Work

In this work we present a joint computational and experimental study of the constant pitch-rate dynamic stall process. Rather than attempting measurements at flight Reynolds and Mach numbers, we are interested in the behavior of a low Reynolds number flow field. Previous studies have indicated that the effects of pitch rate are much greater than the Reynolds number effects, and as Visbal (1991)[131] writes,

> From the experimental standpoint, low speed flows are more amenable to flow visualization and permit the study of higher non-dimensional pitch rates. From a computational perspective, the consideration of laminar flow reduces numerical resolution requirements, and, most importantly, eliminates the uncertainties associated with the modeling of turbulence effects.

Specifically, we present boundary-layer resolved experiments and computations of an NACA 0012 airfoil in a $Re_c = 12{,}000$ flow pitching about the quarter chord at rates in the range $0.1 \leq \Omega^* \leq 0.4$. Since the behavior of the flow near the leading edge appears to have the strongest impact on flow field development and controllability, our experiments and analyses focus on this region.

The results of this study can also be used to evaluate our current understanding of the boundary layer developments which are associated with unsteady separation in the presence of a moving wall and a strong adverse pressure gradient. As a consequence of the difficulties associated with finding the frame(s) of reference in which to locate MRS points, we will not attempt to find points that satisfy the Moore-Rott-Sears unsteady separation criteria. We will, however, evaluate whether the rotating frame of reference attached to the airfoil is the appropriate frame to use for finding MRS points. The flux of vorticity will be analyzed to locate regions of local vorticity accumulation, and the development of different regions containing opposite signed vorticity will be carefully analyzed with respect to the development of the dynamic stall vortex and breakdown of the boundary layer. Streamlines will also be computed in both the absolute frame and the frame of the airfoil for comparison with the results of Ghosh Choudhuri, et al. (1994)[40] and Oshima and Ramaprian (1997).[92]

Following Prandtl's lead,[99] we will use the term "separated" to mean that a radical alteration of the flow field has been caused by developments in the boundary layer. When a thin region of opposite-sign vorticity is present under the primary shear layer, the flow is certainly detached, but we will call it separated only when the streamlines no longer follow the general contours of the surface. These definitions of separated and detached also correspond to those presented by Sears and Telionis (1975)[110] and Doligalski, et al. (1994),[24] among others.

Chapter 2

THE EXPERIMENTAL METHOD: MOLECULAR TAGGING VELOCIMETRY (MTV)

As discussed in Chapter 1, a non-intrusive whole-field measurement technique is required to investigate the low Reynolds number flow dynamic stall flow field. In this chapter we describe an implementation of Molecular Tagging Velocimetry (MTV) which satisfies these requirements.

Molecular Tagging Velocimetry (MTV) is a simultaneous multi-point non-intrusive measurement technique which takes advantage of molecules premixed in the flowing medium that can be turned into long lifetime tracers upon excitation by photons. A pulsed laser is typically used to tag the regions of interest, then the luminescence from the tagged regions is imaged at two successive instances within the tracer's lifetime. The measured Lagrangian displacement vector provides the estimate of the velocity vector. To measure two components of the velocity in a plane, the luminescence intensity field must have spatial gradients along two, preferably orthogonal, directions. For single-point velocimetry, this is easily achieved using a pair of crossing laser beams; a grid of intersecting laser lines allows multipoint velocity measurement. An example is illustrated in Figure 2.1.

MTV implementations require chemical compounds with long luminescence lifetimes. Current laser-induced fluorescence (LIF) techniques are generally not suitable for this purpose because of the short lifetime of the fluorescence process (τ = several

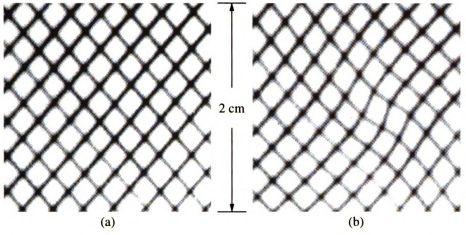

Fig. 2.1: Sample experimental MTV grid. (a) just after laser tagging. (b) displaced grid 6 ms later.

nanoseconds). McKenzie (1993)[82] provides a review of several possible chemical systems which could be used to investigate the dynamic stall flow field in high-speed flows. One category of such techniques involves flow tagging by one laser to produce an electronically excited state, followed by laser-induced fluorescence of that excited state with another laser. RELIEF is one implementation of this sort of technique, see Miles, et al. (1987,[83] 1989,[84] and 1993[85]). The techniques reviewed by McKenzie are typically applied when $U_{\min}$ is large; Stimulated Raman Spectroscopy, for example, has only been applied with $2.6 \leq M_{\infty} \leq 4.3$.

As mentioned earlier, the pulse-diffraction interferometric technique of Chandrasekhara and his co-workers (refs. 15, 126, and 138) is also a potentially suitable diagnostic with which to study the dynamic stall process. It is important to note, however, that the actual quantity measured by this method is the density of the flow field, from which the velocity field is inferred. Appreciable density variations must be present for this technique to work, which makes it unsuitable for use in a low Reynolds number flow field. In low-speed gas-phase flows, the phosphorescence of biacetyl has been utilized in

environments without oxygen (Hilbert and Falco, 1991[48]; Stier, et al., 1995[118]; and others). At present, no phosphorescent chemical systems are available to study low-speed gas-phase flows in the presence of oxygen.

In liquid-phase studies three types of chemical systems have received the most attention. The first relies on photochromic molecules which have required experimentalists to use organic solvents such as kerosene as the flowing medium, see for example Popovich and Hummel (1967),[98] Falco and Chu (1987),[30] Ojha, et al. (1989),[90] Chu and Liao (1992),[16] and Chu, et al. (1993).[17] In a photochromic process excitation by photons causes a change in the absorption spectrum and therefore a change in the color of the solution (e.g. from clear to dark blue). The color change can persist for several seconds to minutes, although the tagging process occurs within nanoseconds. The photochromic process is reversible, therefore the chemical is reusable. It should also be noted that the use of photochromic chemicals requires two photon sources: typically a pulsed UV source (e.g. $\lambda = 351$ nm from an excimer laser) to induce the color change and a white light source to interrogate the tagged regions. With the development of water-soluble photochromics, the potential applications of this molecular design are expanding. Applications of chemically modified water-soluble photochromic dyes have been reported by Douglas, et al. (1991)[25] and Yurechko and Ryazantsev (1991).[142]

The most significant drawback associated with using photochromic chemicals is that each image is produced by a change in the absorption spectrum of the mixture, thereby requiring a measurement of the difference between incident and transmitted light. Emitted light when viewed against a black background is more easily and more accurately detected than transmitted light; consequently, images based on luminescence are better

suited to MTV applications. The long relaxation period of the photochromic chemicals poses a second difficulty for the dynamic stall experiments performed in the current work. For the highest pitch rates studied, the duration of the entire process is less than the relaxation period of all currently available photochromic chemicals. If photochromics were used, each tagged region would be imaged many times as it distorted and convected with the flow. This would complicate analysis of the data considerably, although it is possible that the two-camera data acquisition technique and spatial correlation analysis methods described below could be used successfully to make the use of photochromics feasible in our experiments.

Caged fluorescein and similar compounds have recently become available, and their use was first introduced by Lempert, et al. (1995)[71] and Harris, et al. (1996a,[44] 1996b[45]). In this compound a chemical group is attached to fluorescein in order to render it non-fluorescent. The caging group is removed upon absorption of UV photons ($\lambda = 350$ nm), thereby creating regular fluorescein which fluoresces with a very high quantum efficiency. Here the long-lifetime tracer is the uncaged fluorescein, which persists for a very long time and can be interrogated at the time of interest through its luminescence upon re-irradiation. Two sources of photons are therefore needed, one to break the cage and the other to excite fluorescence.

Three aspects of the current makeup of caged fluorescein require special attention when designing an experiment: the cage-breaking process is not rapid, occurring with a time constant on the order of a few milliseconds; the chemical bond between the cage and the fluorescein is fragile, decaying both spontaneously and with exposure to room light; and the cage-breaking process is irreversible, so each caged molecule can be tagged only

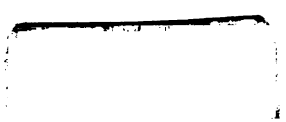

once. In order to tag high-speed fluid flows, a new pattern would have to be generated frequently after each old pattern was swept away downstream. On the other hand, such frequent tagging of low-speed fluid near a solid wall would generate a pattern that was practically impossible to analyze, even given the image analysis techniques described below. The difficulties associated with using caged fluorescein, in conjunction with its very high cost, preclude its use in our experiments.

The third type of chemical system under consideration comprises a new class of recently engineered water-soluble phosphorescent supramolecules. In this case excitation by photons is used to produce a long-lived excited state which is interrogated through its phosphorescence emission as it radiatively returns to its ground state. The long-lifetime tracer is the excited state molecule itself. Only one source of photons is needed, and the excitation/emission process is reversible. The difficulty is that the long-lived excited state (i.e. phosphorescence) suffers from quenching by O_2 and H_2O, and as a result, suitable molecular complexes have not been available until recently. One disadvantage of the phosphorescent supramolecules described here is their lower quantum efficiency ($\phi_e = 0.035$) compared to that of uncaged fluorescein ($\phi_e = 0.90$). This is offset, however, by the advantages of reusability, the need for only one photon source, and a lower cost (estimated to be between 5 to 100 times less, depending on whether a CW or pulsed laser source is used to interrogate the uncaged fluorescein).

Early utilization of these compounds has been reported by Koochesfahani, et al. (1993),[67] Hill and Klewicki (1994),[49] Stier (1994),[117] Gendrich, et al. (1994),[35] Cohn, et al. (1995),[18] and others. Information regarding these phosphorescent complexes, including properties relevant to the optimal design of an MTV experiment, was published by

Gendrich, et al. (1997).[36] A statistical study on the accuracy of a spatial correlation technique used to process image pairs can be found in Gendrich and Koochesfahani (1996).[34] In the coming sections, details of the specific MTV implementation used to study the dynamic stall process are presented. If more complete information is required regarding the chemistry or analysis of this type of MTV, the reader should consult reference 36 or 34, respectively. Furthermore, the review by Koochesfahani, et al. (1996)[66] also provides a summary of recent developments in Molecular Tagging Velocimetry.

2.1. The Chemistry of MTV

Findings by Nocera and his group (Ponce, et al., 1993[97]; Mortellaro and Nocera, 1996[88]; and Hartmann, et al., 1996[46]) show that supramolecules may be designed to exhibit long-lived phosphorescence which is not quenched by the presence of oxygen or water. A successful design by Ponce, et al.[97] indicates that the quenching of a lumophore can be stopped, and the phosphorescence emission recovered, by mixing certain alcohols with an aqueous solution of a cyclodextrin (CD) cup that contains the lumophore. Cyclodextrins are molecules constructed from sugars connected in a head-to-tail arrangement. The molecule is cup-shaped with its size determined by the number of sugars in the structure. Figure 2.2 depicts glucosyl-ß-CD, the CD used in our application, which is constructed of 7 glucose subunits, resulting in an outer cup dimension of 15.3 Å and an inner cup cavity dimension of 7.8 Å. The size of the cavity is important for effective binding to the guest molecule, in our case 1-bromonaphthalene (1-BrNp), which is the lumophore.

The long-lived, green phosphorescence (lifetime $\tau \approx 5$ ms) of 1-BrNp is efficiently

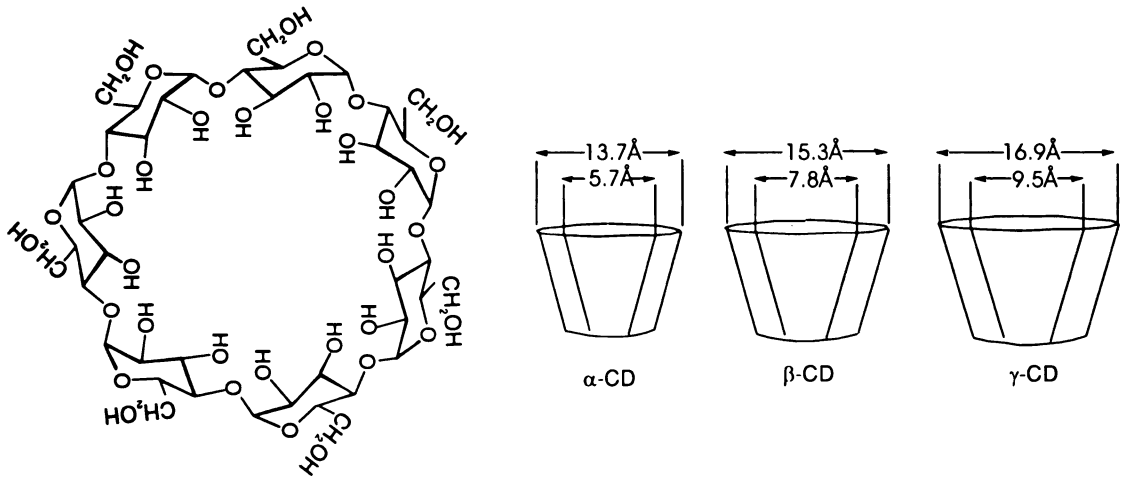

Fig. 2.2: The chemical structure of cyclodextrins. Glucosyl-β-cyclodextrin (gβ-CD), the molecule used in the present study, is a β-CD with an additional glucose added to increase solubility in water.

quenched by oxygen, even when the lumophore is held inside a CD cup. The phosphorescence can be recovered upon adding an alcohol (ROH) to the solution as shown in Figure 2.3. Detailed studies of Ponce, et al.[97] and Hartmann, et al.[46] show that a ternary complex (1-BrNp · Gß-CD · ROH) is formed, where the alcohol hydrogen bonds to the rim of the CD cup and acts as its lid, thereby shielding 1-BrNp from oxygen. The phosphorescence enhancement can be very large, approaching 10^4-10^5, depending on the fit of the alcohol lid to the CD cup. A wide variety of alcohols may be used as the cap, see Ponce, et al.[97] and Hartmann, et al[46] The choices of the alcohol and its concentration strongly influence the phosphorescence lifetime and intensity. Figure 2.4 shows the dependence of total phosphorescence emission on concentration for three different types of alcohol, *tert*-butanol (*t*-buOH), cyclohexanol (cycOH), and neopentanol (neopOH). The lifetimes for *t*-buOH and cycOH have been measured to be about 5 ms and 4 ms, respectively, for the alcohol- and CD-concentration independent ranges.

When using phosphorescent supramolecules for molecular tagging purposes, the

images acquired at a prescribed time delay Δt after tagging are always less intense than those acquired right after tagging as a result of the exponential decay of the luminescence. To obtain the highest possible image signal-to-noise, the chemical composition must be selected to yield the highest intensity for the selected Δt. For this reason an excess of immiscible 1-BrNp is always present in our experiments to maintain a saturated solution of the lumophore (typically a molar concentration of order 10^{-5} M). The choice of an alcohol and its concentration is based on data such as that in Figure 2.4. It can be seen that neopOH at 0.15 M is expected to produce the highest intensity, but unfortunately the use

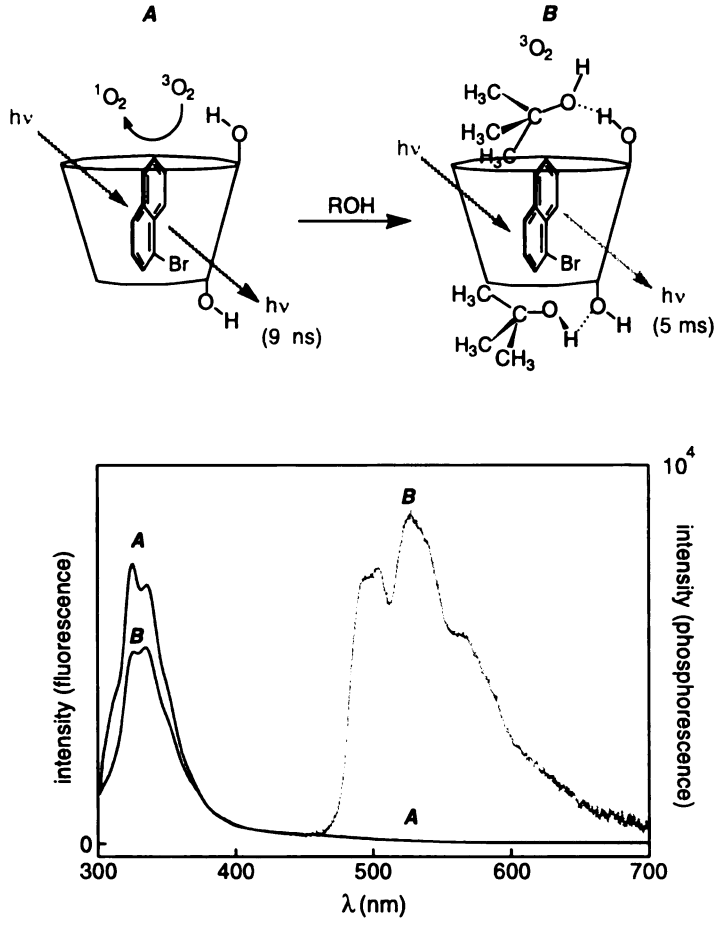

Fig. 2.3: Emission from 1-BrNp in gβ-CD (A) Only blue fluorescence is exhibited in the absence of an appropriate alcohol (ROH); (B) A bright green phosphorescence plus a reduced initial fluorescence is seen upon the addition of ROH, which prevents the quenching of 1-BrNp phosphorescence by O_2.

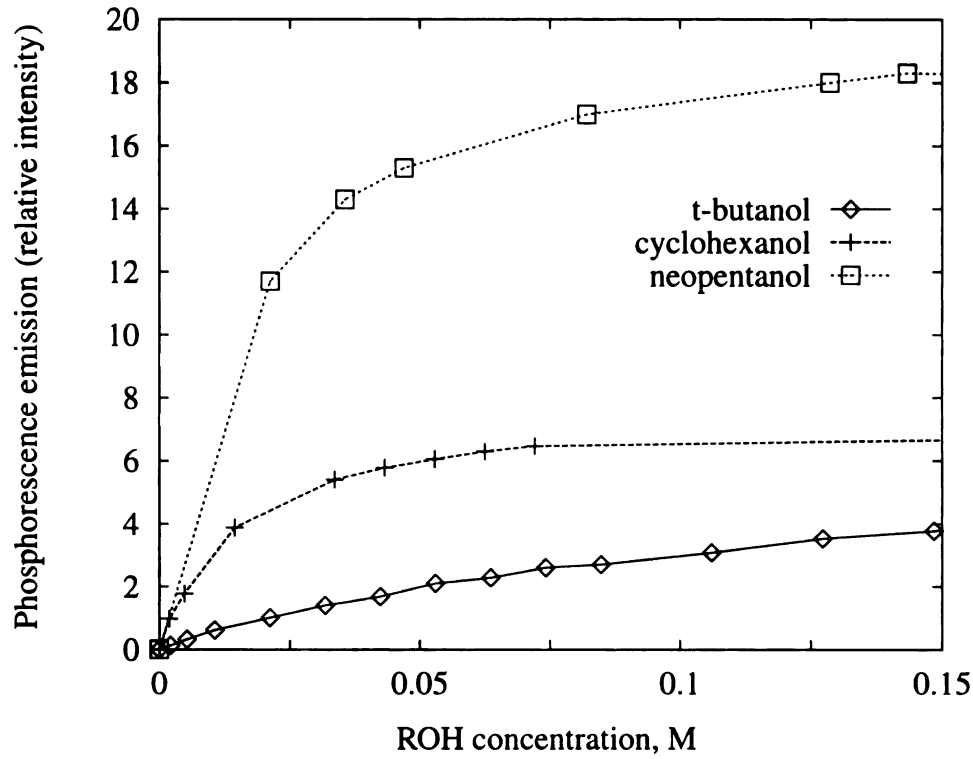

Fig. 2.4: Total phosphorescence emission from 1-BrNp · gß-CD · ROH for three different types of alcohol at fixed concentrations of 1-BrNp and gß-CD.

of neopOH in large-scale experiments is cost-prohibitive. The complex made using cyclohexanol, the next best choice, yields 90% of its maximum intensity at an alcohol concentration of 0.05 M. These are the alcohol and concentration that are used throughout this work.

The selection of the CD concentration is driven by the fact that an increase in its concentration results in more phosphorescence but a reduced laser beam penetration length, because of the increased absorption of the phosphorescent complex. For a typical working distance of 30-40 cm in our water tunnel, we have found the optimal CD concentration to be approximately 1×10^{-4} M. For the mixture composition described here, the corresponding lifetime was measured to be $\tau \cong 3.7$ ms. It is useful to recall that τ refers to the time when the emission has decayed to 37% (e^{-1}) of its initial intensity. The actual

usable delay time between laser tagging and interrogation can be considerably longer and is dictated by the type of detection used. Image-intensified cameras are used in the present study to obtain images with delays of up to 8 ms; in other studies utilizing this ternary compound, delays of up to 45 ms have been used successfully.

The requirement that three components be mixed to produce the phosphorescent complex described here allows us to implement other applications beyond the traditional one of just velocimetry. These other applications include molecularly tagging a passive scalar mixing region and monitoring its Lagrangian evolution and molecularly tagging a chemical reaction interface between two streams and observing its Lagrangian evolution. The details of these applications, which are not taken advantage of in the present work, are documented in Gendrich, et al. (1997).[36]

2.2. Tagging

Tagging the flow along single lines was originally used by Hummel and his group (e.g. Popovich and Hummel, 1967[98]; Ojha, et al.,1989[90]). In the works of Miles and his co-workers (refs. 83-85) and Lempert and his co-workers (refs. 9, 44, 45, and 71), single laser lines are still used to tag the flow (i.e., grids are not generated), and the velocity is inferred from the displacement of the line centers in much the same manner as using hydrogen bubble lines generated by a wire (see for example Lu and Smith, 1985[75]). Clearly this type of tagging can provide only one component of the velocity, that normal to the tagged line. In addition, the estimate of this velocity component has an inherent error associated with it. Following the analysis of Hill and Klewicki (1996),[50] and referring to

Figure 2.5, that error can be cast in the form:

$$\frac{\Delta u}{u} = \tan\theta \, \frac{\partial u}{\partial y} \, \Delta t \qquad (4)$$

In this expression, u is the estimated velocity component normal to the tagged line, the error in the estimated velocity is $\Delta u \equiv u_{actual} - u$, the local flow angle given by $\tan\theta = v/u$ (with v being the flow velocity parallel to the tagged line), and Δt is the time delay between tagging and interrogation. Clearly an *a priori* knowledge of the flow field is necessary in order to provide an estimate of the error. It can be observed, however, that this inherent error is identically zero only in flows where the velocity component v along the tagged line is zero (i.e. in unidirectional flows) or where the velocity gradient $\partial u/\partial y = 0$. In a general flow field where these constraints are not met, the error can be reduced by decreasing the delay time Δt, but it cannot be made arbitrarily small, since Δt has to be large enough for the resulting displacement of the tagged line to be measurable with adequate accuracy. Obviously it is not suitable to use laser line tagging when attempting to measure the complex boundary layer flow field associated with the dynamic stall process, where both velocity components and velocity gradients are non-zero.

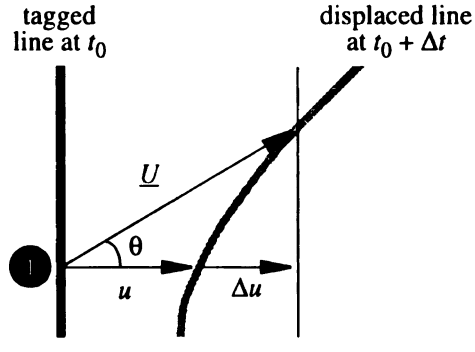

Fig. 2.5: The velocity at point 1 is $\underline{U}$. Using the line center displacement method gives a lateral velocity estimate u, with error Δu. The vertical velocity component cannot be estimated with the flow tagged in this manner.

Two velocity components can be estimated only when the luminescence intensity field from a tagged region has spatial gradients in two directions, and Gendrich and Koochesfahani (1996)[34] showed that optimal results can only be obtained when those directions are orthogonal. A pair of crossing laser beams can generate one tagged region suitable for single-point velocimetry; a grid of intersecting laser lines allows for multi-point velocity measurements. Use of this tagging scheme was first suggested by D'Arco, et al. (1982),[21] and it was later improved upon and utilized by Falco and Chu (1987).[30]

In the optical approach of Falco and Chu,[30] which is still used today, the main laser beam is split into multiple lines by an array of small mirrors, called a beam divider. We have developed a much simpler device for this purpose; a brass plate with a series of thin slots blocks a portion of the incident beam, thereby generating multiple laser lines. Figure 2.6 contrasts these two different approaches. Clearly, the beam blockers allow a smaller fraction of the total laser energy to be used for tagging purposes, however beam blockers with arbitrary slot patterns can be designed and constructed much more quickly and inexpensively than a similar mirror array. The advantages become clearer when the width and the number of laser lines have to be optimized for a particular experiment, or when beams

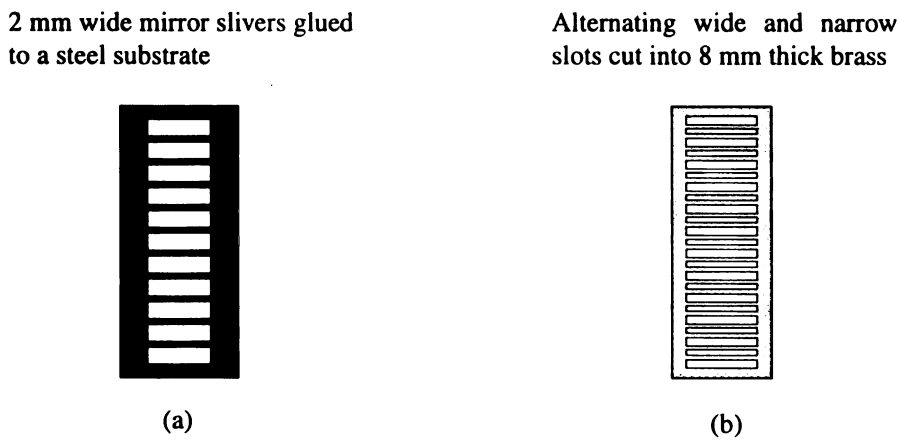

Fig. 2.6: Optical devices to create patterned illumination: (a) a beam divider as developed by Falco and Chu (1987)[30]; (b) an example of one beam blocker configuration.

of non-uniform thickness are needed to simplify the spatial correlation procedure described in Section 2.4. We note that with improved detection and processing methods, we have been able to obtain high quality data with beam blockers that transmit as little as 30% of the incident energy.

When two sets of uniform lines form an intersection pattern of the type seen in Figure 2.1, it is difficult to know which intersection from the earlier image corresponds to which intersection in the later image. In machine vision papers this is commonly known as the visual correspondence problem; see for example Haralick and Shapiro (1993).[43] Let d be the distance between two adjacent intersection points in Figure 2.1(a). In the case of uniform intersections, the time delay between images, Δt, must be made small enough so that the largest displacement of any intersection during that interval is less than $d/2$; otherwise it would be possible to mistake one intersection for another. One way to make each intersection locally unique is by using two non-uniform sets of lines to form the grid pattern. For example, if two sets of alternating wide and narrow lines intersect, the distance between identical intersections (e.g., the distance between the intersection of two narrow lines) is increased from d to $2d$, and in principle Δt can be increased so that the maximum allowable intersection displacement is approximately d. In our experiments we use beam blockers with alternating wide and narrow slots, and each field of view requires a different beam blocker configuration to achieve an optimal intersection density in the images. The specifics of these slot patterns are detailed in Table 1 on page 55.

The UV laser used in our experiments is a Lambda Physik 220 iCC excimer laser filled with XeCl. This unit provides 20 ns pulses at a wavelength of 308 nm with pulse energies between 50 and 200 mJ and repetition rates up to 100 Hz. Several mirrors,

lenses, and beam blockers are used to create an intersecting pattern of lines in the region of interest; see Figure 2.7. The main laser beam, which is initially a 3.8×1.3 cm rectangle, is first passed through a pair of cylindrical lenses in order to increase the aspect ratio of the beam in the region of interest. This pair of lenses functions as an adjustable very-long focal length cylindrical lens; the effective focal length is varied by adjusting the distance between the two lenses using a translation stage. The beam is then divided using a 50:50 beam splitter, and each of the resultant beams passes through a blocker to generate the laser grid pattern. The energy in each small beam thus generated varies between 1 mJ and 2 mJ given an incoming main laser beam of 100 mJ.

Spherical lenses are used as needed to scale the entire grid pattern for a given field

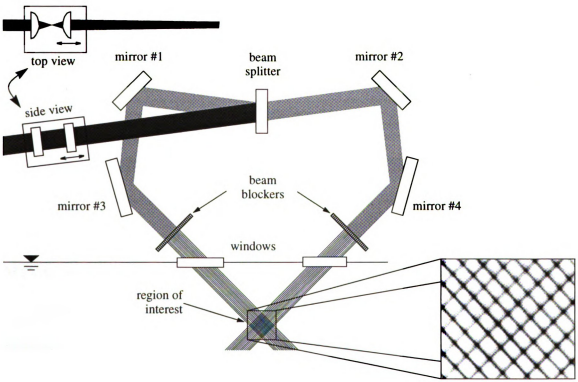

Fig. 2.7: Typical laser optics arrangement. Inset shows a region tagged using beam blockers with uniform slot width and spacing. Both top- and side-views are shown of the cylindrical lens arrangement which increases the beam aspect ratio by reducing the beam depth Δz in the region of interest.

of view (discussed in the next section). The depth Δz of the beams in the direction normal to the plane of the grid pattern is typically 250 μm ($2c$) for a 3.5 cm ($292c$) field of view. When lenses are used to reduce the pattern size for a 2 cm ($167c$), and or 1 cm ($83c$) field of view, Δz is scaled correspondingly. The inset in Figure 2.7 shows an example of a region tagged by a grid pattern generated using a beam blocker with uniform slot width and spacing.

2.3. Detection

The common element among most previous studies utilizing molecular tagging velocimetry is that a single detector is used; the initial tagging pattern is recorded once, usually at the beginning of the experiment, and then delayed images are acquired. The implicit assumption in this approach is that the initial tagging pattern remains spatially invariant throughout the experiment. Because current processing schemes measure the displacement of the tagged regions with sub-pixel accuracy (see Section 2.4), small variations in the initial pattern will be misinterpreted as flow velocity fluctuations. This is particularly problematic when a solid object like an airfoil blocks variable portions of the laser beams during the course of an experiment. We have improved the accuracy of the MTV technique by employing a two-detector imaging scheme.

This detection arrangement, shown schematically in Figure 2.8, involves a link between the laser and the two image detectors through a digital delay generator. Immediately after the laser fires, the first detector records an earlier image of the tagged flow, and after a prescribed time delay, Δt, the second detector records a later image. The selection

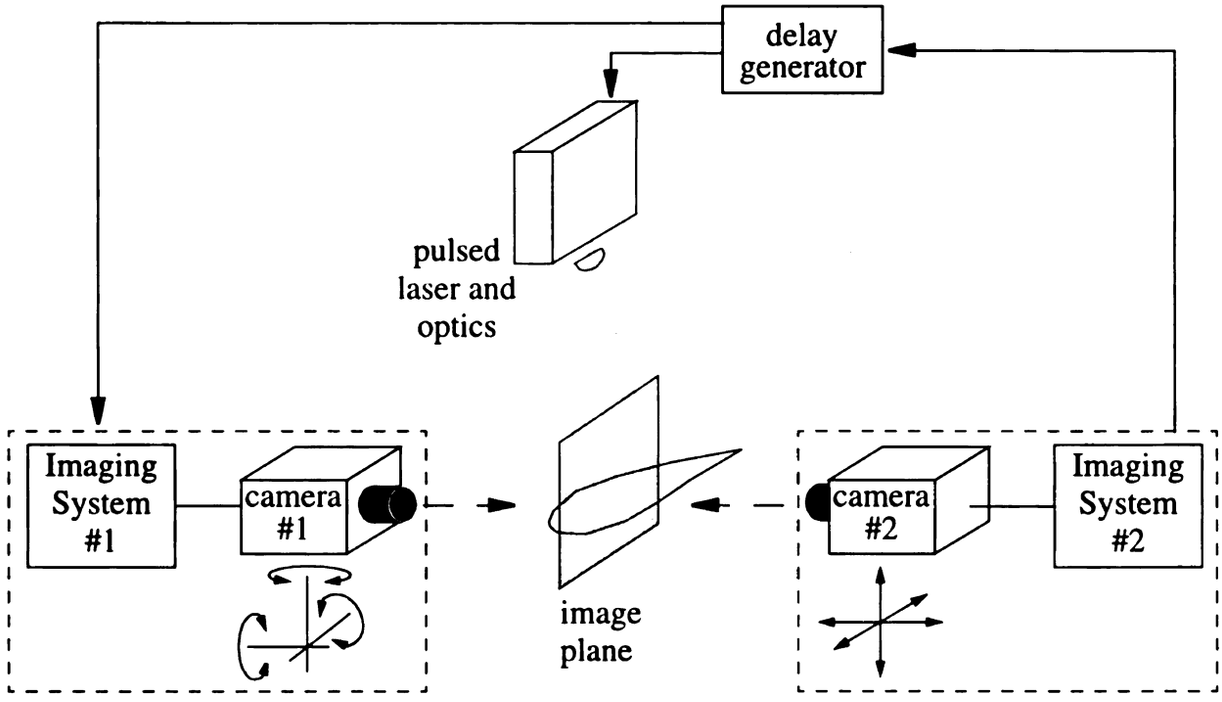

Fig. 2.8: 2-camera optical arrangement. Both cameras view the same image plane from either side of the test section. Synchronization between the two cameras and the laser is provided by a digital delay generator.

of time delay between tagging and interrogation is dictated by several factors. A larger delay will produce larger displacements and therefore a higher dynamic range in the velocity measurement. However, an increase in Δt leads to a degraded S/N in the delayed image, and it can also produce large distortions attributable to the strain rate and vorticity fields, which limits the effectiveness of our correlation procedure in estimating the displacement field (see Section 2.4).

In the arrangement shown in Figure 2.8, the two detectors view the same region of interest from opposite sides of the test section. All images are digitized to 8 bits into 512×512 pixel arrays by two Trapix-Plus image acquisition/processing systems (Recognition Concepts, Inc.) then transferred onto two 5 GB disk arrays in real time. After acquisition, the images from one camera are flipped horizontally to put them in the same

frame of reference as the images from the other camera. In previous two-detector MTV studies (Gendrich, et al. 1994[35]; Cohn, et al. 1995[18]; Gendrich and Koochesfahani, 1996[34]; and Gendrich, et al., 1997a,[33] b[36]), both cameras were located on the same side of the experiment and viewed the image plane through a cube beam splitter. In the present work the cameras are positioned on either side of the test section, which results in twice as much light being available to each camera. This produces significant signal-to-noise improvements and a corresponding increase in the accuracy of the measurements at the expense of a large but worthwhile increase in the time required to align the two cameras.

The alignment of the two cameras relative to each other is adjusted with a 3-axis translation stage on one camera and a 3-axis rotation stage on the other. The two cameras are aligned to approximately one pixel using a reference target attached to the airfoil, after which the target is removed and the laser grid itself provides alignment information. To obtain the most precise camera displacement field possible, 32 images of the same laser grid are acquired by each camera. These undelayed images have a very high signal-to-noise ratio, so the analysis of those images yields individual estimates of $D_x(x,y)$ and $D_y(x,y)$ which are accurate to at least ±0.1 pixel. Averaging these results reduces the uncertainty by a factor of $(N)^{-1/2}$, where N is 32, the number of estimates in the average. This produces a camera displacement field whose sub-pixel accuracy is better than ±0.02 pixel. This apparent displacement at zero velocity is taken into account when computing the actual displacement resulting from the flow for each image pair (see sect. 2.4, p. 60). The alignment is verified to be the same before and after each run (see sect. 2.6, p. 79).

Two Xybion ISG-350-GW3 intensified cameras with enhanced blue receptivity and reduced Automatic Brightness Control levels comprise the detectors used for all of

our experiments. The intensifier tubes and cameras are run in manual mode; Table 5 lists the settings of the switches on each camera. A Camera Control Unit (CCU) attached to each camera provides access to connectors and switches without having to disturb the cameras physically. The CCU rear panel switch settings are documented in Table 6, while Table 7 indicates how the front panel switches and knobs are adjusted. Each camera is fitted with a Nikon 105 mm f/2.8 Micro-Nikkor macro lens, a Nikon-to-C-mount adapter, and a 2× tele-extender and/or extension tubes, as needed, depending on the required field of view. Tables 5-7 are found in Appendix I.

A Stanford Research Systems (SRS) DG535 digital delay generator (DDG) is used to link the cameras and laser as indicated schematically in Figure 2.8; the DDG parameter settings are documented in Appendix I, see Table 8. Figure 2.9 diagrams all of the connections between the camera control units, the DDG, the airfoil motion controller, and the laser. Camera A supplies horizontal and vertical drive signals to camera B, and the field index from camera A triggers the DDG at the start of each odd field. The trigger synch output from the DDG causes the laser to pulse and the airfoil controller to record the airfoil's position at that instant. The delayed outputs from the DDG are fed to the external trigger inputs of each camera to control the gating of the intensifier tubes. The first delay, from the $\overline{A}\sqcup\overline{B}$ output, causes camera A to record an image 0.318 μs after the laser pulse, and the delay from the $\overline{C}\sqcup\overline{D}$ output, which is set to be an integral multiple of 63.6 μs, the horizontal drive period, causes camera B to start recording Δt seconds after camera A started to record. The exposure time for each camera can be any integral multiple of 63.6 μs; but in our experiments it is set to be the same for each camera, typically to a value of $\Delta t/10$. The recorded images are smeared to a certain extent, since the tagged molecules

continue to move during the exposure intervals. However, as long as the exposure times are the same for each camera, the effects of smearing will be identical, assuming that the acceleration field produces a negligible change in the velocity field during the time between images, Δt.

When digitizing video data from a particular sensor, the size of the smallest detectable feature is dictated by the camera's image ratio, which we define to be the size of the

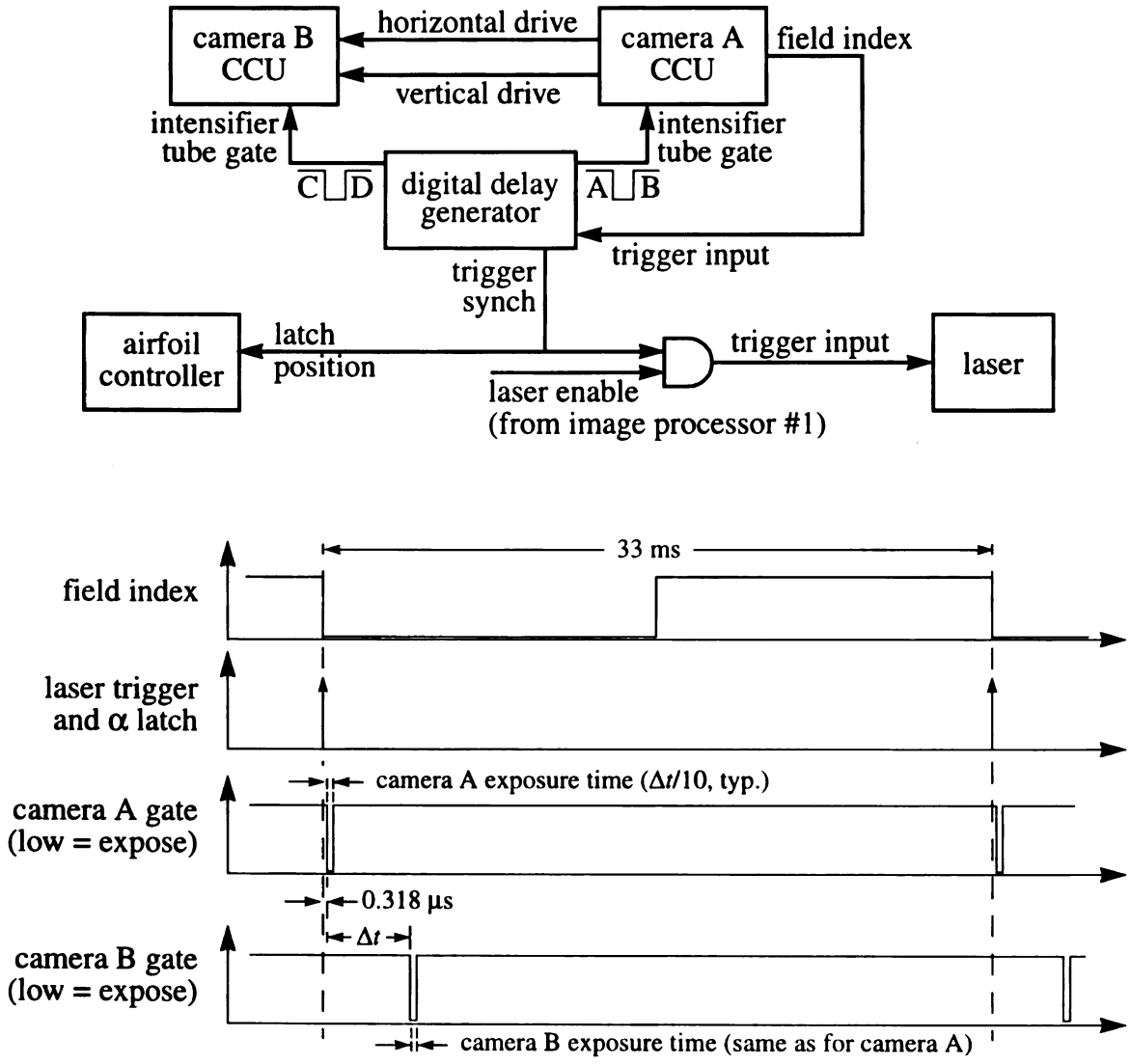

Fig. 2.9: Electronic interconnections between camera control units (CCUs), digital delay generator (DDG), laser, and airfoil motion controller, plus a diagram showing the timing of events.

field of view divided by the size of the detector. As long as an adequately repeatable flow field is under study, large fields of view can be used to image gross features, while smaller image ratios can be used to resolve the much smaller near-wall developments. An additional benefit associated with smaller fields of view is that adequate pixel displacements can still be achieved using shorter Δt values, thereby reducing the adverse effects of vorticity and strain on velocity measurements (see pp. 61-64). Three different sized square fields of view have been used in the present work; they are 3.5 cm, 2 cm, and 1 cm ($292c$, $167c$, and $83c$) on a side. For each field of view, the time delay Δt is selected to produce a 10 pixel displacement in the freestream. Multiple overlapping regions were imaged for each image ratio, as illustrated in Figure 2.10; for example, Figure 2.10(b) shows that six different regions were imaged for the 3.5 cm field of view. Different beam blocker configurations were used for each image ratio, along with the appropriate lenses needed to scale down the grid pattern. Table 1 documents these different beam blocker configurations, as well as the beam widths (FWHM) that were produced in the region being measured.

In addition to recording multiple regions for each image ratio, the pitch-up maneu-

Table 1: Beam blocker configurations.

field of view (cm)	beam blocker sizes			beam widths in the measurement region	
	wide slot width (mm)	narrow slot width (mm)	gap width (mm)	wide beam width (c)	narrow beam width (c)
3.5	6.25	2.50	5.50	5.3	2.1
2	5.00	2.50	2.50	3.7	1.8
1	4.00	2.00	2.00	1.7	0.8

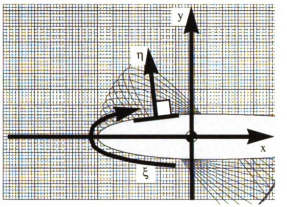

(a) Airfoil target and coordinate systems. The fine lines are spaced 1 mm ($8.3c = 8.3 \times 10^{-3}$ C) apart. $x = y = 0$ at the pitch axis. $\xi = 0$ at the leading edge, and $\eta = 0$ at the airfoil surface.

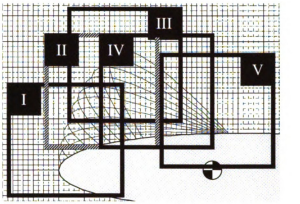

(c) Regions imaged with a 2 cm ($167c$) field of view.

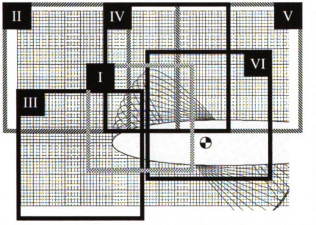

(b) Regions imaged with a 3.5 cm ($292c$) field of view.

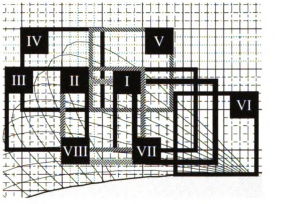

(d) Regions imaged with a 1 cm ($83c$) field of view.

Fig. 2.10: Airfoil target, coordinate directions, and the different regions imaged for each field of view (indicated by Roman numerals). The airfoil is depicted at $\alpha = 0°$; outlines of the airfoil are shown in 5° increments.

ver is also performed 140 times while the cameras view each region. In order to obtain improved spatial measurement density, the laser beam grid is repositioned five different times such that none of the intersection locations are in positions previously measured for that region. The temporal resolution of the cameras is fixed: 30 frames are recorded per second per camera. In order to improve the temporal measurement density, the time when the camera starts recording is shifted with respect to when the pitch-up maneuver begins.

Two, four, or eight runs are recorded for each grid position so that images have been recorded every 0.16°; the higher the pitch rate, the more runs have to be recorded in order to achieve this resolution. Finally, the airfoil was pitched both up and down in order to measure the velocity field on both the suction and pressure surfaces. A total of 1,820 runs were recorded, comprising approximately 117 GB of image data.

2.4. Image Pair Analysis

The traditional method for finding the displacement of tagged lines or grids has been to locate the center of each line through various techniques. Most recent techniques use a best fit of the pixel intensity values to an assumed laser line shape, for example, a Gaussian intensity distribution. We are not aware of a systematic statistical study of the performance of this approach while considering the effects of experimental parameters such as image contrast, signal to noise ratio, etc. The recent study of Hill and Klewicki (1996)[50] reports the accuracy in determining the displacement vector to be ±0.35 pixel rms. Even though efforts are under way to improve the accuracy further using better algorithms, the basic premise behind this approach is the use of a known line shape for the tagged line, which may not be known *a priori* in some situations because of a variety of reasons associated with laser beam transmission through a flowing medium, bleaching effects, objects like a moving airfoil intermittently blocking portions of the beams, etc. In the work from our laboratory (refs. 18, 33-38, 66-68, and 118), we have taken a different approach in an attempt to implement a generalized scheme that is independent of the details within a tagged region, and can accommodate arbitrary tagging patterns or patterns

which vary during an experiment. The displacement of the tagged regions is determined using a direct digital spatial correlation technique.

Consider a region in a flow tagged at time t_1 by an intersecting pair of laser beams as shown in Figure 2.11(a). The tagged region is displaced by an amount $(\Delta x, \Delta y)$ to a new location at a later time $t_2 = t_1 + \Delta t$ as a result of the local flow velocity, Figure 2.11(b). A small window, referred to as the source window, is selected about the tagged region in the earlier image, and it is spatially correlated with a larger roam window in the second image. The roam window is centered about the original location of the source window, and its extent is large enough to encompass the displacement vector. We calculate the spatial correlation coefficient $R(r,s)$ between the intensity field I_1 of the source window and I_2 of the

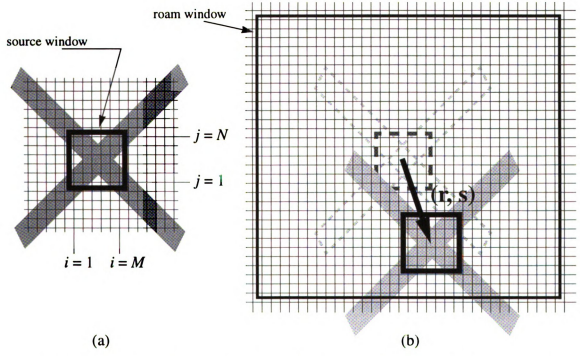

Fig. 2.11: Spatial correlation technique schematic. (a) Tagged region at time $t = t_1$. (b) Correlation of the source window with one portion of the roam window at time $t_2 = t_1 + \Delta t$; dashed lines indicate the original location of the region, while the shaded region indicates the displaced intersection. The correlation procedure works best when distortions caused by vorticity and strain are negligible during the delay interval Δt.

roam window as a function of the pixel displacement *(r, s)* between them. The correlation coefficient is computed according to the following formula (e.g., Ross, 1987[106]):

$$R(r,s) = \frac{\overline{I_1 \cdot I_2} - \overline{I_1} \cdot \overline{I_2}}{\sigma_{I_1} \cdot \sigma_{I_2}} \tag{5}$$

In this expression, an overbar refers to the expected value, and σ denotes the standard deviation of the subscripted variable. With this definition, $-1 \le R \le +1$. The representation of the various terms shown above in terms of discrete image pixel values can be computed using the following equations:

$$\overline{I_1 \cdot I_2} = \frac{1}{M \cdot N} \sum_{i,k} \sum_{j,l} I_1(i,j) \cdot I_2(k,l) \qquad \begin{cases} i = [1 \,..\, M] \\ j = [1 \,..\, N] \\ k = [1+r \,..\, M+r] \\ l = [1+s \,..\, N+s] \end{cases} \tag{6}$$

$$\overline{I_1} = \frac{1}{M \cdot N} \sum_{i} \sum_{j} I_1(i,j) \qquad \begin{cases} i = [1 \,..\, M] \\ j = [1 \,..\, N] \end{cases} \tag{7}$$

$$\overline{I_2} = \frac{1}{M \cdot N} \sum_{k} \sum_{l} I_2(k,l) \qquad \begin{cases} k = [1+r \,..\, M+r] \\ l = [\,1+s \,..\, N+s] \end{cases} \tag{8}$$

$$\sigma_{I_1} = \sqrt{\frac{1}{M \cdot N} \sum_{i} \sum_{j} \left(I_1(i,j) - \overline{I_1}\right)^2} \qquad \begin{cases} i = [1 \,..\, M] \\ j = [1 \,..\, N] \end{cases} \tag{9}$$

$$\sigma_{I_2} = \sqrt{\frac{1}{M \cdot N} \sum_{k} \sum_{l} \left(I_2(k,l) - \overline{I_2}\right)^2} \qquad \begin{cases} k = [1+r \,..\, M+r] \\ l = [\,1+s \,..\, N+s] \end{cases} \tag{10}$$

In the present work we employ square windows (i.e., $M = N$) and do not compute over the entire roam window domain when prior information is available regarding the approximate location of the displacement vector. The location of the peak in *R(r,s)* defines the displacement vector accurate to within one pixel. Sub-pixel accuracy is obtained by fitting a 9×9 pixel region about the peak in *R(r,s)* to a two-dimensional 7th-order polyno-

mial, then locating the maximum of that fit. Gendrich and Koochesfahani (1996)[34] found that the 7th-order fit of a 9×9 region produces the most accurate sub-pixel displacement estimates, so those are the parameters used throughout this work. The computed displacement vector (Δx, Δy) is corrected by subtracting the apparent displacement at the center of the source window because of camera alignment errors, $D_x(x,y)$ and $D_y(x,y)$; see Section 2.3 above. The spatial average of the velocity within the source window is then estimated according to $[u, v] = [(\Delta x - D_x)/\Delta t,\ (\Delta y - D_y)/\Delta t\,]$. After sets of image pairs have been processed into displacement fields, with displacements and vector locations both expressed in pixel values, the target images and time between exposures are used to convert pixels into normalized coordinates $((x-x_0)/C, (y-y_0)/C)$ and velocities $(u/U_\infty, v/U_\infty)$.

The example provided in Figure 2.12 illustrates a region in an actual experiment tagged by a laser grid, the tagged region at a later time, and the corresponding spatial correlation coefficient field for one of the grid crossings. A well-defined correlation peak occurs at the location corresponding to the displacement of the tagged region by the flow. This displacement peak is located to sub-pixel accuracy using the polynomial fit described above. One advantage of our processing technique over traditional line-center methods is robustness to the presence of noise, which is attributable to the averaging process inherent in the correlation procedure.

It should be noted that this procedure can also be applied to process Digital Particle Image Velocimetry (DPIV) image pairs; see for example Huang, et al. (1993),[51] Fincham and Spedding (1995),[31] Okamoto, et al. (1995),[91] and Roesgen and Totaro (1995).[105] The procedure is, however, different from the image cross correlation procedure suggested by Utami, et al. (1991)[123] and Keane and Adrian (1992),[64] where only the

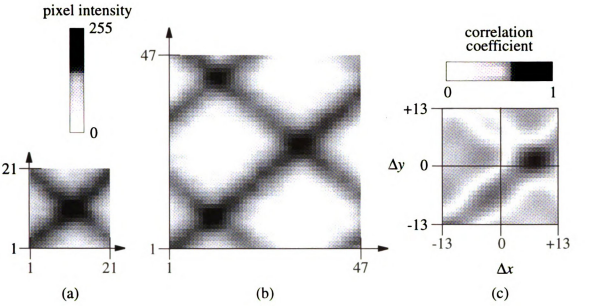

Fig. 2.12: Experimental grid intersection. (a) Source window 20 μs after laser pulse. (b) Roam window from an image of the same molecules 6 ms later. (c) Correlation coefficient field.

direct cross correlation $\overline{I_1 \cdot I_2}$ is computed instead of the complete correlation coefficient $R(r,s)$ defined earlier.

It must also be noted that our spatial correlation technique is a first-order method for estimating a linear displacement vector; it does not attempt to estimate the higher-order derivatives of the velocity field. For this reason, it is understood that Δt must be short enough to minimize image distortions which result from velocity gradients (i.e., strain rate and vorticity). In the present work this is achieved by using smaller fields of view to image those regions with the most intense strain and vorticity fields, as outlined in the preceding section. We have observed that the peak in the correlation field drops to below 50% before strain- and vorticity-induced distortions have an appreciable impact on the velocity vector accuracy, so all vectors with a peak correlation coefficient below 50% are discarded (from whatever sized field of view). If it had not been possible to use shorter Δt

values and data had to be recovered from severely distorted regions, the procedure(s) outlined by Huang, et al. (1993)[52], Tokumaru and Dimotakis (1995)[122], and/or Okamoto, et al. (1995)[91] could have been implemented to account for (and potentially estimate) the velocity field and its gradients simultaneously.

Reference 34 discusses many issues which influence the accuracy of processing MTV image pairs. These issues include the image signal-to-noise ratio and contrast, the grid intersection angle, the width of the grid lines, the size of the correlation source window, the effects of non-Gaussian intensity profiles, non-uniform grid intensities, and interlaced versus non-interlaced detection approaches. For the experimental results presented in this work, the image signal-to-noise ratio is always 5 or higher, with a contrast of at least 120. Except for measurements near the leading edge, where optical constraints dictate an angle of 117^{o}, intersection angles are all approximately 98^{o}. Grid pattern scaling is controlled with respect to the image ratio such that thick grid lines are 8 pixels wide, while thin grid lines average 4.5 pixels in width. The intensity profile of our lines is closer to top-hat than Gaussian, and only non-interlaced detectors are used. This combination of parameters in conjunction with the work of Gendrich and Koochesfahani[34] allows us to conclude that u-component errors will be approximately equal to v-component errors and that the error magnitudes for the primitive velocity vectors presented in this work have a 95% confidence interval of 0.1 pixel, that is, the magnitude of the error vector is less than 0.1 pixel for at least 95% of the vectors measured. Furthermore, in most of the experiments performed, the time delay is adjusted to yield a velocity of 1 cm/s per pixel of displacement, so almost all measurements have an error of less than 0.1 cm/s. The worst-case error is 0.15 cm/s. It should be noted that most of the velocity measurements pre-

sented in this work are a composite from many different runs, with the results mapped onto a regular grid (as described in the next section); the accuracy of the composite results is discussed below. Moreover, all quantitative velocity measurements presented in this work have been normalized by U_∞, and the corresponding worst-case error is 0.015 in non-dimensional form.

Additional details regarding the processing of MTV image pairs are presented in the next several paragraphs for the interested reader. The program used to process image pair sequences enforces a limit on the magnitude of each displacement vector. This magnitude is typically set equal to the distance between two adjacent intersections. The Nelder-Mead simplex method (Press, et al., 1988[100]) is used to locate the maximum of the 7th-order polynomial used to fit the correlation coefficient field; this method was chosen because it can be used to maximize any functional form, not just two-dimensional 7th-order polynomials. Image saturation degrades the accuracy of results, and one is most likely to observe saturation at the intersection of two bright lines, the very points which define the centers of our source windows. After the peak of the correlation coefficient field is located, the intensities in the central regions of the source and roam windows are checked. If saturation is detected in either window, that velocity vector is discarded. The bad vector detection scheme of Westerweel (1994)[137] is applied to locate potentially inaccurate vectors during image analysis and predict what those vectors should have been on the basis of their neighbors' velocities. New correlation fields are computed and fitted using these predictions, and if a good vector results, it is retained.

While processing a sequence of image pairs, accurately determined displacement vectors can be used to predict what the next displacement vector ought to be. When such

prior information is available, a second-order predictor uses the last three measurements to estimate the next vector, and the roam window is reduced so that correlation coefficients are computed only for the expected displacement plus a 3 pixel region around that point. If a local peak in the correlation field is not located within this smaller roam window, the prior information is discarded, and the correlation field is computed and processed using the entire roam window domain.

In localized regions of high shear and/or vorticity, the grid can deform significantly in a very short time. Under these conditions it is possible for a higher correlation coefficient peak, one not corresponding to the real location of the displaced intersection, to exist within the roam window. Other than using Westerweel's technique[137], we have found no reliable way to determine "on the fly" whether a velocity vector is bad and needs to be discarded, although an unusually low correlation value or a sudden drop in the correlation peak from one time to the next can indicate that such a situation has occurred. In this case, if prior information was used to compute the potentially bad vector, it is discarded and a new vector is computed using the entire roam window domain. As mentioned above, under no circumstances is a velocity vector retained if the correlation coefficient field's maximum value is less than 0.5.

2.5. Post-processing

Section 2.3 documents how data are acquired from multiple overlapping regions for three different image ratios. The resulting sets of image pairs are analyzed using the procedure outlined in the preceding section, producing a large number of velocity vectors

widely distributed throughout the space and time of the dynamic stall process. This section describes how those data are post-processed to create a regularly distributed set of velocity vectors at specific angles of attack.

MTV data from a single run are, in general, irregularly spaced, which complicates the issues of computing velocity gradients, plotting velocity profiles, etc. In order to regularize our data spatially, we have chosen to implement a method similar to those described by Spedding and Rignot (1993)[116] and Zeldin and Meade (1997).[143] The basis of those papers revolves around fitting a known analytical function to the original data values in the vicinity of each regular grid point. Several different functional forms have been tested, including polynomials, Gaussian windows, and thin-shell splines.[116] We have determined that a two-dimensional polynomial form provides results as accurate as the others, and although simulations suggested that a fourth-order polynomial ought to produce the best results, there is no appreciable difference between using second-, third-, fourth-, or fifth-order polynomials when fitting our experimental data. Consequently the six coefficients of a second-order two-dimensional polynomial surface $S(x, y)$ are computed for each velocity component via a least-squares fit of the irregularly spaced data surrounding each regularized point.

We wish to employ a regularly distributed grid of points that rotates with the airfoil and has approximately the same point density as the original data. This is especially true on the suction surface in the vicinity of where the DSV forms, which in our experiments occurs in the range $0.05 \leq \xi \leq 0.3$ and $\eta < 0.6$. A consideration of the regions imaged (Figure 2.10) and the distribution of measurement points within each region (e.g., Figure

2.13(a)) led to the construction of the grid shown in Figure 2.13(b). That grid has the following characteristics: in the less densely measured regions, $\xi < 0.05$ and $\xi > 0.3$, the spacing in the ξ direction is $10c$ (i.e., $1 \times 10^{-2}C$), while in the more densely measured region on the suction surface, the spacing is $3c$. The near-wall measurements on the suction surface are equally dense, so the near-wall spacing in the η direction is 3c, and it gradually increases to 10c for $\eta > 0.084$. Since the flow field was only measured over the forward third of the airfoil, the 206×52 regular experimental grid only covers the region bounded by $-0.35 \leq \xi \leq 0.35$ and $0 \leq \eta \leq 0.264$. Obviously the regular grid point density is higher than the original point density in the near-wall regions for $\xi < 0.05$ and $\xi > 0.3$, as well as for $\eta > 0.084$ in the range $0.05 \leq \xi \leq 0.3$. This is an unfortunate side effect of the C-grid topology chosen, but the regularization process described in this section can accommodate that complication while mapping the unmodified data points onto this regular grid.

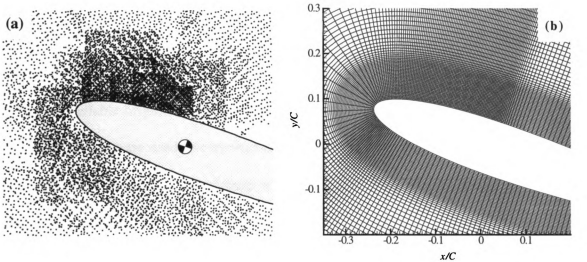

Fig. 2.13: (a) Original data measurement locations for one representative angle of attack (α = 19°. Ω^* = 0.1). (b) The regular grid onto which those data points are mapped.

The local grid spacing determines the size of the region from which data points are drawn for computing the velocity at a regular grid point. An adequate number of irregularly spaced data points must be available to fit the surfaces $S_u(x, y)$ and $S_v(x, y)$ from which the regularized velocity components are derived, and the distribution of initial data points is examined about each regular grid point to ensure that the following criteria are satisfied. To prevent extrapolation into areas where data are unavailable, at least one original data point must be located within 1.5 times the local grid spacing of the regular point under consideration. A factor greater than unity is used to accommodate those regions discussed above where the grid spacing is more dense than the original point density. The order of the polynomial used to compute $S_u(x, y)$ and $S_v(x, y)$ dictates the minimum number of data points required for a satisfactory fit. Unmodified points are drawn from as far away as 9 times the local grid spacing, and at least 9 irregularly spaced data points must be found in the vicinity of each regular point. Velocity vectors are computed at each regular grid point only when all of these criteria are satisfied.

Temporal regularization or phase averaging can be accomplished in two different ways: (1) data from each experimental realization can be mapped onto the regular grid described above, then those grids could be phase averaged using standard methods, or (2) all of the available original data points can be divided into temporal phase bins, then the data from each bin are used to construct one regularized grid. The first approach has the advantage of allowing one to compute statistics on the averaged quantities, but a large amount of smoothing is caused by the processes of first interpolating the data onto a regular grid then averaging. In addition, the interpolation process must use values farther away from each regular grid point in order to have enough data to construct acceptable surfaces

$S_u(x, y)$ and $S_v(x, y)$ — causing smoothing to be performed over a significantly larger region. When using the second approach, no convenient way exists to compute statistics regarding the averaged values, and a highly repeatable flow field is required, but smaller features can be resolved as a consequence of less smoothing, and less storage and compute time is required to implement this approach. In Section 4.1 we show that our flow field is repeatable enough to use this approach, additional details of which are described next.

Grids of regular points are constructed every quarter of a degree, and the corresponding phase bins are 0.25° wide, centered on these angles of attack. This is just slightly more than the change in angle of attack during the delay between images, Δt, for the 3.5 cm field of view data acquired at the highest pitch rate, as seen in Table 2. In addition to the irregularly spaced data measurements put into each phase bin, a set of velocities at the wall are also computed for that bin's nominal angle of attack and pitch rate, and those vectors are added to the original data point pool before any regularization is performed. When mapping irregularly spaced data onto the regular grid, between 80 and 120 points are typically found to be close enough to each regular grid point (according to the criteria discussed above), but no more than 170 points are used in each fit, and individual

Table 2: Exposure times, delay times, and change in angle of attack during the delay time for all fields of view and pitch rates.

field of view (cm)	exposure time (ms)	delay time, Δt (ms)	$\Delta\alpha$ during Δt for the indicated pitch rate		
			0.1	0.2	0.4
3.5	0.5427	8.6496	0.08°	0.16°	0.33°
2	0.3816	4.5156	0.04°	0.09°	0.17°
1	0.1908	2.0034	0.02°	0.04°	0.08°

unmodified data points can, of course, be used in the determination of the velocities at several regular grid points. As seen in Figure 2.13, the density of original data points is lowest near the nose, so more points from farther away are used to estimate each regular point, resulting in higher levels of smoothing near the nose than elsewhere. This is especially apparent in the vorticity distributions presented in Chapter 4.

Once the unmodified data are mapped onto a regular grid, a second-order accurate central difference scheme is used to compute velocity derivatives, then vorticity and strain rate are computed according to:

$$\omega_z = \frac{\partial v}{\partial x} - \frac{\partial u}{\partial y} \tag{11}$$

$$\tau = \frac{\partial v}{\partial x} + \frac{\partial u}{\partial y} \tag{12}$$

Since these variables are the sum or difference of two velocity gradients, the uncertainty is the same for both of them. An analysis of the strain rate at point 0 in the sketch below yields the magnitude of this uncertainty:

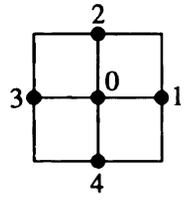

$$\tau_0 = \frac{\partial u_0}{\partial x} + \frac{\partial v_0}{\partial y} = \frac{u_3 - u_1}{2h} + \frac{v_2 - v_4}{2h} + O(h^2) \tag{13}$$

$$(\delta\tau_0)^2 \approx \left(\frac{\partial \tau_0}{\partial u_3}\delta u_3\right)^2 + \left(\frac{\partial \tau_0}{\partial u_1}\delta u_1\right)^2 + \left(\frac{\partial \tau_0}{\partial v_2}\delta v_2\right)^2 + \left(\frac{\partial \tau_0}{\partial v_4}\delta v_4\right)^2 \tag{14}$$

$$\delta\tau = \delta\omega_z = \frac{\delta u}{h} \tag{15}$$

Equation (15) contains the assumptions that the errors in u and v are identical at points 1-4 and that errors of $O(h^2)$ are negligible. Using the worst-case numbers $\delta u = 0.15$ cm/s and $h = 3c$, this uncertainty is 4.2 s^{-1} or 5.0 when normalized by U_∞ and C. This is approximately 1% of the peak vorticity levels encountered in our experiments. The circulation-

based vorticity computation technique of Abrahamson and Lonnes (1995)[1] could be applied to our data, as could the adaptive technique of Lourenco and Krothapalli (1995).[74] While both techniques would have yielded marginal improvements in our estimates of ω_z, a finite-difference approach would still have been required to compute the strain rate. Because a finite-difference approach was required, and since the uncertainty in the finite-differenced vorticity estimates is quite low, we applied the central-difference scheme analyzed above to estimate both vorticity and strain rate.

We must acknowledge that we are computing derivative values using an averaged velocity field, which is different from computing the average of N estimates of a derivative quantity. Because of the different levels of smoothing associated with the two methods of phase averaging discussed above, it was felt that comparable estimates of the instantaneous vorticity and strain rate fields could not be obtained from individual realizations of unmodified data. Another approach can be employed to obtain estimates of the average derivative quantities from the original data, though. The x- and y-derivatives can be computed from $S_u(x, y)$ and $S_v(x, y)$, the second-order surface fits of the irregularly-spaced u- and v-velocity component data as described above (pp. 65-67). The finite-differenced results display sharper features with peak values typically 10% higher than those produced by differentiating the surface fit, suggesting that the finite-difference approach yields results comparable to those that would be obtained using a real average of the instantaneous data but with less smoothing of the data.

In this flow field the edge of the boundary layer is most accurately determined by locating where the difference between the measured velocity profile differs from that of the inviscid profile by some small amount. As the boundary layer thickens and leading-

edge separation begins, computing the inviscid velocity field becomes more and more difficult, rendering this approach impractical for estimating δ. Recognizing that the freestream fluid is irrotational, we have chosen to estimate the boundary layer thickness by locating the point where the vorticity magnitude drops below 10 s^{-1}, although the value of δ is relatively insensitive to cutoff values between 5 s^{-1} and 25 s^{-1}. The tangential velocity component at $\eta = \delta$ is used for normalizing δ^* and θ. Trapezoidal-rule integration is performed when computing quantities like δ^*, θ, and the vorticity flux above the airfoil. The worst-case error in all four of these quantities is approximately equal to half the fine grid spacing, $1.5c$, since the uncertainty in the boundary layer thickness is so much larger than the contributions attributable to errors in the integration or the velocity estimates.

2.6. The Experimental Facility

Experiments are conducted in a closed-return water tunnel using a fiberglass NACA 0012 airfoil pitching about its quarter chord. This section describes the water tunnel and its performance, the airfoil assembly and control mechanisms, along with the remaining experimental details which have not been covered in proceeding sections.

The water tunnel is a 10,000 liter closed-return facility with a 61 cm × 61 cm × 244 cm test section; see Figure 2.14. The flow management section is followed by a 6:1 contraction which is symmetric with respect to our data acquisition plane, a vertical plane located in the center of the test section. The airfoil pitch axis is located 120 cm downstream of the test section inlet, 30.5 cm above the floor of the tunnel; additional details regarding the airfoil assembly are discussed below.

To prepare the facility for MTV experiments, the tunnel is first filled with deionized water, then 300 m*l* of 1-BrNp are added, followed by 1.3 kg Gβ-CD and 52 liters of cycOH. The melting point of cycOH is 25°C, which is slightly above ambient in our laboratory, so the alcohol must be melted before it can be added to the tunnel. Once mixed, however, there is no problem with the alcohol refreezing. After all of the components have been added, the tunnel is operated continuously for approximately 50 hours to ensure the mixture's homogeneity. After that time the kinematic viscosity is measured and found to be $\nu = 0.0095\ cm^2/s$. A 12.0 cm airfoil in this mixture with a 10.0 cm/s freestream velocity has a chord Reynolds number $Re_c = 12{,}600$.

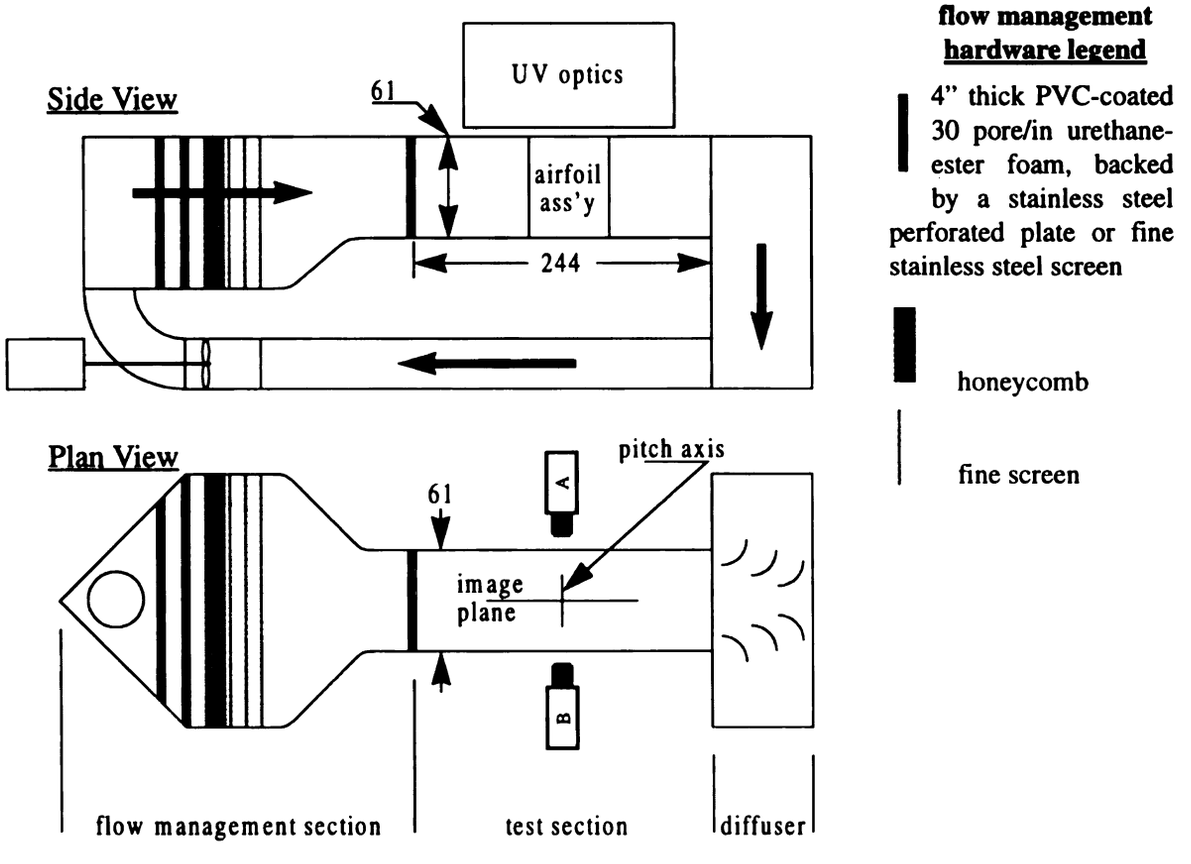

Fig. 2.14: Water tunnel schematic. Locations of the cameras, image plane, and pitch axis are shown in the plan view. Test-section dimensions are given in (cm).

The tunnel's impeller is driven by a 20 HP motor controlled by a Tosvert 130H1 variable torque motor controller. If the motor is operated at 5.6% of its maximum RPM, a freestream velocity of 10.0 cm/s is generated within the test section when the airfoil assembly is present. The airfoil was removed, and the tunnel freestream velocity was measured using MTV at many widely separated points throughout the test section immediately prior to the experiments described in the present work. The time between exposures, Δt, was set so that an average displacement of thirty pixels was obtained while maintaining a 95%-confident sub-pixel accuracy of 0.1 (0.3%). With the tunnel running continuously, a total of 3600 images were acquired at 30 Hz then analyzed. The RMS of those velocities, indicative of fluctuations at frequencies from DC to 15 Hz, was 0.3% for freestream velocities in the range 4 - 14 cm/s. Recalling that a 0.3% accuracy with 95% confidence corresponds to a 0.15% RMS if the data have a normal distribution, we can conclude that the 0.3% RMS in freestream velocity is caused by fluctuations in the flow and not just due to random variations in the measurements. While higher than a typical low-speed wind tunnel (e.g., Mueller, et al., 1983[89]), this freestream turbulence intensity is significantly lower than that cited for most water tunnel studies. Oshima and Ramaprian[92], in particular, quote a freestream turbulence level of approximately 1.2%.

Since MTV is an optical technique, optical access in and around the facility is very important. The plexiglass walls of the test section and airfoil assembly (described below) block ultraviolet radiation but pass visible light, allowing two-detector data to be acquired using cameras mounted on either side of the test section. The lens and mirror arrangement shown in Figure 2.7 is mounted on optical rails above the test section, and quartz windows are located at the upper surface of the water to permit the UV laser beam to enter the test

section without being absorbed by a plexiglass window or diffracted by a free surface. Since laser access is restricted to one direction and the NACA 0012 profile is symmetric with respect to its chord line, the airfoil is pitched up for suction surface measurements and down for measurements of the pressure surface. For flow visualizations (e.g., Figure 1.2) an argon-ion laser is used to illuminate a vertical sheet of hydrogen bubbles. The beam is passed through a cylindrical lens and reflected upward through the floor of the test section to produce a laser sheet in the plane of the hydrogen bubbles. In this case the airfoil is pitched down for visualizations of the suction surface and up when the pressure surface is to be visualized.

The airfoil assembly is depicted in Figure 2.15. The airfoil itself has a 12 cm chord (C) and a 48.5 cm span (b). It is constructed of a fiberglass laminate designed for minimal deformation even with a lift coefficient of 7 at Reynolds numbers around 10^5. After layup in an aluminum mold and autoclaving overnight, the airfoil is slightly oversized; it is then sanded to smooth the surface and to match the NACA 0012 profile. The thickness varies less than $0.84c$ from the nominal profile over the entire airfoil. Bearings mounted in the outside side walls support the stainless steel pitch axis, which passes through the airfoil's quarter-chord point. Circular end plates fit precisely into cut-outs in both inner side walls, allowing the airfoil to rotate without scratching the side walls. Two hollow graphite rods connect the stepper motor and one end plate such that a 1° rotation of the motor produces a 1° change in angle of attack. Additional details of the airfoil assembly's design and construction can be found in Smiljanovski (1990).[114]

For nominally two-dimensional studies on the performance of an airfoil section, the aspect ratio of the wing used in the study is an important factor ($AR \equiv b/C$); the larger

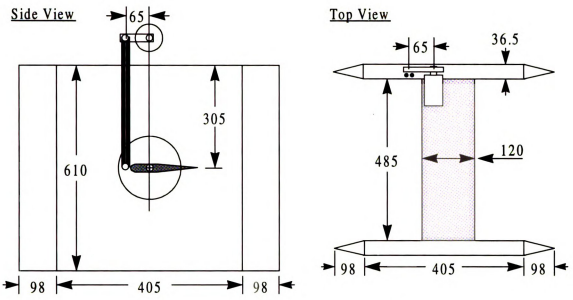

Fig. 2.15: Airfoil assembly schematic.

the aspect ratio, the more uniform the flow is along the span of the model. Additionally as a model pitches up, it blocks the flow through the test section, causing significant local variations in pressure and somewhat less significant changes in lift and drag. Katz and Walters (1995)[63] discuss the effects of blockage, concluding that a 10% blockage causes a peak decrease in C_p of approximately 0.2 as a consequence of blockage-induced increases in the freestream velocity. Table 3 presents the aspect ratio and test section height-to-chord (*H/C*) ratios for several of the studies reviewed in Chapter 1. It should be noted that a 10% blockage is obtained at $\alpha = 30°$ for $H/C = 5$, and 30° is beyond the angle of attack at which leading edge separation begins for all of the pitch rates studied in this work.

Accurate control over the angle of attack is an essential requirement of any dynamic stall experiment. Except for studies conducted in tow tanks (e.g., Shih, et al.[112]) or where the pitch axis was variable (e.g., Helin and Walker,1985[47]), stepper or servo

motors were used to control the angle of attack in almost all of the papers surveyed (e.g., refs. 2, 4, 19, 32, 61, 62, 92, and 136). In our airfoil assembly a KXA amplifier and DC servo motor combination from PMI Motion Technologies is driven by a Galil DMC-1030 control system. The DMC-1030 is a PID controller, operated with the parameters shown in Table 9 (see Appendix I). The position of the motor is monitored using a 10,000-count optical encoder, giving an angular resolution of 0.036°. As shown schematically in Figure 2.9, the motion controller records the airfoil's position each time the laser pulses, i.e., at 30 Hz. Central differencing is used to compute pitch rate values from a time series of such measurements, and the resulting resolution in Ω^* is 0.0056.

Figure 2.16 shows the motion history and pitch rate of every measurement pre-

Table 3: Wing aspect ratio and tunnel height-to-chord ratios for nominally 2D studies.

Reference	*AR*	*H/C*
Jumper, Schreck, and Dimmick (1987)[60]	0.25	3.0
Francis and Keesee (1985)[32]	1.3	4.5 and 6.0
McCroskey, Carr, and McAlister (1976)[80]	1.6	2.5
Acharya, et al.[2,4,61,62]	2.0	2.0
Conger and Ramaprian (1994)[19]; Oshima and Ramaprian (1997)[92]	2.0	3.0
McAlister and Carr (1978)[78]	2.1	3.0
Gendrich, et al. (1992[37], 1995[38]) and the present work	4.0	5.1
Walker, Helin, and Chou (1985)[136]	4.0	6.0
Shih, et al. (1992)[113]; Shih, et al. (1995)[112]	5.5	2.4
Lorber and Carta (1988)[73]	5.5	5.5

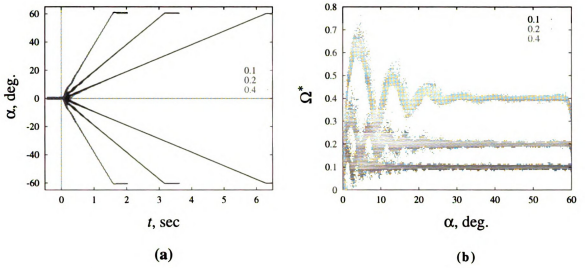

Fig. 2.16: (a) Motion history and (b) pitch rate for all of the experimental data presented in this work. The standard deviation in Ω^* is approximately 0.004 for all three pitch rates once the initial acceleration is damped out.

sented in this work. Although it is rare to find plots of α versus t in the literature, our motion histories are comparable to those presented by Francis and Keesee (1985)[32], Lorber and Carta (1988)[73], and Acharya and Metwally (1990)[2], all of whom recorded a brief acceleration period at the beginning of the motion, small deviations from a constant pitch-rate profile, and a slight overshoot once the maximum desired angle of attack had been reached. No plots of pitch rate versus α have been presented in any of papers referenced in this work, so no comparisons can be drawn between the data in Figure 2.16(b) and that of other researchers. It should be noted that the scatter in Figure 2.16(b) is an unfortunate artifact of the plotting method and the discrete nature of the data; the data are in fact very tightly clustered about the mean values, with a standard deviation in Ω^* of approximately 0.004 for all three pitch rates once the initial acceleration is damped out.

Before any experiments were run, the reference angle $\alpha = 0°$ had to be input into the motion controller; this followed immediately after the tunnel's freestream velocity had

been calibrated. With the target affixed to the airfoil, the streamwise direction of the target was precisely aligned with the freestream, and that angle of attack was recorded by the controller. An error up to 2 counts (0.072°) might be associated with this alignment, however the alignment was not disturbed during the 16 weeks of data acquisition, so there are no errors associated with resetting $\alpha = 0°$ at any point during the experimental cycle.

A standard procedure was followed to take data for each region, i.e., the squares marked with Roman numerals in Figures 2.10(b)-(d). Because of disk storage limitations, only one region could be investigated each day. At the start of the day, water was added to replace the 5-15 gallons that had been lost to evaporation the previous day; 1-BrNp was added if needed to maintain a saturated solution; and 18 liters of cycOH were added once after 8 weeks to replace what had been lost to evaporation. Changes in kinematic viscosity due these additions were negligible. The cameras were positioned and aligned using a target affixed to the airfoil, then the target was removed and the laser grid was set up. Each laser grid (there were five per region) was recorded with $\Delta t = 0$, and the intersection locations were checked against previously recorded grids for that region to ensure that the positions were unique; the beam blockers were moved laterally until another unique grid was obtained. The relative alignment of the cameras was fine-tuned using these zero-delay grids, and they comprised our estimates of the camera displacement field, $D_x(x,y)$ and $D_y(x,y)$ as discussed in Section 2.3 (p. 52). The DDG was set for the appropriate delay, Δt, and the B-camera gain was adjusted to obtain a contrast of about 220 for the delayed images; the A-camera exposure remained constant throughout, so its gain did not need to be adjusted. Programs controlling the airfoil motion and image recording were started, and the airfoil pitched up then down at the three different pitch rates with the

appropriate start times for the pitching motion with respect to the field index from camera A. The recorded airfoil positions were checked against previously recorded α time series, and each image was checked to ensure that no errors had occurred in image acquisition or storage. If errors had occurred, the experiment was re-run. After running experiments for five different grid positions, one final camera displacement field was obtained, and the six different $D_x(x,y)$ and $D_y(x,y)$ estimates were compared. The camera displacement field is a smoothly varying function over the entire image, which is seen as a consistent set of $D_x(x,y)$ and $D_y(x,y)$ vectors. If the relative alignment of the cameras had changed during the course of the experiments, it must have occurred sometime while data were being acquired, invalidating the camera displacement field. In this case discontinuities were seen when comparing the 6 estimates of $D_x(x,y)$ and $D_y(x,y)$, at which time all of the data were discarded and the experiments were run again. After all checks had been passed successfully, the image data and airfoil positions were written to tape, then verified.

Beyers (1995)[8] discusses sources of errors in high-alpha experiments, including dynamic support interference, unsteady wall interference, test facility interference, Reynolds number effects, flow quality, and freestream turbulence levels. In the design and operation of our tunnel and model, we have successfully attempted to minimize potential errors from all of these sources.

Chapter 3

COMPUTATIONAL PROCEDURE

This chapter describes the computational methodology which was employed to simulate the dynamic stall flow field. A fully-compressible two-dimensional Navier-Stokes solver was used, based on the implicit factored scheme of Beam and Warming (1978)[7], who wrote: "Traditionally, implicit numerical methods have been praised for their improved stability and condemned for their large arithmetic operation counts." The original code was developed by Visbal (1986a)[127], with subsequent modifications that are discussed below.

As published, the Beam-Warming algorithm is non-iterative and spatially factored, so that second-order accurate spatial cross-derivatives can be explicitly evaluated in an efficient manner. Beam and Warming[7] proposed that second-order accurate central differences be used to evaluate temporal derivatives implicitly, making this a 3-time-level scheme. When simulating the dynamic stall flow field, Visbal and Shang (1989)[133] found that errors caused by the approximate spatial factorization far outweighed errors associated with using Euler implicit temporal derivatives instead of a second-order accurate scheme, as long as the time step size is reasonably small![133] As implemented, the algorithm is therefore 2nd-order accurate in space and first-order accurate in time, which is consistent with the practice of almost all researchers in the field. Of the literature

reviewed, only Ekaterinaris, et al. (refs. 27, 26, and 126) and Ghia, et al.[39] used third-order accurate upwind-biased solvers, but Ekaterinaris and his co-workers incorporated thin-layer approximations into their model, while Ghia and her co-workers were attempting to reduce unwanted oscillations by using a more accurate integration scheme.

In order to facilitate the comparison of computational results and experimental flow visualizations, particle tracking was also incorporated into the code. A first-order marching scheme was implemented to track the motion of 30,000 particles. Bi-linear interpolation was used at each time tick to extract the velocity vector $\underline{U}$ at each point's location from the neighboring computational grid nodes, and the position of each particle was incremented by $\underline{U}\Delta t$, the distance travelled by that particle during the computational time step Δt. Initial locations were chosen such that the particles would simulate bands of hydrogen bubbles that originated from a pulsed wire some distance upstream. While the airfoil remained at rest, time was advanced until the leading edge of the "virtual hydrogen bubbles" had passed downstream of the airfoil's trailing edge. Immediately before the airfoil started to pitch up, a small cluster of particles was added in the vicinity of the quarter chord nearest the trailing edge. The motion of these particles emulated experiments in which dye had been injected near the trailing edge, in an effort to discover whether mass transfer from the trailing-edge region influenced the dynamic stall process. Gendrich, et al. (1992[37], 1995[38]) have shown a very good correspondence between these computed "flow visualizations" and those obtained experimentally. For example, the angle of attack marking the first visual appearance of a "bulge" near the nose of the airfoil as the flow separates from the leading edge agrees to about 2.5 degrees between the experiment and computations.

The performance of the solver used in the present study has been extensively documented by Visbal (1986a[127], 1986b[128], 1990a[129], 1991[131]) and Visbal and Shang (1989).[133] Furthermore, the more recent unstructured grid computations of Ghosh Choudhuri, et al. (1994)[40] utilized the same solver, although at higher Mach number and finer grid resolution. The O-grid topology was used in the current work with 203×101 points in the ξ and η directions, respectively (see Figures 2.10 and 3.1); nearly orthogonal grids were generated following the method outlined by Visbal and Knight (1982).[132] The minimum grid spacings were $0.6c$ (i.e., $6 \times 10^{-4}C$) in the ξ direction and $0.08c$ in the η direction. The grid extended 30 chords radially away from the airfoil (i.e., in the η direction), and spatial periodicity was imposed along the O-grid cut by a five point overlap in the ξ direction at the nose of the airfoil. The airfoil surface was no-slip and isothermal.

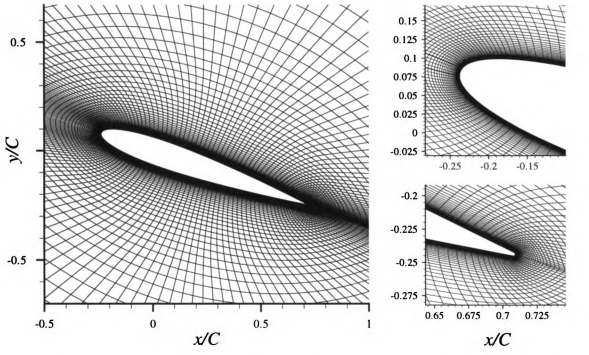

Fig. 3.1: Computational grid in the vicinity of the airfoil. Leading-edge and trailing-edge details are also shown.

Freestream conditions were given along the inflow portion of the far-field boundary, and fully-developed conditions ($\partial[\ ]/\partial x = 0$) were imposed along the outflow boundary.

The resolution of this grid geometry with respect to the dynamic stall problem was tested by Visbal (1986b)[128] and Visbal and Shang (1989)[133], who observed that halving the number of grid points in both directions had a negligible influence on the time history of the airfoil's integrated loads. When compared with the finer grid computations, the difference in lift and drag coefficients for the case $\Omega^* = 0.3$ was less than 1% for $\alpha \leq 40^o$. The worst case occurred for the lowest pitch rate considered here ($\Omega^* = 0.1$); as an example, the lift coefficient changed less than 3% for $\alpha \leq 30^o$ when compared with a coarser grid computation. The majority of the results presented here address the flow behavior up to the onset of leading edge separation and the initial stages of dynamic stall vortex evolution that follow. These phenomena occur over ranges of angle of attack below those mentioned above (for each pitch rate mentioned). On the basis of the integrated loads, we can therefore conclude that the present computations provide accurate simulations for the portion of the flow field discussed here.

As noted in preceding sections, the present study is concerned with $Re_c = 12{,}000$, so we expect the flow to remain laminar over the airfoil, at least through the early stages of leading edge separation. Consequently no turbulence model has been incorporated into our solver. While previous studies have suggested that Reynolds number effects should be quite limited (e.g., Walker, et al., 1985[136]; Conger and Ramaprian, 1994[19]; and Wilder, et al., 1993[138]), it was felt that this should be verified for the present computations. Figure 3.2 shows the time history of lift, drag, and moment coefficients for Reynolds numbers between 8,000 and 20,000. It can be seen that there is effectively no difference between

the three Reynolds numbers for the high pitch-rate case. The unsteady separated region near the trailing edge, which affects these data even when the angle of attack is constant at $\alpha = 0°$, is responsible for the variations observed in the low pitch-rate case, but if those oscillatory effects are smoothed out, it can again be seen that the variation is quite small for a wide range of Reynolds numbers about the one to be studied in the present work. We therefore expect the $Re_c = 12{,}000$ computations to be directly comparable with the $Re_c = 12{,}600$ experimental results presented in Chapter 4.

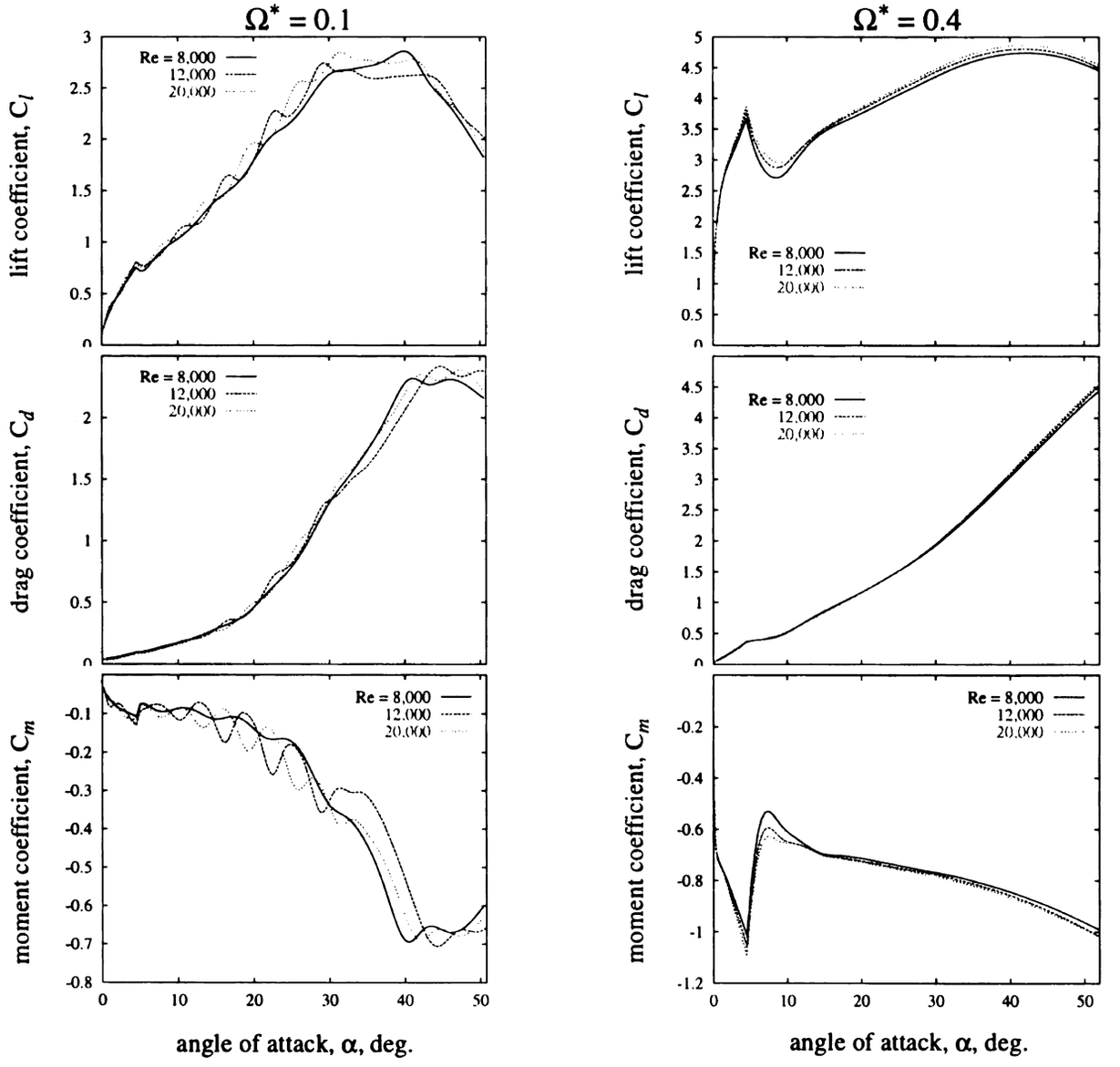

Fig. 3.2: The effects of Reynolds number on lift, drag, and moment coefficients.

The solver used was designed to compute subsonic and supersonic flow fields by numerically integrating the fully-compressible Navier-Stokes equations. As a result, the numerical stability of the solution is degraded when the freestream Mach number is set too low. Because the Mach number of the corresponding experimental study was practically zero, the present numerical study employed the smallest Mach number that still yielded stable results, which is $M_\infty = 0.1$. For this Mach number the maximum density variation was less than 3% at the highest pitch rates, which should enable acceptable comparisons to be made with our water tunnel studies.

In addition to matching the Reynolds and Mach numbers, the airfoil motion profile is also to be matched between the computations and experiments. Although the constant pitch-rate segment of the motion profile is easy to match, the accelerations and decelerations used to achieve the motion depicted in Figures 1.1 and 2.16 are more difficult to simulate. An exponential form of the pitch rate was first studied by Visbal (1986b)[128],

$$\alpha = \frac{1}{2}\left(1 - e^{-\frac{t}{\tau}}\right)\Omega^* \tag{16}$$

and the effects of the acceleration time constant, τ, were investigated. Constant (ON or OFF) accelerations more closely match the motions produced by real physical devices, and the dimensionless time constant associated with such an acceleration is $e \equiv T_a/T_c$, the acceleration period divided by the time required to execute the entire motion in the limit of infinite acceleration (see Figure 1.1). The effects of varying e in a computation were reported by Gendrich, et al. (1995).[38] In both of these studies (refs. 128 and 38), it was found that as long as the acceleration had ended before leading edge separation began, the specific details of the acceleration did not significantly impact the dynamic stall process. In the present work, a value of 0.15 has been used for e.

It can readily be seen that the pitch-rate time history of the experiments shown in Figure 2.16 (b) does not match the idealized pitch-rate profile shown in Figure 1.1. The real pitch rate is in fact a damped oscillation with an amplitude of less than 0.05 by the time leading edge separation begins for all of the pitch rates under study. Since a constant (ON/OFF) acceleration matches the idealized motion profile, and even though it does not exactly reproduce the experimental pitch-rate time history, that type of motion profile is used in the present computations. We expect that since the experimental accelerations damp out before leading edge separation begins (see Section 4.3), a comparison between these computations and experiments is still appropriate.

The correct choice of computational time step size is necessary to minimize computational requirements while producing accurate time-resolved simulations. The results of Visbal (1986b)[128] for $\Omega^* = 0.1$ indicated that if the time step $\Delta t\, U_\infty/C \leq 10^{-3}$, the numerical solution was independent of time step, e.g. the lift coefficient remained unchanged upon halving the time step. This criterion was observed in the current computations as well; the maximum time step sizes were 1×10^{-3}, 5×10^{-4}, and 3×10^{-4} for $\Omega^* =$ 0.1, 0.2, and 0.4, respectively. During the initial acceleration period, the time step was reduced even further to values ranging between 5×10^{-5} and 2×10^{-4}.

Although the algorithm is unconditionally stable, Beam and Warming[7] found it necessary to add fourth-order dissipative terms to the formulation in order to damp out very short wavelengths and enhance the numerical stability of their solution. Our implementation includes implicit and explicit nonlinear dissipative terms as described by Jameson, et al. (1981).[57] Since the added dissipation is of higher order than the accuracy of the method, it does not alter the algorithm's formal level of accuracy. The influence of damp-

ing in our computations was assessed by systematically increasing the damping coefficient. It was found that an increase of damping coefficient by a factor of three resulted in only small changes. For example, the lift and drag coefficients for $\Omega^* = 0.4$ changed by less than 0.6% throughout the entire motion trajectory, see Figure 3.3. The angle of attack at the onset of leading edge separation, and the angles of attack characterizing the occurrence and evolution of the primary zones of reversed flow on the suction surface, varied by less than one degree for all of the cases studied here (Gendrich, et al., 1995[38]).

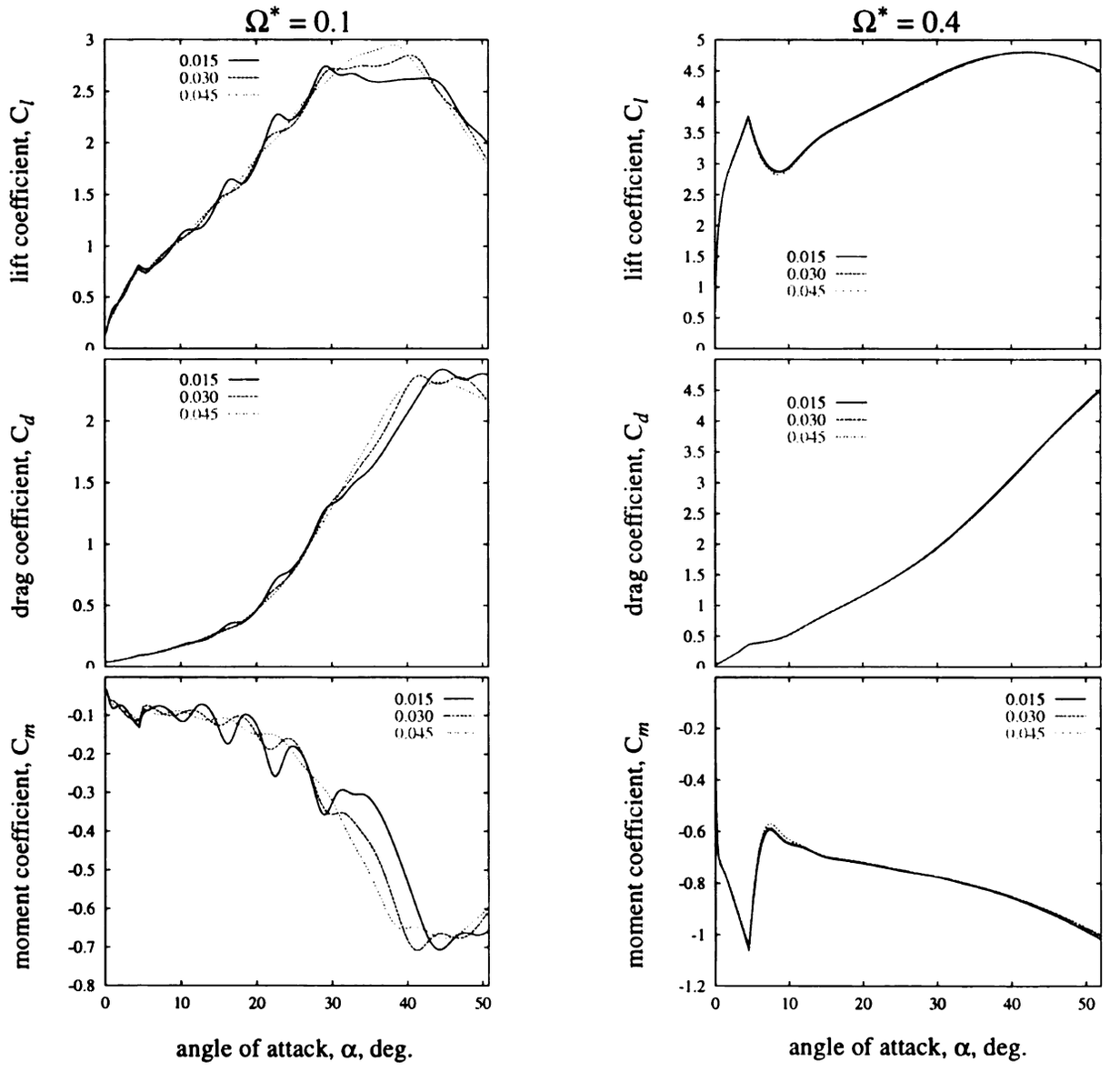

Fig. 3.3: The effects of damping on lift, drag, and moment coefficients.

Once the Reynolds number, Mach number, and level of damping were decided upon, a set of initial conditions had to be constructed such that no spurious transients caused by the initial conditions would influence the dynamic stall results. Initial conditions were established by estimating a velocity at each point in the domain, then advancing time with $\alpha = 0°$ until limit-cycle oscillations were observed in the lift, drag, and moment coefficients, see Figure 3.4. Constant values for these coefficients were not expected, because of the unsteady separated region in the vicinity of the trailing edge on an NACA 0012 airfoil at this Reynolds number. Examination of the ω_z contours indicated that a cyclically consistent distribution of vorticity was being shed into the wake, as observed experimentally. Once a good set of initial conditions had been produced, they were used for the subsequent computations of each pitch rate.

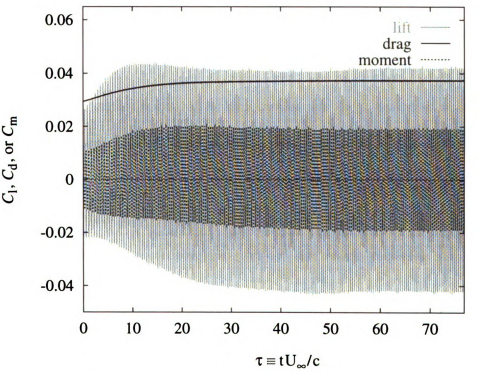

Fig. 3.4: Lift, drag, and moment coefficients at $\alpha = 0°$ while computing the steady-state flow field.

Chapter 4

RESULTS AND DISCUSSION

This chapter documents the results of the experiments and computations which were described in the preceding chapters, focussing on the flow field developments that underlie leading-edge separation. We first investigate whether a stochastic or deterministic model most accurately describes the behavior of the experimental flow field prior to leading-edge separation. This is an important factor to consider when interpreting results that have been phase-averaged using the procedure outlined in Section 2.5. Next comes a discussion of the implications associated with presenting results in an absolute frame of reference versus the rotating frame of reference attached to the airfoil. Previous investigators have published results using both of these frames of reference, and some of the published quantities are frame-dependent, while others depend only weakly or not at all on the chosen reference frame. Experimental results for the lowest pitch rate are then presented to give the reader an overview of the measured dynamic stall process. Subsequent sections address pitch-rate effects and the differences between our experimental and computational results. Where appropriate, we compare our results with the experiments of Oshima and Ramaprian (1997)[92] and the computations of Ghosh Choudhuri, et al. (1994)[40].

4.1. Experimental "Repeatability"

The phase averaging procedure discussed in Section 2.5 produces a time history of the average velocity field during the dynamic stall event. Each average velocity field can be interpreted as an instantaneous realization of some portion of the event, if the flow field develops in the same way each time the experiment is run. If the velocity fields are different from run to run, then a statistical approach must be used to correctly interpret the results. It therefore behooves us to consider how similar the flow field is from one run to the next, so that a proper analysis of the data can be undertaken. In the following discussion, this run-to-run similarity of the velocity fields is called the "repeatability" of the experiment; it should not be confused with the ability of the experimental apparatus to duplicate the same freestream conditions or motion of the airfoil, which has already been discussed in Chapter 2.

Because of the nature of the process used to map our irregularly spaced data onto a set of regular grids (see Section 2.5 and page 67, in particular), it is quite difficult to compute statistics that quantify run-to-run variability in the velocity fields. By presenting a subset of the original velocity vectors, it will be shown that the experimental flow field is in fact highly repeatable, at least through the initial development of the dynamic stall vortex. Representative data are selected from three angles of attack for each pitch rate studied. Although the significance of those angles is discussed starting in Section 4.3, they correspond to: (1) when the reversed flow front has reached approximately $\xi = 0.05$; (2) during the boundary layer eruption which separates the DSV from its feeding vortex sheet; and (3) several degrees later, well after the onset of leading-edge separation, during

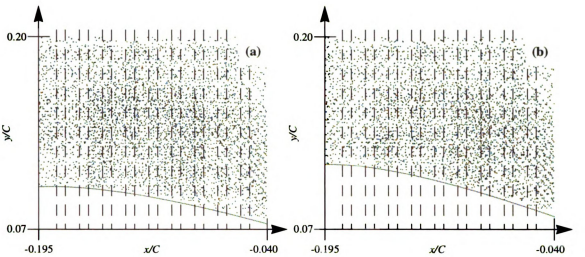

Fig. 4.1: Original measurement locations for two representative angles of attack. The repeatability data plotted in subsequent figures are drawn from narrow bands such as those illustrated here.

the convection and diffusion period of the DSV after its initial formation.

The data plotted in Figures 4.2-4.4 are obtained by extracting original velocity vectors located above the suction surface from narrow bands (6*c* wide) centered on several different *x* locations, namely *x/C* = [-0.9 : -0.5] in increments of 0.05. The starting *x*-locations of the vectors (i.e., the *x*-component of the heads of each velocity vector) are adjusted to be at the center of the bands from which the data were drawn, while the starting *y*-locations are not changed. This allows for easier comparison of vector direction and magnitude, and a feel for the velocity profiles can be garnered by connecting the tips of the individual vectors. The process by which vectors are chosen is illustrated in Figure 4.1 for two representative data sets, $\Omega^* = 0.1$, $\alpha = 19°$ and $\Omega^* = 0.2$, $\alpha = 23.5°$. Each dot indicates where a measurement was made, while the dashed lines delimit the 6*c*-wide strips centered on *x/C* = [-0.9: -0.5]. It can be seen that about 30% of the data points fall within these narrow bands, and these comprise the velocity vectors which are used to construct Figures 4.2 - 4.4.

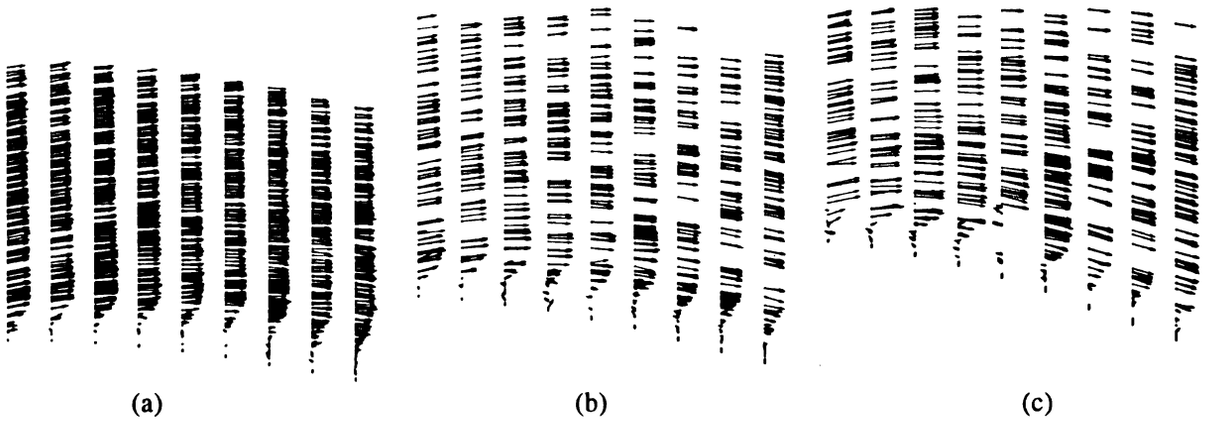

Fig. 4.2: Irregularly-spaced data depicting velocity profiles for when the reversed flow front has reached approximately $\xi = 0.05$. (a) $\Omega^* = 0.1$, $\alpha = 15°$; (b) $\Omega^* = 0.2$, $\alpha = 19.75°$; (c) $\Omega^* = 0.4$, $\alpha = 25.5°$.

Figure 4.2 shows that the flow field is extremely repeatable through this early stage of the experiment. Fewer than 0.1% of the approximately 4,000 vectors plotted in this figure vary by more than 0.9° or 0.1 cm/s from their neighbors. It can also be seen that fewer data points are present in the freestream at the higher pitch rates. This is caused by the higher rate of dropouts that occurs when processing very high-speed vectors in an experiment designed to resolve the low-speed flow near the wall. As implemented, our experimental technique has a dynamic range of approximately 450:1, and this limit was occasionally exceeded in fields of view containing the freestreams of the higher pitch rates.

Figure 4.3 shows a very slight increase in the experimental variability during the next stage of flow field evolution, although a greater level of variation is seen in the $\Omega^* = 0.4$ measurements than is present at the lower pitch rates. It should be noted at this time that the uncertainty in the direction of a velocity vector is dependent upon its magnitude, $\delta\theta = \tan^{-1}(0.015 U_\infty / |\underline{U}|)$ — see page 69. The level of uncertainty is approximately 0.9° for velocity vectors with a normalized magnitude of one, and the uncertainty

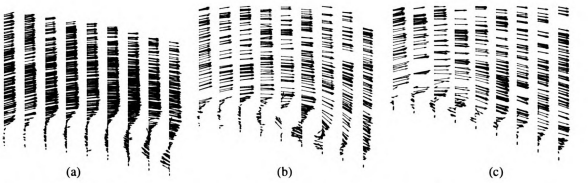

Fig. 4.3: Unmodified data depicting velocity profiles during the boundary layer eruption which separates the DSV from its feeding vortex sheet. (a) $\Omega^* = 0.1$, $\alpha = 19°$; (b) $\Omega^* = 0.2$, $\alpha = 23.5°$; (c) $\Omega^* = 0.4$, $\alpha = 27°$.

increases as the magnitude decreases. It should also be noted that data from at least 80 runs are plotted in each of the Figures 4.2-4.4 (a-c).

Irregularly-spaced data from a later time during the diffusion and convection of the dynamic stall vortex are shown in Figure 4.4. The variability is higher than before in all cases, and there is also a larger increase in variability at the higher pitch rates. Several different factors can contribute to these increases. First, the flow field itself might be this variable. Since the boundary layer breakdown develops very rapidly as will be seen in subsequent sections, the precise location of the DSV and other small-scale shear-layer fea-

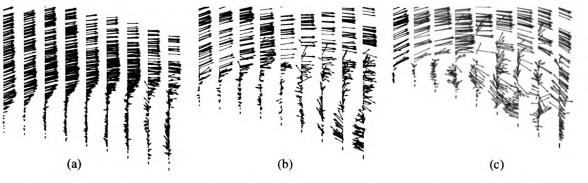

Fig. 4.4: Unmodified data depicting velocity profiles from the growth period of the DSV after its initial formation. (a) $\Omega^* = 0.1$, $\alpha = 22°$; (b) $\Omega^* = 0.2$, $\alpha = 28°$; (c) $\Omega^* = 0.4$, $\alpha = 33°$.

tures vary somewhat from run to run (e.g., see the flow visualizations in Figures 1.2, 4.7, etc.). Instances of this are apparent in Figure 4.4(c), where various centers of rotation can be discerned covering a fairly broad range in both the vertical and streamwise directions. In the regions of higher velocity gradient, the correlation procedure might have produced bad vectors because of excessively high distortions of the intersection region. This is more likely to have occurred in the data from the larger fields of view, as outlined in Section 2.4. In the very high-speed regions, it is also possible that a couple of correspondence errors occurred (see page 48 and also Haralick and Shapiro, 1993[43]) because of the very large travel of the tagged regions during the time between exposures, Δt. It should be noted that these problems appear only well after the onset of leading-edge separation. Since the primary focus of the present work is on developments in the flow field that cause leading-edge separation, these problems are not expected to adversely impact the conclusions discussed below.

The velocity profiles in Figures 4.2-4.4 illustrate several significant features of the dynamic stall flow field, which will be expanded upon in subsequent sections. First, a noticeable velocity overshoot is present at the edge of the boundary layer, but is no larger than what is expected from the inviscid solution of this problem. The velocity overshoot makes the process of estimating the boundary layer thickness and quantities like δ^* and θ more difficult than it is with steady wall-bounded shear flows. In addition, higher pitch rates cause higher velocities outside the boundary layer, while the boundary layer thickness (i.e., roughly 165% of the distance from the wall up to the largest velocity vector, see especially Figure 4.2) appears to be relatively independent of pitch rate at the different stages of flow evolution. This results in higher velocity gradients in the boundary layer,

and therefore higher vorticity and strain levels at the higher pitch rates. While flow visualizations suggest the presence of significant activity in the separated zone near the leading edge (e.g., Figure 4.8), it can be seen in Figure 4.4 that the region is in fact fairly quiescent, which is typical of most separated flows.

4.2. Frame of Reference

This section discusses the differences between results presented in the absolute or laboratory frame of reference, the (x, y) coordinate system, versus the rotating frame of reference of the airfoil, the (X, Y) coordinate system. It will be seen that the differences in the velocity and vorticity field are very slight, although significant changes in the streamline topology can be caused by transforming from one coordinate system to the other. Since all previous results with which we wish to compare have been presented in the airfoil's frame of reference, most data in subsequent sections will also be presented in that frame.

Consider first the transformation from the (x, y) coordinate system to another fixed frame of reference (x', y') which at this instant happens to be aligned with X and Y, the coordinate axes rotating with the airfoil. The spatial coordinate transform from (x, y) to (x', y') involves a rotation of both coordinates and velocity vectors through an angle of $-\alpha$, but the vector magnitudes and angles with respect to the airfoil surface remain the same, and the surface velocity itself is non-zero. Now consider the transformation from (x', y') to (X, Y) coordinates. In this velocity transform solid body rotation is added, which changes both the direction and magnitude of every velocity vector and produces a surface velocity

of zero. The combined transformation from the absolute frame of reference (x, y) with velocities (u, v) to the rotating coordinate system (X, Y) with velocities (U, V) can be written as follows:

$$X = x\cos(\alpha) - y\sin(\alpha) \tag{17}$$

$$Y = x\sin(\alpha) + y\cos(\alpha) \tag{18}$$

$$\frac{U}{U_\infty} = \frac{u}{U_\infty}\cos(\alpha) - \frac{v}{U_\infty}\sin(\alpha) - 2\Omega^* Y \tag{19}$$

$$\frac{V}{U_\infty} = \frac{u}{U_\infty}\sin(\alpha) + \frac{v}{U_\infty}\cos(\alpha) + 2\Omega^* X \tag{20}$$

The present study is concerned exclusively with regions that are within $0.3C$ of the pitch axis, so the maximum magnitude of the added velocity vector is 0.24 in non-dimensional form. This compares with velocities outside the boundary layer which range between 1 and 4.5. In addition, the tangential velocity added in the boundary layer regions of interest is significantly smaller than the global maximum of 0.24 for all pitch rates.

Strain rate is invariant under the transforms (17)-(20), and when transforming to the rotating frame of reference, a constant value equal to $2\Omega^*$ is added to the entire vorticity field. In non-dimensional terms the maximum added vorticity is 0.8, well below the uncertainty of our vorticity estimates, which is 5 (see p. 69).

An analysis of streamline patterns in the flow field can be used to locate centers of rotation, stagnation points, and the boundaries of any recirculating regions that might be present. Centers of rotation (nodes or foci) and stagnation points (saddles or half-saddles) comprise the critical points in which we are interested, see Figure 4.5, which is used with permission from Perry and Chong (1987).[95] However, a streamline pattern is dependent upon the frame of reference chosen for the velocity vectors. Perry and Chong present a comprehensive discussion of the streamline and critical-point analysis which will be

applied in subsequent sections, but several key aspects of their discussion are summarized here. In stationary frames of reference, or in non-inertial reference frames in which the observer is at rest with respect to the surface, critical points on a no-slip boundary are located where the vorticity is zero and the pressure and vorticity gradients are both finite. No such straightforward rules exist for finding critical points at free-slip boundaries in non-inertial reference frames (i.e., on dividing streamlines), which is unfortunately where MRS points will be located if they exist in our flow field.

In strictly two-dimensional, incompressible flows, all possible critical points are located on the *Y*-axes of Figures 4.5(a) and (b). This means that closed recirculating

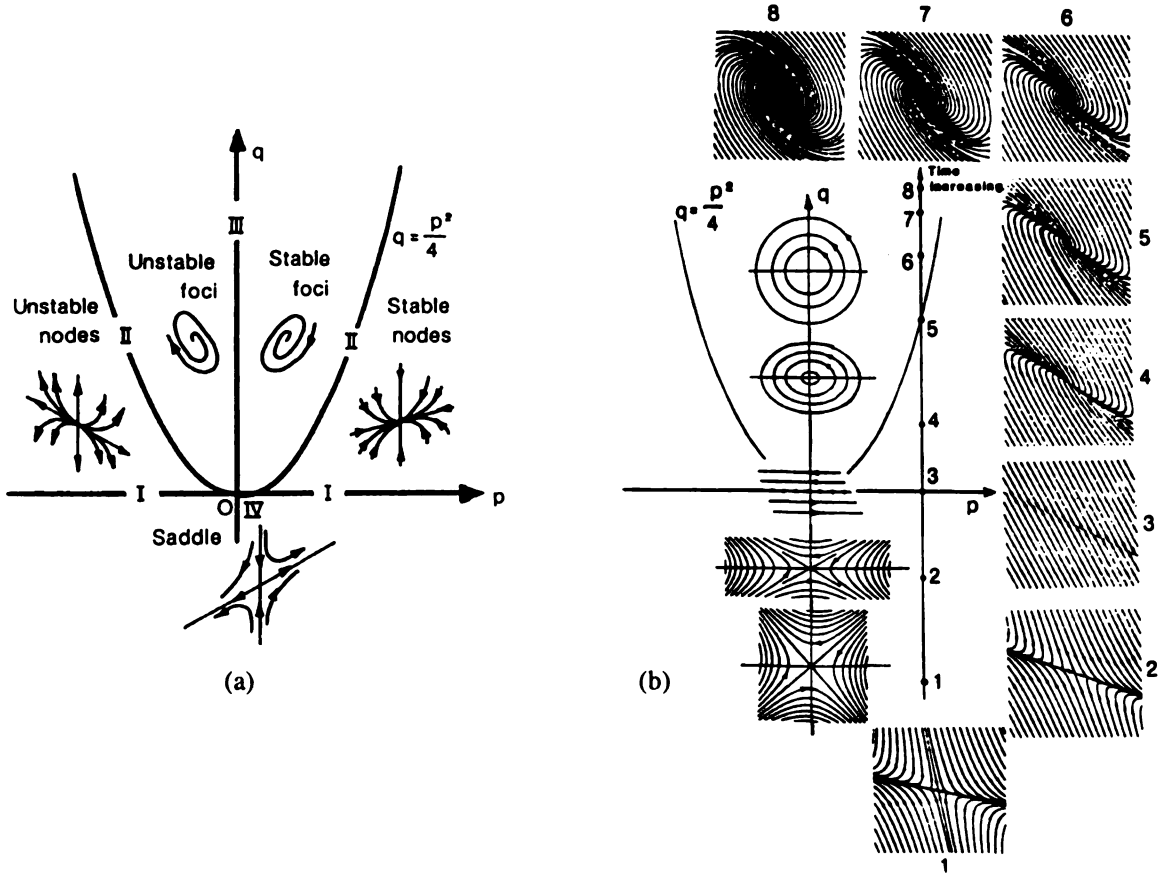

Fig. 4.5: (a) Streamline patterns that define the various critical points in a flow field, and (b) the formation of a closed recirculation region from a vorticity field experiencing non-axisymmetric stretching. (copyright © 1987 by Annual Reviews — reprinted with permission).

regions must rotate about centers, not foci. The presence of a focus, which is observed in some of our experimental results, suggests that the flow is three-dimensional. The reader is reminded that streamline patterns, and hence the appearance of critical points, is dependent on which frame of reference is chosen. It is therefore difficult to reach an unambiguous conclusion regarding the two- or three-dimensional nature of a flow field on the basis of streamline plots.

Perry and Chong (1987)[95] cite Davey (1961)[22] and Hunt, et al. (1978)[55], who first applied the Poincaré-Bendixson "hairy sphere theorem" to the topological study of fluid flows. This theorem states that the Euler characteristic, i.e., the number of nodes plus foci minus the number of saddles, must equal two in a flow field containing an object which is topologically equivalent to a sphere. Our airfoil assembly is most readily modeled as a sphere with two holes in it; consequently its Euler characteristic is zero. An important implication of this theorem is that the formation of a new center or focus is always associated with the formation of a new saddle at some other location in the flow.

Finally, in unsteady flows with closed recirculation regions, the locations of the peak vorticity, the associated pressure minima, and the centers of rotation are all offset with respect to one another. Figure 4.5 documents the streamline patterns associated with each of the five different kinds of non-degenerate critical points, and it also shows how a closed recirculation region can develop in a region of vorticity undergoing asymmetric stretching.

Figure 4.6 illustrates one portion of the dynamic stall flow field which is most strongly influenced by the transformation to the rotating frame of reference: the leading-edge region of the suction surface with $\Omega^* = 0.4$. A careful comparison of the velocity

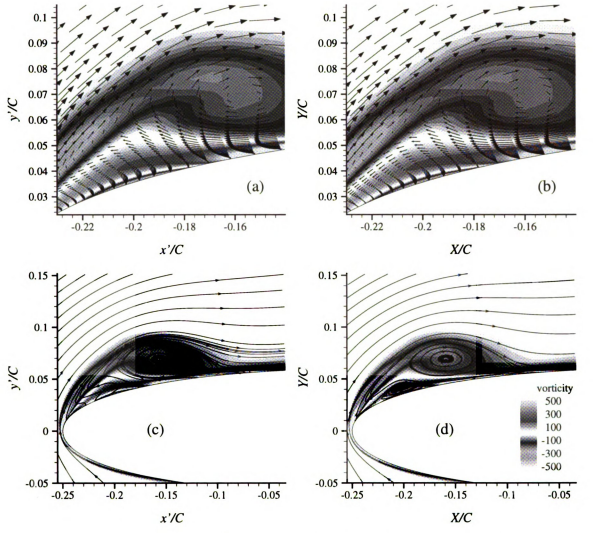

Fig. 4.6: Computational results for $\Omega^* = 0.4$, $\alpha = 36°$. Although the velocity vector field varies only slightly between (a) an inertial frame of reference (x', y') and (b) the rotating frame of the airfoil (X, Y), the streamline patterns vary significantly between those two frames as seen in (c) and (d), respectively.

fields (Figures 4.6a and b) reveals the very slight angular differences, especially in the near-wall region where the vector magnitudes are low. On the other hand, the differences in the streamline patterns shown in Figures 4.6(c) and (d) are much more readily ascertainable. Streamlines intersect the wall when it is in motion, but they run parallel to the wall (except at critical points) when the wall is fixed. A large node, the secondary recirculating region, is seen in the latter frame of reference but not in Figure 4.6(c). The saddle associ-

ated with the large primary recirculating region is present at $x/C = -0.07$ in the absolute frame, while it is well outside our field of view in the rotating frame.

As mentioned earlier, streamlines will only be computed in the rotating frame of reference for comparison with the results of previous studies. If the (X, Y)-coordinate system were "moving with the separation point," then critical points located in regions of zero shear would define MRS unsteady separation and reattachment points as discussed in Section 1.3. We will see in subsequent sections that none of the critical points in the rotating frame satisfy the zero shear criterion, as also noted by Ghosh Choudhuri, et al. (1994)[40].

4.3. Measurements of Dynamic Stall, $\Omega^* = 0.1$

This section presents experimental results documenting the development of the dynamic stall flow field for the lowest pitch rate considered in this study, $\Omega^* = 0.1$; the effects of pitch rate will be considered in Section 4.5. First hydrogen bubble flow visualizations will be used to provide a global context for discussions of the suction-surface vorticity field near the leading edge. Enlarged views of the measurement domain, outlined by the small black rectangles in Figures 4.7 and 4.8, show the specifics of the velocity and vorticity fields during the onset of leading-edge separation and the initial stages of DSV growth and convection. A sharp reduction in the rate of convective vorticity flux will be shown to accompany the development of the DSV, indicating that a strong local accumulation of vorticity begins at that time.

The bands of hydrogen bubbles used to visualize the flow originate at a stainless steel wire with a diameter of 51 μm located about $20c$ upstream of the leading edge.

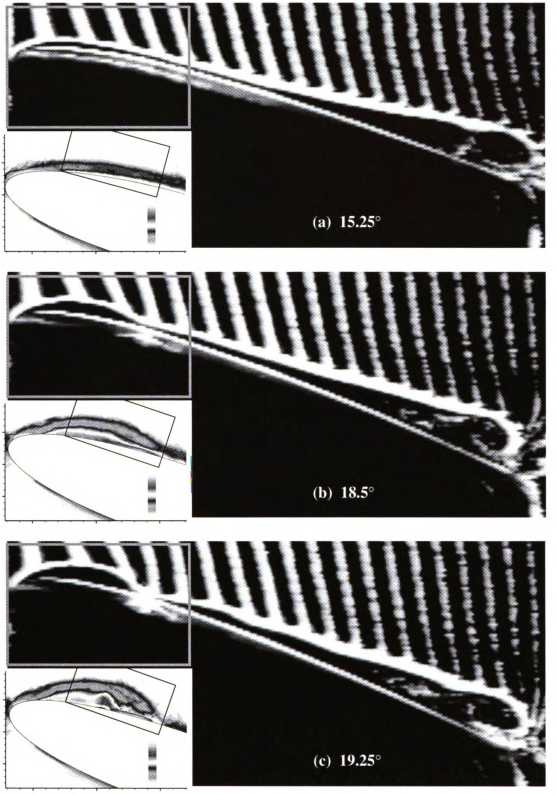

Fig. 4.7: Flow visualizations and vorticity field during the initial stages of leading-edge separation.

Hydrogen bubbles are generated at the wire by periodically imposing a voltage between the wire and an electrode downstream. Since the bubbles originate upstream of the airfoil, they typically coalesce into a lateral line delimiting the edge of the boundary layer. A visible gap between this line and the surface of the airfoil denotes a thickening of the boundary layer from its original state, especially near the leading edge, where the boundary layer is originally quite thin.

During the initial stages of development (not shown here), the flow is attached, although the flow visualizations reveal a thickening of the boundary layer that starts in an area near the trailing edge and grows toward the leading edge. In Figure 4.7(a) we see that this increase in boundary layer thickness is associated with a very thin region of positive (counterclockwise) vorticity that extends downstream from $x/C = -0.15$. Overlying this is the negative (clockwise) vorticity which originates near the leading edge and convects downstream. Figure 4.7(a) shows that this negative vorticity is concentrated in a thin region which smoothly follows the contours of the airfoil's surface despite the presence of the reversed-flow region. At this stage we can therefore say that the flow is detached but not separated (see page 35).

A "bulge" is forming near the leading edge in Figure 4.7(b), and Brown (1992)[10] used this as his indicator of the onset of leading-edge separation. This is associated with a streamwise-varying growth in the reversed-flow region and the corresponding development of a fairly sharp bend in the overlying vortex sheet. From that time on, the upward expansion of the positive vorticity region progresses rapidly, and the nascent dynamic stall vortex cuts off the reversed-flow region from its downstream origins while itself being cut off from its upstream source of negative vorticity (Figure 4.7c). The devel-

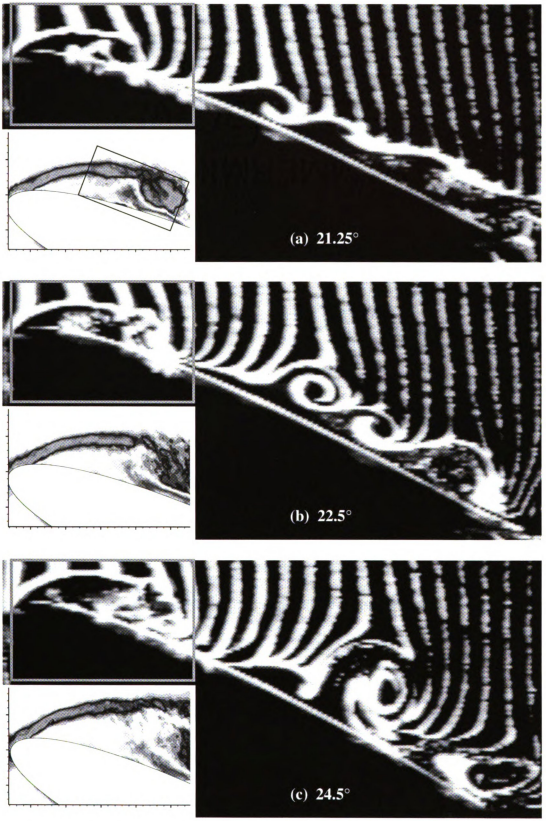

Fig. 4.8: Flow visualizations and vorticity field during the growth and convection of the DSV.

oping suction peak associated with the DSV produces a favorable pressure gradient along a portion of the surface upstream of the vortex. This globally favorable pressure gradient acts like an adverse pressure gradient on the reversed-flow region, and a very thin layer of clockwise (negative) vorticity develops underneath it, producing the three-layer vortical structure which was also seen in the computations of Ghosh Choudhuri, et al. (1994).[141] As this new region of negative vorticity grows slightly, the overlying reversed-flow region grows more, causing an even larger expansion of the separated region over the suction surface. Figure 4.8 documents this growth and the beginning of the convective phase of the dynamic stall vortex.

At this point an in-depth examination of the near-wall velocity and vorticity fields will help us determine where, when, and why leading-edge separation occurs. The small black rectangles overlaid on the vorticity contours of Figures 4.7 and 4.8 delimit the regions which are displayed in the velocity, vorticity, and streamline plots of the next two figures.

Figure 4.9 depicts the developments in the velocity field and the corresponding vorticity, streamline, and U_{tan} fields during the process of leading-edge separation. Data in this figure are in the rotating frame of reference attached to the airfoil, so the surface velocity is zero everywhere. Additionally, two out of every three vectors in the ξ-direction are skipped to improve the clarity of the presentation. The lightest orange contour in Figures 4.9 and 4.10 indicates the presence of reversed flow ($-0.1 \le U_{tan}/U_\infty < 0$), while a white contour indicates the converse ($0 \le U_{tan}/U_\infty < 0.1$). A small sketch at the top of each figure indicates where these results are located with respect to the overall leading-edge flow field.

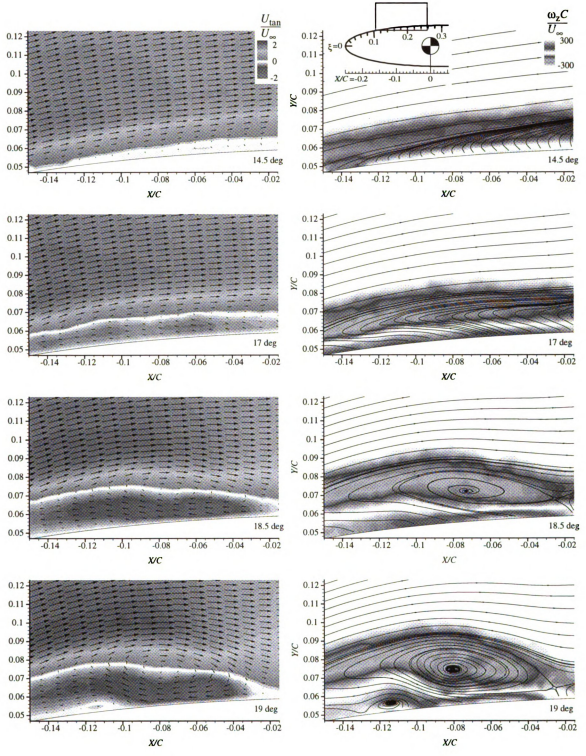

Fig. 4.9: Velocity vectors, tangential velocity and vorticity contours, plus streamline patterns during the initial stages of leading-edge separation. One third of the available vectors are shown.

The views in Figure 4.9 are magnified when compared to the vorticity plots shown in the previous two figures. These enlarged views reveal that the reversed-flow front has progressed to $X/C = -0.1$ by $\alpha = 14.5°$. Recalling that the first regularized measurement location is $3c$ (i.e., $3 \times 10^{-3}C$) above the airfoil surface, this observation actually implies only that a $3c$-thick region of reversed flow exists over the suction surface for $X/C \geq -0.1$. Similar care must also be exercised when interpreting streamline patterns. The placement of a streamline is affected both by the lack of data between the surface and $\eta = 3c$, as well as by the increasing uncertainty in the direction of a measured velocity vector when its magnitude approaches zero (see page 92). In the rotating frame of reference, streamlines can only intersect the surface at critical points, but without data in the very near-wall region, a reliable streamline cannot be computed below $\eta = 3c$. Furthermore, flow features smaller than the grid spacing cannot be detected except under the most unusual circumstances.

The velocity profiles in Figure 4.9 show a continual increase in the velocity overshoot above the boundary layer until the DSV starts to form. Flow visualizations indicate that leading-edge separation begins at an angle of attack $\alpha = 18.5°$ (see Figure 4.7b). In Figure 4.9 it can also be seen that the reversed-flow region is about $15c$ thick at that angle of attack, with a peak reversed-flow magnitude of approximately $U_{tan}/U_\infty = -1$. It should be noted that such a powerful flow reversal so close to the wall generates positive vorticity whose magnitude is measured to be over 300 in dimensionless form, which is as strong as the negative vorticity produced at the leading edge!

Once the reversed-flow front has advanced from the trailing edge past the pitch axis, two critical points are located in the vicinity of the leading edge: a half saddle at the

stagnation point on the pressure surface and a half saddle at the upstream-most location of the reversed-flow region on the suction surface. An exhaustive analysis of streamlines in the experimental flow field indicates that no new critical points are detected within our resolution limit until $\alpha = 17.75°$, at which point a focus is seen at the center of a new closed recirculating region (called the primary recirculating region by Ghosh Choudhuri, et al., 1994[40]) that ultimately grows into the dynamic stall vortex. It should be noted that a new saddle develops at the same time as the new focus. This saddle is on the boundary of the recirculation region, and it moves rapidly downstream as the region grows. By 18.5° the focus is at the center of an ellipsoidal region $80c \times 20c$ in size, and the effects of the proto-DSV are apparent in the flow visualizations as noted in the preceding paragraph. A second focus and two new half saddles are detected when $\alpha = 19°$, at which time the streamwise extent of the third layer of vorticity is about $18c$ while its maximum vertical extent is slightly greater than $3c$. This new focus forms the center of the secondary recirculation region, which is initially bounded by a streamline passing through the two critical points at the wall.

The angle of attack changes by 1.25° between the appearance of the first and second foci. A third focus appears very shortly thereafter ($\Delta\alpha = 0.25°$), and its inception is captured in the uppermost streamline plot of Figure 4.10. While the dynamic stall vortex is developing, its circulation continues to increase because of an accumulation of vorticity from the leading-edge region. The rapid growth of the tertiary recirculating region, accompanied by the continued expansion of the secondary region, severs the DSV from its feeding vortex sheet around $\alpha = 20°$, at which time the center of the DSV is seen to start moving downstream. This accumulation of vorticity is discussed on the basis of the vor-

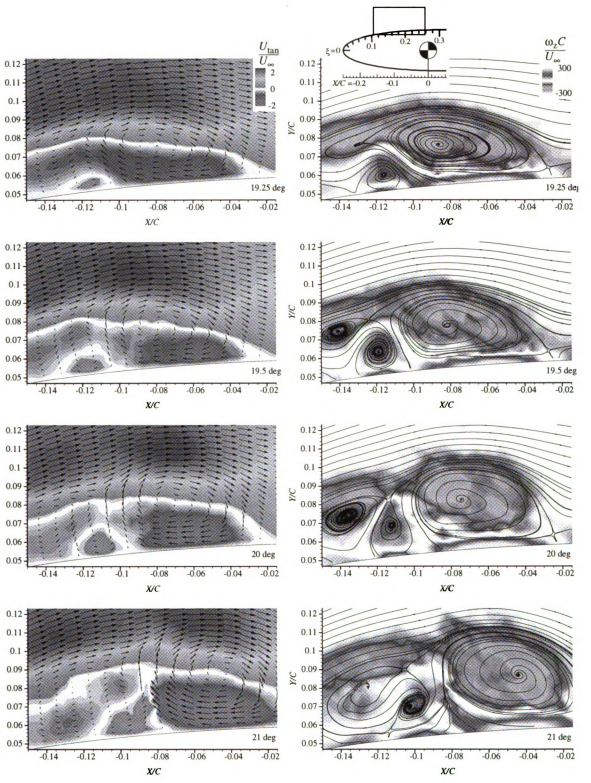

Fig. 4.10: Velocity vectors, tangential velocity and vorticity contours, plus streamline patterns during the growth and initial convection of the DSV. One third of the available vectors are shown.

ticity flux plot which is presented next.

Following the notation of Reynolds and Carr (1985)[103], we define the non-dimensional convective flux of vorticity through a line normal to the surface to be:

$$F \equiv \frac{C}{U_\infty^2}\int_0^\delta U_{\tan}\omega_z d\eta \tag{21}$$

Although vorticity is being generated at the surface because of the pressure gradients in the flow field, Reynolds and Carr[103] argue that the diffusion of this vorticity away from the surface takes place over a much longer time scale than the convective transport of vorticity for rapidly developing events. During the leading-edge separation process, $\Delta\alpha = 1.25°$ corresponds to $\Delta\tau = 0.16$ for this pitch rate, which suggests that the vorticity flux is indeed dominated by the convective terms.

Figure 4.11 illustrates the convective vorticity flux above the suction surface for

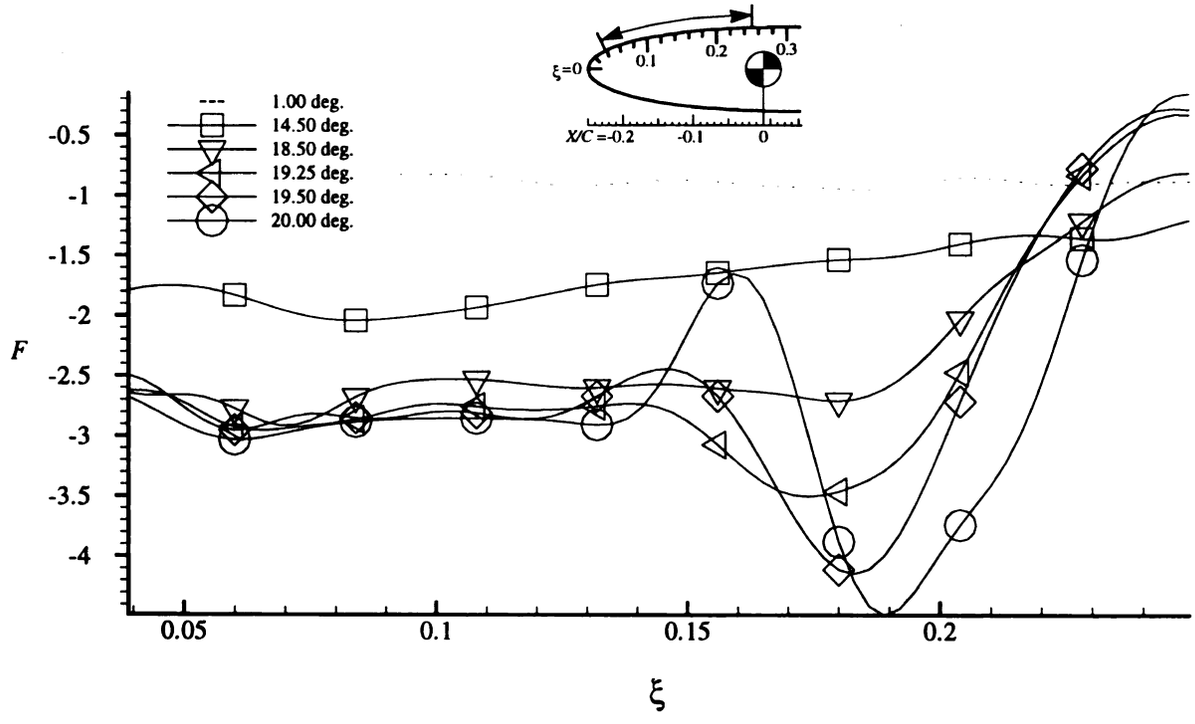

Fig. 4.11: Convective vorticity flux above the suction surface through the onset of leading-edge separation.

six different angles of attack bracketing the onset of leading-edge separation. (Symbols are shown every 9th data point to aid in discriminating the lines from one another.) As the angle of attack increases, the magnitude of the "average" vorticity flux also increases, corresponding to the higher levels of vorticity being generated upstream. A decrease in the magnitude of the vorticity flux from one point to the next indicates that vorticity is accumulating in that region; this is seen as a local minimum in the F versus ξ plot. A gradual accumulation can be seen, for example, over most of the suction surface for $\alpha = 14.5°$. A more abrupt decrease in vorticity flux is seen for $\alpha = 18.5°$ and $\xi \geq 0.18$ ($X/C \geq -0.09$), which is just upstream of the developing dynamic stall vortex, see Figure 4.9. As the center of the DSV moves forward and the vortex grows in strength, so does the location and magnitude of the negative peak in Figure 4.11, e.g., for $\alpha = 19.25°$. Other local maxima and minima in the vorticity flux at later angles are caused by the effects of vorticity accumulation in the secondary and tertiary recirculating regions.

4.4. Computations of the $\Omega^* = 0.1$ Flow Field

In this section we compare our computational results for the $\Omega^* = 0.1$ pitch rate with our experimental data and with the computations of Ghosh Choudhuri, et al. (1994).[141] The resolution limit of the data comprises an important consideration in these comparisons, so it is discussed first. It will then be shown that our computational results are practically identical with those previously published,[141] whereas significant differences exist between conclusions based on those computations versus those derived from the experiments. A model is proposed to explain the source of those differences.

As discussed in Chapter 3, the computational grid used in our study has 203 points in the ξ-direction and 101 points in the η-direction. The spacing between adjacent grid nodes varies along the surface, as well as in the surface normal direction; specifics are shown in Figure 4.12. Compared to the regularized experimental measurement density, many more computational grid points are present in the very near-wall region, which enables features with a smaller extent in the η-direction to be detected.

This concept is easily illustrated on the basis of streamline plots derived from our computational data set at $\alpha = 14.5°$, the angle at which we first see the focus that later develops into the dynamic stall vortex. In Figure 4.13 the green lines denote the computational or experimental mesh, black arrows are individual velocity vectors, and continuous black lines indicate streamlines. As opposed to every other figure in this work, the x- and y-axes are scaled independently in Figure 4.13 (the ratio of the scale factors is approximately 10:1), which allows us to more clearly study the details of this velocity field. Figure 4.13(a) shows the velocities as they were originally computed, while Figure 4.13(b) depicts the near-wall velocity field after it has been remapped onto the regularized mea-

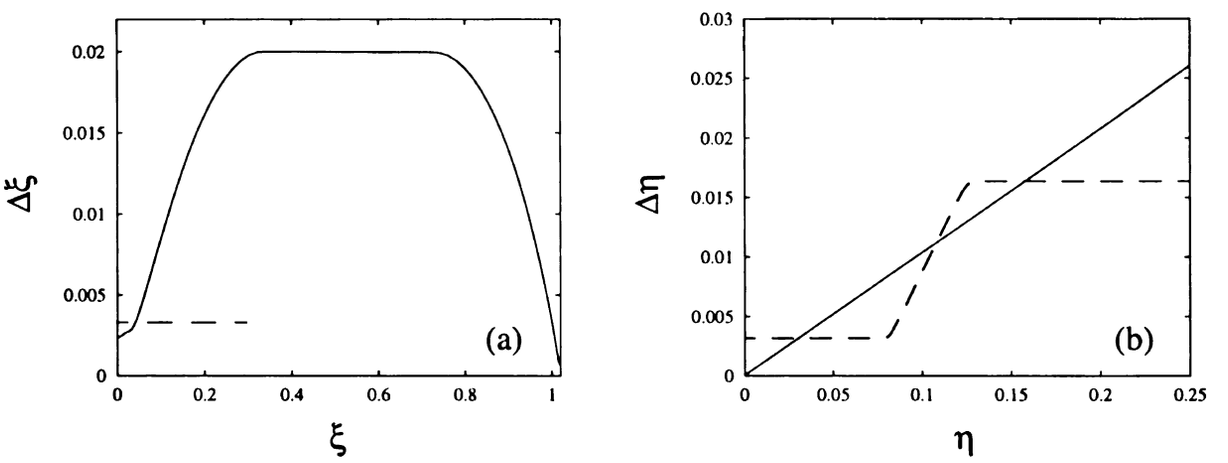

Fig. 4.12: Computational grid spacings (a) along the airfoil surface, and (b) in the η-direction within a quarter chord of the surface. Dashed lines indicate the corresponding experimental grid sizes.

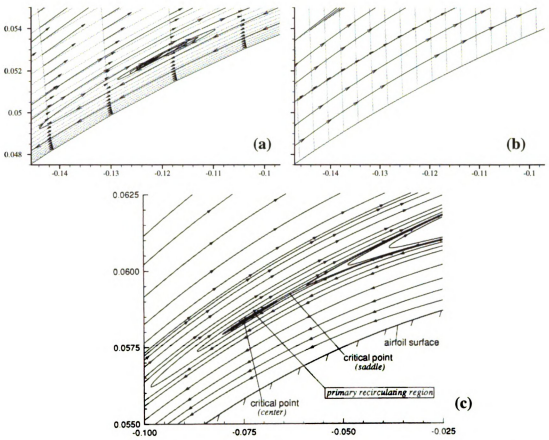

Fig. 4.13: (a, b) Streamline patterns for $\alpha = 14.5°$ based (a) the velocity field as originally computed and (b) the computed velocity field after it has been remapped onto the regularized measurement grid. (c) Computational results from ref. 40 at $\alpha = 15.01°$. In all of these plots, the x-axis scale is approximately 10 times the y-axis scale.

surement grid via bi-linear interpolation. In this region the experimental grid is approximately four times finer in the ξ-direction but 15 times more coarse in the η-direction when compared to the computational grid. Consequently no hint is seen in Figure 4.13(b) of the flow reversal and recirculating region which are shown so clearly in Figure 4.13(a).

When comparing our experiments and computations, small near-wall features which are seen in the computations but not the experiments might in fact be present in both. This condition, therefore, does not indicate an inconsistency between the two data sets. However, the results <u>are</u> contradictory when a feature larger than the coarser grid

spacing is seen in one set of data but not the other. If a contradiction arises because a feature is absent in the experimental results, it is either a consequence of that feature not being present in the flow field, or because that feature is not present in a consistent enough fashion to be captured by the regularization process described in Chapter 2. On the other hand, if a "large" feature exists in the phase-averaged experimental results but not the computations, it indicates a potential validation problem for this particular computational solution which might be caused by factors such as the grid resolution, damping levels, Mach or Reynolds number mismatch, etc.

In the study of Ghosh Choudhuri, et al. (1994)[40], a structured C-grid and an unstructured grid were both utilized to study the constant pitch-rate dynamic stall flow field for $\Omega^* = 0.1$. Both methods produced results consistent with one another and with the experimental data available at that time. Since the resolution of the structured grid was finer than that of the unstructured grid, results based on the former are expected to be nominally more accurate. The Mach and Reynolds numbers in that study were 0.2 and 10,000, respectively, and both are comparable to the values of 0.1 and 12,000 used in the present work.

Figures 4.13(a) and (c) present a comparison of their structured grid results with our computations at the inception of the dynamic stall vortex. In both cases the velocity field experiences a flow reversal within a quit thin region near the wall ($\eta \leq 3c$). In our computations this occurs very slightly earlier, farther forward, and closer to the wall, but the subsequent development of this center is practically identical in both studies. Figure 4.14 shows this development through the formation of the secondary recirculating region. In this figure the same range of non-dimensional vorticity values are plotted, $-75 \leq \omega_z \leq 75$

using similar color look-up tables for those values. Two consistent differences can be seen between the topological features of the two studies: closed recirculating regions in our study are flattened out in the η-direction and stretched in the ξ-direction, and the centers

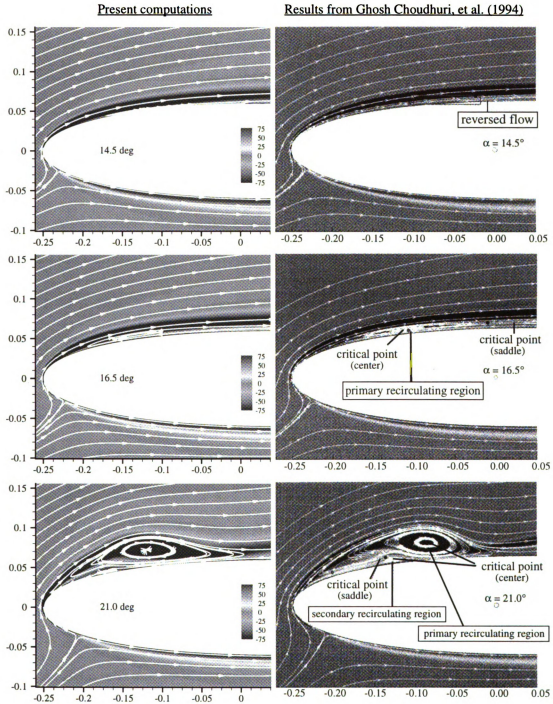

Fig. 4.14: Vorticity contours and streamline patterns from the present computations and the structured-grid results of Ghosh Choudhuri, et al. (1994)[40].

of those regions are located about 20*c* farther upstream, which is roughly equivalent to two grid nodes in that part of our computational domain. The vorticity fields appear to be essentially identical between the two studies, with two caveats: (1) the peak values cannot be observed using this color mapping, and (2) the differences seen in the shapes of the vorticity contours are related to the topological differences noted above. On the basis of these comparisons, we can conclude that the present computations represent the flow field as well as the simulations of Ghosh Choudhuri, et al. (1994)[40], at least through the onset of leading-edge separation.

Since their two different computational approaches produce practically the same results as the present computations, it is tempting to conclude that the computational results have been validated. Nevertheless, the question remains, do the simulations accurately predict what is observed experimentally? The combined computational and experimental flow visualization studies of Gendrich, et al. (1992[37], 1995[38]) showed a 2° to 3° difference between the visually detected onset of leading-edge separation. The measured flow fields discussed earlier in this chapter also show that the dynamic stall vortex not only develops sooner than predicted numerically, it also forms much more rapidly.

Figure 4.15 illuminates the differences between the measured and computed flow fields, beginning with the streamwise expansion of the reversed-flow region and proceeding through the initial stages of leading-edge separation. Angles of attack have been matched as nearly as possible on the basis of the size, strength, and global appearance of the vorticity field. Although the vorticity contours are partially obscured by the streamlines, it can be seen that the vorticity distributions are very similar at the different stages of flow evolution. It should also be noted that the field of view in this figure is larger than it

is in Figures 4.9 and 4.10, so that the relative extent of the computational and experimental flow features can be compared more readily.

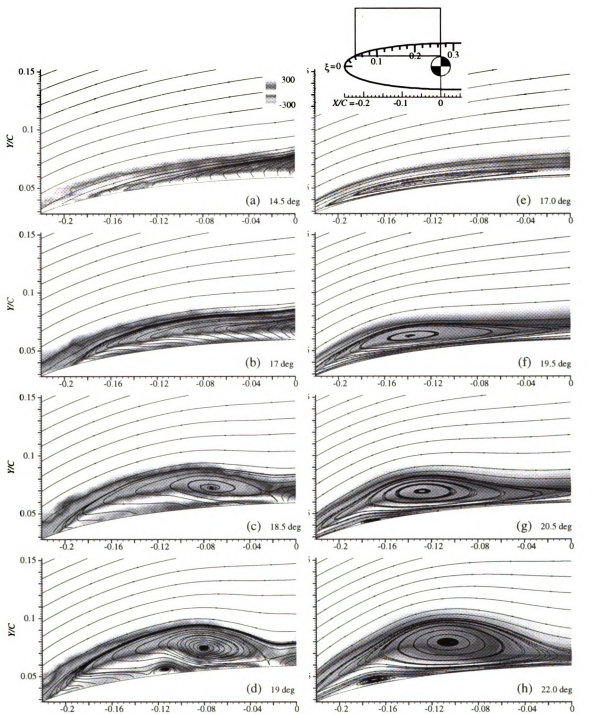

Fig. 4.15: (a-d) Experimental versus (e-h) computational vorticity fields and streamline patterns.

Despite the qualitative similarities in the vorticity field, the topologies of the streamline patterns differ significantly between the simulations and the measurements. In the simulations, the inception of the primary recirculating region occurs when $\alpha = 14.5°$ at a point so close to the wall that its existence cannot be verified on the basis of our experimental data. In fact, the velocity field measurements for that angle of attack do show that the reversed-flow front has expanded significantly toward the leading edge, and it is possible that the computationally observed birth of the DSV is also present at that time in our experiments. However, by $\alpha = 17°$ the computed boundary layer has grown to approximately the same size as we observe experimentally at 14.5°, and the center of the primary region has moved to about $\eta = 6c$, so it should be visible in the experimental streamline pattern. Nonetheless, the inception of the DSV is not observed experimentally until $\alpha = 17.75°$; see Figure 4.16.

The topological development of the experimental dynamic stall vortex shown in Figure 4.16 is the same as that recorded by Ghosh Choudhuri, et al. (1994)[40], i.e., a new node and saddle form in very close proximity to one another. The node moves forward initially, but a short time later, as circulation accumulates in the vortex, the center of the region turns around to head downstream and away from the wall. The saddle which is located at the furthest downstream point of the DSV remains relatively motionless in our experiments until the DSV's convective phase begins, while in all of the simulations that saddle moves rapidly downstream immediately after its formation. Consequently the simulated dynamic stall vortex appears to be more ellipsoidal than the corresponding measured DSV.

The secondary recirculation region plays a key role in separating the DSV from its

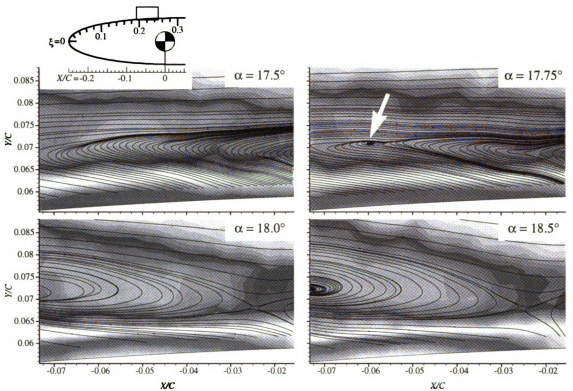

Fig. 4.16: Experimentally observed genesis of the dynamic stall vortex. Vorticity contours have the same scale as in figure 4.15.

feeding vortex sheet, and the abruptness of this region's growth is closely tied to the rapid enlargement of the separated region near the leading edge. More than the relatively slow roll-up of the outer zone of negative vorticity, it is the sudden eruption of the positive vorticity layer which most nearly resembles the boundary layer breakdown process and terminal boundary layer structure proposed by Van Dommelen and Cowley (1990)[124] and Peridier, et al. (1991b)[94].

The expansion rate of the secondary zone differs very widely between experiment and computation. Experimentally the secondary region is observed to double in size between $\alpha = 19°$ and 19.25°, whereas in our simulations its vertical extent increases by only 50% between $\alpha = 20.5°$ and 22°. The tertiary recirculation region is first observed in the computations of Ghosh Choudhuri, et al. (1994)[40] at $\alpha = 20.5°$. The same event

occurs in our simulations at 26.5°, while in our experiments it happens at 19.25°, a bare 0.25° after the birth of the secondary region. Once leading-edge separation begins in our experiments, it progresses quite rapidly; in the simulated flow fields, events happen at a more sedate pace. Table 4 summarizes these findings.

Three related models can be used to provide some insight into the behavior of the DSV and the secondary recirculation region. The simplest model treats the vorticity convecting downstream as a vortex sheet. When perturbed in the surface-normal direction, vortex sheets tend to roll up, with the strength of the interaction depending upon the level of the perturbation. Indications are that the perturbation, whatever its source, is stronger in the experimental flow field than it is in the computations. This might be caused by the finite level of external disturbance sources in the experimental facility, or small disturbances in the simulations may be damped out by the numerical dissipation which is added to increase the stability of the solution algorithm. The vortex-sheet model adequately accounts for the observed roll-up of the shear layer (e.g., Figure 1.2, $\alpha = 21–28°$), but it does not help us to understand why the dynamic stall vortex forms.

Reynolds and Carr (1985)[103] propose a "vortex-train model" to describe the dynamic stall flow field. Their model is based on the behavior of a hypothetical string of

Table 4: Initial angle of attack at which a feature is detected

feature	present study		ref. 40
	experiments	computations	
primary recirculating region	17.75°	14.5°	15°
secondary recirculating region	19°	20.5°	21°
tertiary recirculating region	19.25°	26.5°	22.5°

vortices which are influenced by their image vortices beneath the airfoil surface. The negative-signed vortices convecting downstream have an upstream velocity induced on them by the corresponding image vortex train. As the airfoil pitches up, the developing adverse pressure gradient causes a reduction in the free-potential velocity, allowing the negative vortices to "swim upstream" against the convective current. In the meantime, "vortices formed at the leading edge keep coming relentlessly downstream," so a net accumulation of circulation occurs, enabling the vortices to swim even further upstream, until they encounter the start of the adverse pressure gradient region near the leading edge. Reynolds and Carr[103] suggest that the continuing accumulation of circulation at this time causes a vortex to form and then shed, once its size is approximately equal to the boundary layer thickness. While this model satisfactorily accounts for the accumulation of negative vorticity that leads to the formation of the dynamic stall vortex, it fails to provide an explanation for the behavior of the underlying positive vorticity layer.

Consider once again the response of an individual vortex in Reynolds and Carr's "vortex train." When this vortex experiences a downward perturbation, i.e., toward the airfoil's surface, it moves closer to its image and is subject to an increased induced velocity, so it starts to "swim upstream." As it does so, it accumulates vorticity from the downstream-convecting vortices that it encounters. At this point, while the vortex continues to gain strength and migrate upstream, it looks like Walker's (1978)[134] rectilinear vortex convecting above a wall. The vortex causes an unsteady alteration in the surface pressure distribution, which leads to an eruption of the boundary layer fluid "ahead" or upstream of the vortex core. In this case, the boundary layer fluid that erupts is actually the positive vorticity layer as a result of the reversed-flow region that developed before separation

began. The subsequent growth of the secondary recirculating region forces the dynamic stall vortex away from the wall, and therefore away from its image pair; it cuts off the source of circulation that was feeding the DSV; and as the positive vorticity from the "boundary layer" mixes with the negative vorticity of the DSV, the net circulation in the DSV decreases. This combination of factors causes the induced velocity on the dynamic stall vortex to drop, and it begins to convect downstream instead of "swimming upstream."

The vortex/wall interaction model provides explanations for several of the differences observed between the various sets of results. First it suggests that dynamic stall vortices which are closer to the wall will "swim" further upstream as a consequence of the higher levels of induced velocity. This is exactly what we see: the DSV center is closest to the wall in our computations, followed by the simulations of Ghosh Choudhuri, et al. (1994)[40], then the experimental results; and the DSV develops farthest upstream in our computations, followed in order by the other two sets of data. The vortex is most compact in our experiments, and it produces the strongest boundary-layer response; the least compact vortex core is in our simulations, and it produces the weakest secondary recirculating region. As noted above, the weaker the eruption of positive vorticity, the longer it takes the DSV to separate from its feeding vortex sheet, hence the larger it grows and the later it begins to move downstream. Again, this corresponds to the observed behavior in the three different flow fields under consideration.

To summarize, the velocity, vorticity, and streamline patterns in the early stages of the simulated dynamic-stall process match the experimentally measured flow field to the resolution limit of the data. The computations indicate an initial formation of the DSV which is too small and too close to the wall to verify experimentally, however the experi-

mental observations are not inconsistent with the simulations at that point. As the DSV grows in the computational domain, it becomes flatter and more ellipsoidal than what we observe experimentally. The differences in the location and strength of the dynamic stall vortex alter the intensity of its interaction with the underlying positive vorticity region. The weaker interaction in our computations prolongs the developmental phase of the DSV; this is the source of the 2°–3° delay between the visibly detectable onset of leading-edge separation observed by Gendrich, et al. (1995).[38] The finer resolution grids used by Ghosh Choudhuri, et al. (1994)[40] produced a somewhat more circular DSV than our own computations, suggesting that an adaptively refined grid might yield a DSV whose dynamics more nearly match the experimental flow field.

4.5. Pitch-Rate Effects

As discussed in the introduction, the dynamic stall process is strongly influenced by the pitch rate. In fact, the dynamic effects of the pitch rate are more significant than Reynolds number effects for a wide range of values, which is why low Re_c studies are expected to provide useful insight into the dynamic stall problem. In this section we consider the effects of pitch rate on the computed and measured flow fields. These effects are first documented using the computational vorticity field, followed by plots of the experimental vorticity distribution and streamline patterns. The computations show that although the reversed-flow region develops independently at the leading edge for pitch rates above 0.2, the separation process is only weakly influenced by pitch rates for the range of values considered. The experimental results show the same trends as the compu-

tations: at higher pitch rates, the leading-edge separation process is more compact and develops closer to the leading edge. As with the computations, the experimentally observed interaction is stronger at higher pitch rates, but increased small-scale activity and three-dimensional effects are seen which cannot be simulated by our two-dimensional solver. The reduced repeatability of the flow field at higher pitch rates (see Section 4.1) is seen to have an adverse impact on the results for $\Omega^* = 0.4$ after the onset of leading-edge separation.

Our simulations indicate that the dynamic stall process always begins with a development of a thin reversed-flow region near the leading edge for all of the pitch rates considered in this study. Gendrich, et al. (1995)[38] showed that this region can develop in two different ways, either by an expansion of the reversed-flow front from the trailing edge all the way to the leading-edge region, or by an independent formation process at higher pitch rates ($\Omega^* \geq 0.3$). Figure 4.17 shows the computed vorticity field after the initial development of the reversed-flow region near the leading edge, and as expected because of the higher levels of adverse pressure gradient at the higher pitch rates (Gendrich, et al., 1995[38]), higher levels of vorticity are generated and the reversed-flow front progresses farther forward in those cases. In all other respects the vorticity fields are quite similar at this stage of development.

The spatial scale of the developing dynamic stall vortex is inversely proportional to the pitch rate, as is the distance between the core of the DSV and the wall (see Figure 4.18). Furthermore, the levels of vorticity inside the vortex are significantly higher at the higher pitch rates (note the different scales of vorticity in each part of Figures 4.17-4.19). This combination of factors produces a significantly stronger eruption of the secondary

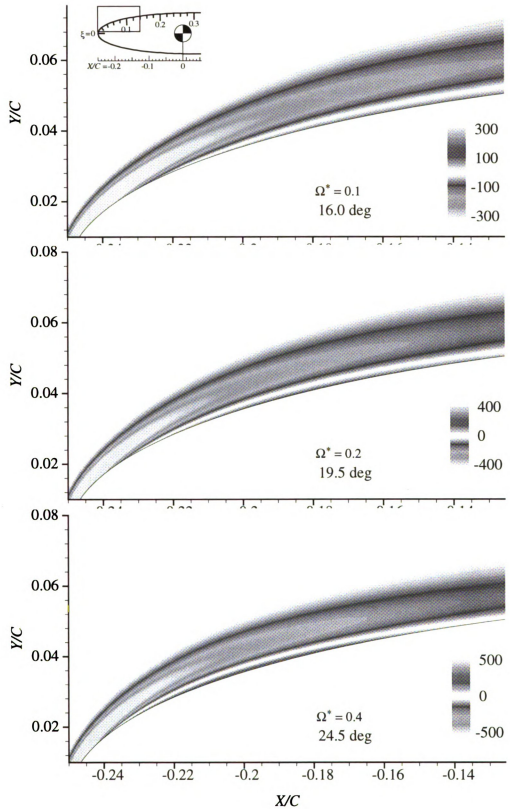

Fig. 4.17: Computed vorticity contours after the development of the reversed-flow region but before the onset of leading-edge separation.

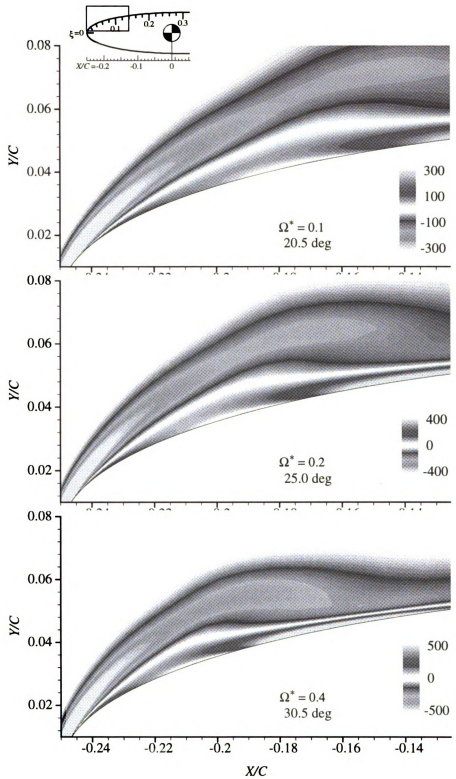

Fig. 4.18: Computed vorticity contours at the formation of the secondary recirculating region.

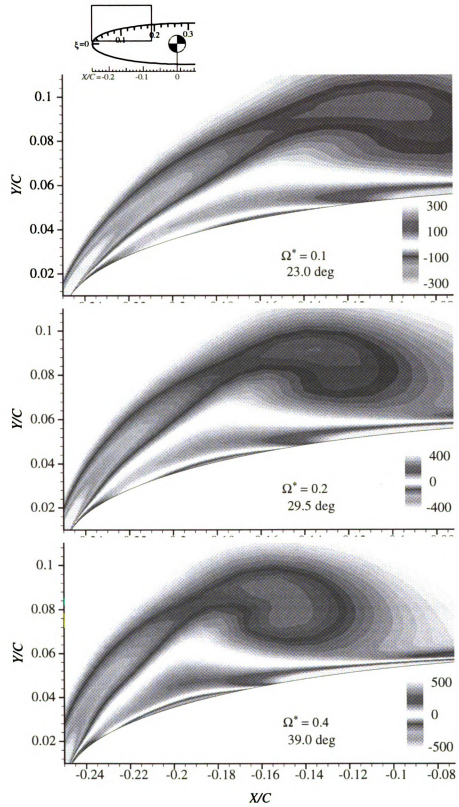

Fig. 4.19: Computed vorticity contours after the onset of leading-edge separation. Vorticity contour levels are the same as in figures 4.17 and 4.18, but a larger field of view is visible in this figure.

recirculating region for higher values of Ω^* as seen in Figure 4.19. These observations are consistent with the unmodified experimental data shown in Section 4.1: at the lower pitch rates in Figure 4.3, the recirculating region which develops into the DSV has a larger extent, and the center of the region is located further downstream.

Figures 4.20-4.23 document the vorticity contours and streamline patterns of the experimental flow field for the three different pitch rates of this study. As with the computational results, different angles of attack have been matched as nearly as possible on the basis of the size, strength, and global appearance of the vorticity field. The spatial scaling is identical in all of these figures, but the plots for each pitch rate focus on the region within which the dynamic stall vortex will develop. The sketches in each figure show the region depicted by the respective plots, and as predicted by the simulations, the dynamic stall process develops closer to the leading edge at higher pitch rates. Note also that the range of vorticity contours is different for $\Omega^* = 0.2$ and 0.4 than it is for $\Omega^* = 0.1$.

As in the simulations, our experimental measurements indicate that the dynamic stall process begins at these pitch rates with the development of a reversed-flow region near the leading edge. Figure 4.20 also shows that the $U_{tan} = 0$ front propagates upstream at the lower pitch rates, while a region of positive vorticity which is independent of the trailing edge forms at $\Omega^* = 0.4$. The experimental results differ from the computations in that an array of small-scale nodes and saddles is seen centered around $\eta = 12c$ for $\Omega^* \geq 0.1$. A short time later (Figure 4.21) the reversed-flow region has grown, and the developing recirculating regions for the higher pitch rates are both larger and farther from the wall, about $\eta = 25c$.

Figure 4.22 depicts the streamline patterns and vorticity contours at the visually

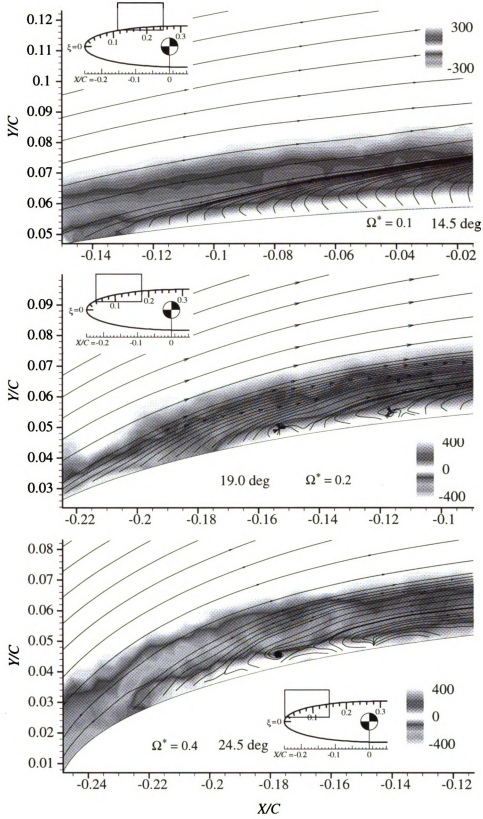

Fig. 4.20: Experimental vorticity field and streamline patters just after the reversed-flow region forms.

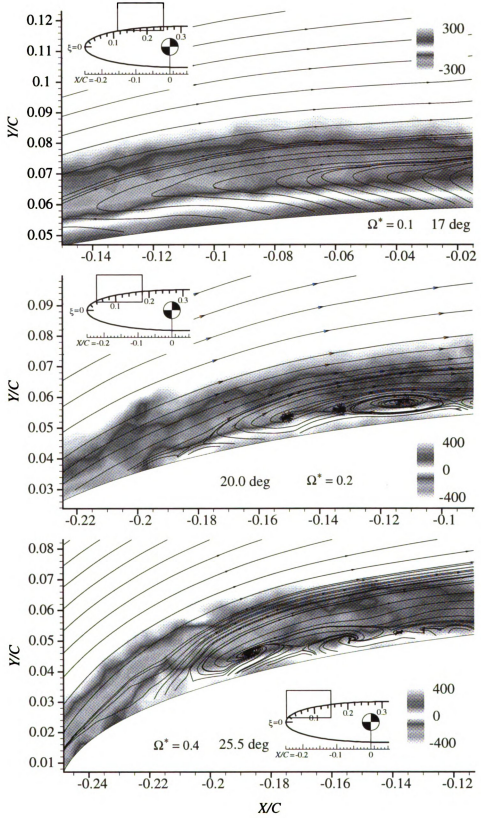

Fig. 4.21: Boundary layer developments just prior to the onset of leading-edge separation.

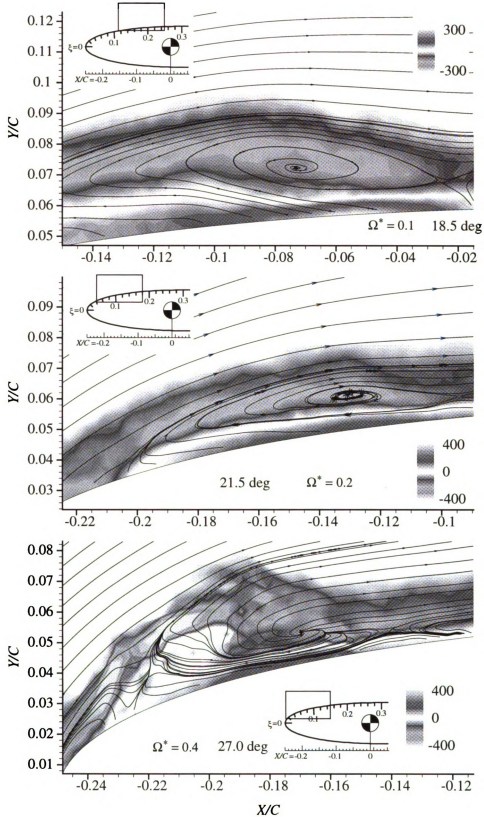

Fig. 4.22: Streamlines and vorticity contours at the visually detected onset of leading-edge separation.

detectable onset of leading-edge separation (Brown, 1992[10]). At this point the higher variability in the $\Omega^* = 0.4$ flow field (discussed in Section 4.1) has caused the phase-averaged results for that pitch rate to be less coherent than they are for the others. The small-scale rotational centers seen for $\Omega^* = 0.2$ have agglomerated into one large vortical structure centered at $x/C = -0.13$. The secondary and tertiary recirculation regions form within 0.25° of each other for that pitch rate, while that process is not visible in the phase-averaged results for $\Omega^* = 0.4$. Figure 4.23 shows the intense eruption of positive vorticity which in both cases severs the DSV from its upstream source of circulation.

The scale of all of these events is very small, with the boundary layer occupying a region less than 40c thick up to the onset of leading-edge separation. The limiting spatial resolution of our measurements almost certainly prevents us from observing the initial formation of the dynamic stall vortex, but there is adequate resolution to detect the reversed-

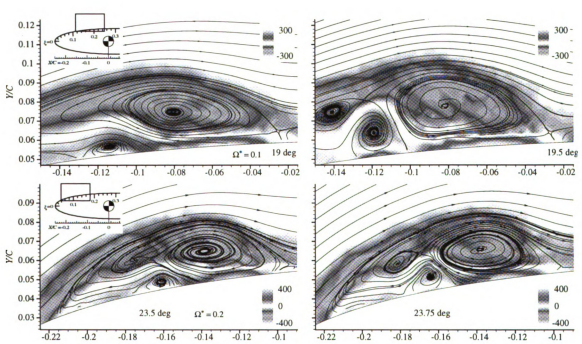

Fig. 4.23: Formation of the secondary and tertiary recirculation regions (not observed for $\Omega^* = 0.4$).

flow front and the three layers of vorticity which have previously been detected only in simulations. The results of Oshima and Ramaprian (1997),[92] shown in FIgure 4.24, have a resolution limit of 2.4 mm, which in their experiments is approximately 16c. While they observe the same global features as seen in the present study, it is probable that they lack the spatial resolution necessary to detect the reversed-flow developments which precedes the onset of leading-edge separation according to our observations. As a result, they conclude that such a flow reversal is not a significant factor in the development of the dynamic stall flow field, in contradiction of what is seen in the present work and the previously cited works of other researchers.

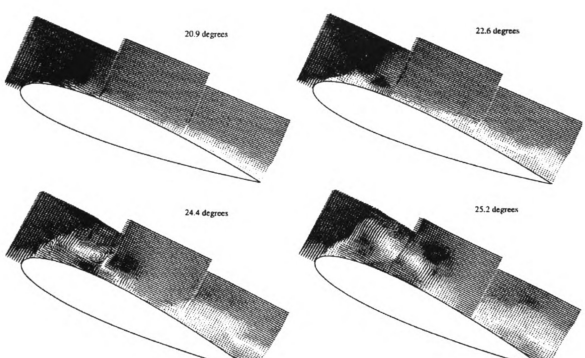

Fig. 4.24: Experimental results from Oshima and Ramaprian (1997)[92].

Chapter 5

CONCLUSIONS AND FUTURE WORK

This work comprises a joint computational and experimental study of the constant pitch-rate dynamic stall process. Since previous studies have indicated that the effects of pitch rate are much greater than Mach or Reynolds number effects, the behavior of a low-Reynolds number flow field was investigated. This eased the difficulties associated with high-speed flow visualization and measurements, reduced numerical resolution requirements, and eliminated the need to incorporate turbulence effects into the computational model. In particular, we presented boundary-layer resolved experiments and computations of an NACA 0012 airfoil in a Re_c = 12,000 flow pitching about the quarter chord at rates in the range $0.1 \leq \Omega^* \leq 0.4$. This is the first time that the inception of the dynamic stall vortex has ever been captured experimentally, and results indicate that the flow near the leading edge does indeed have a strong impact on the dynamic stall flow field development and controllability.

Irregularly spaced data from over 1,000 realizations of the experiment were combined onto a regularly spaced grid by using the airfoil's measured angle of attack for synchronization. In the critical region near the leading edge, the regularized measurements are spaced $0.003C$ ($3c$) apart, which is a spatial resolution over five times better than previous experiments. Data were acquired frequently enough so that the regularized results

could be computed every 0.25°, which is at least four times better than previously reported results.

The two-camera Molecular Tagging Velocimetry (MTV) technique was used to make these measurements in a non-intrusive fashion. Although the use of a molecular-based technique introduced some additional complexity into the experiment, it also made it possible for the measurements to simultaneously resolve the boundary layer and free stream in the fairly three-dimensional flow field of an unsteady separation event. It also eliminated many of the experimental uncertainties associated with using particle-based techniques such as Particle Image Velocimetry (PIV) to measure this flow field.

The laser beam grid patterns generated in these experiments utilized the beam blocker method first presented by Gendrich, Koochesfahani, and Nocera (1994 and 1997).[35,36] In addition, the aspect ratio of the laser beam was manipulated using a pair of cylindrical lenses, mounted on translation stages so that the distance between the lenses could be adjusted. In this way it was possible to ensure that the depth of the measurement volume was small relative to the cameras' depth of field, so the tagged regions were always in focus during each experiment.

The correlation procedure described in Chapter 2 was implemented so that sequences of image pairs could be processed automatically. Using a variety of algorithms, the program selected source windows centered on regions with sufficient spatial intensity gradients to produce valid velocity vectors. The velocity vector field found at one time step was used as a guide for the selection of roam windows at the next time step, and processing times were reduced by automatically shrinking the roam window size when this prior information was available. The relative alignment of the two cameras was taken into

account in a very precise and accurate manner, which introduced less than 0.02 pixels of error into each velocity measurement. The effects of blurring which occurred during an exposure were eliminated by setting the exposure time to be the same for each camera. Therefore the overall accuracy of each measurement was typically better than ±0.1 pixel, while the maximum velocity vector magnitude ranged between 15 and 45 pixels, depending on pitch rate.

The dynamic-stall flow field was also investigated computationally using a two-dimensional, fully compressible, approximately factored Navier-Stokes solver. The unsteady flow field was simulated for the three pitch rates discussed in this study, $\Omega^* = 0.1, 0.2$, and 0.4. For all of these pitch rates, leading edge separation began after the initial acceleration period had ended; no cases were presented for which the airfoil was still accelerating at the onset of leading edge separation.

The present computations were well-validated against the previously available experimental data, as well as against other codes, grid toplogies, and computational methods. The computational results of the present study, in addition to the higher resolution simulations of Ghosh Choudhuri, et al. (1994), reproduced the integrated loads and experimentally observed large-scale features of the flow field reasonably well, but none of the computations were sufficiently well-resolved to capture the size, shape, location, and abruptness of the topological developments which take place during the leading-edge unsteady separation process.

Furthermore, Ghosh Choudhuri, et al. (1994) suggested that "the use of different numerical algorithms provides a stringent examination of the accuracy of the computations." The present study provides one concrete instance where this is not the case. In

fact, all of the computational results considered in this study were only accurate with respect to the sorts of experimental results against which they had been validated, e.g., integrated loads like lift, drag, and moment. In general the comparison of one computation against another will not be a good indication of how well either simulation resolves dynamical elements of the problem which have not yet been quantified experimentally. In particular, there was nothing about any past simulation which indicated that the streamwise grid spacing near the nose must be no more than $3c$ before a numerical study will be able to resolve the inception, growth, and development of the DSV for the pitch rates considered in this study.

Previous results from many researchers had suggested that two different processes characterize the onset of leading-edge separation at high and low pitch rates. At low pitch rates, the onset of leading-edge separation is seen to occur after the reversed flow front originating at the trailing edge has reached the leading edge. This process has been referred to as "trailing-edge stall." At higher pitch rates, the two reversed-flow regions are seen to develop independently, and leading-edge separation occurrs without the reversed flow front from the trailing edge having ever reached the leading-edge region. This process has been called "leading-edge stall," and the present computations indicated that the boundary between leading- and trailing-edge stall is approximately $\Omega^* = 0.2$.

Although it has been suggested that other global differences should be observed in the flow field evolution of these two regimes, the experimental and computational results of the present study indicate that this is not the case. The lift, drag, and moment coefficients do not appear to be influenced by the presence of the thin reversed-flow region. Significant changes in lift, drag, and moment profiles are not seen until the dynamic stall

vortex has formed and begun to convect downstream. Near the surface, the development of the reversed-flow region is an essential precursor to the formation of the dynamic stall vortex, and that flow reversal is caused by the presence of a strong adverse pressure gradient. At higher pitch rates the pressure gradient is stronger and more localized, so that the flow reversal itself is a local phenomenon, while in other cases the entire boundary layer becomes detached from the suction surface. In either case it is the presence of the detached shear layer that leads to the local accumulation of vorticity which grows into the dynamic stall vortex. In that sense, every dynamic stall event is the result of a "leading-edge stall" process.

Another challenge addressed by this study was to determine the size and location of the separated region in the dynamic stall flow field. It was previously suggested that the Moore-Rott-Sears criterion was the most suitable method for locating where and when unsteady separation occurs, and the MRS point would indicate the most upstream limit of the separated region. In keeping with previous studies, we examined the streamline and shear fields computed in the non-inertial frame of reference rotating with the airfoil. Our experimental and computational results agree with previously published simulations which indicate that MRS points do not exist in the dynamic stall flow field, if this is the correct frame of reference. Future work will consider whether a rotationally accelerating frame more nearly approximates the frame of reference moving with the separation, in which case MRS points may be found in this flow field.

While the streamline topology is strongly influenced by the frame of reference, the vorticity field associated with the dynamic stall process varies only slightly when changing from a fixed to a rotational frame. Therefore a consideration of the vorticity field will

lead to more unambiguous results, at least as far as the frame of reference is concerned. In the future, we will analyze the unsteady flux of vorticity to locate regions of local vorticity accumulation. In addition, the formation of regions containing opposite-signed vorticity will be carefully analyzed with respect to the development of the dynamic stall vortex and breakdown of the boundary layer.

REFERENCES

1. Abrahamson, S. and Lonnes, S. (1995) Uncertainty in calculating vorticity from 2D velocity fields using circulation and least-squares approaches. *Exp. Fluids* **20**(1): 10-20.

2. Acharya, M. and Metwally, M. H. (1990) Evolution of the Unsteady Pressure Field and Vorticity Production at the Surface of a Pitching Airfoil. **AIAA 90-1472.**

3. Adrian, R. J. (1991) Particle-Imaging Techniques for Experimental Fluid Mechanics. *Ann. Rev. Fluid Mech.* **23**: 261-304.

4. Alrefai, M. and Acharya, M. (1996) Controlled Leading-Edge Suction for Management of Unsteady Separation over Pitching Airfoils. *AIAA J.* **34**(11): 2327-2336.

5. Baldwin, B. S. and Barth, T. J. (1990) A One-Equation Turbulence Transport Model for High Reynolds Number Wall-Bounded Flows. **NASA TM-102847.**

6. Baldwin, B. S. and Lomax, H. (1978) Thin Layer Approximation and Algebraic Model for Separated Turbulent Flows. **AIAA 78-257.**

7. Beam, R. M. and Warming, R. F. (1978) An implicit factored scheme for the compressible Navier-Stokes equations. *AIAA J.* **16**(4): 130-140.

8. Beyers, Martin E. (1995) Interpretation of Experimental High-Alpha Aerodynamics — Implications for Flight Prediction. *J. Aircraft* **32**(2): 247-261.

9. Biage, M., Harris, S. R., Lempert, W. R., and Smits, A. J. (1996) Quantitative velocity measurements in turbulent Taylor-Couette flow by PHANTOMM flow tagging. *Proceedings of the Eighth International Symposium on Applications of Laser Techniques to Fluid Mechanics*, Lisbon, Portugal, July 8-11, 1996, 15.4.1-15.4.8.

10. Brown, T. A. (1992) Effects of motion history on leading edge separation for an airfoil pitching to large angles of attack. *M. S. Thesis, Dept. Mech. Egr., Michigan State University.*

11. Carr. L. W. and McAlister, K. W. (1983) The Effect of a Leading-Edge Slat on the Dynamic Stall of an Oscillating Airfoil. **AIAA 83-2533.**

12. Carr, L. W. (1988) Progress in analysis and prediction of dynamic stall. *J. Aircraft* **25**(1): 6-17.

13. Cassel, K. W., Smith, F. T., and Walker, J. D. A. (1996) The onset of instability in unsteady boundary-layer separation. *J. Fluid Mech.* **315**: 223-256.

14. Cebeci, T., Hefazi, H., Roknaldin, F., and Carr, L. W. (1995) Predicting Stall and Post-Stall Behavior of Airfoils at Low Mach Numbers. *AIAA J.* **33**(4): 595-602.

15. Chandrasekhara, M. S., Carr, L. W., and Wilder, M. C. (1993) Interferometric Investigations of Compressible Dynamic Stall Over a Transiently Pitching Airfoil. **AIAA 93-0211.**

16. Chu, C. C. and Liao, Y. Y. (1992) A quantitative study of the flow around an impulsively started circular cylinder. *Exp. Fluids* **13**(2/3): 137-146.

17. Chu, C. C., Wang, C. T., and Hsieh, C. S. (1993) An experimental investigation of vortex motions near surfaces. *Phys. Fluids A* **5**(3): 662-676.

18. Cohn, R. K., Gendrich, C. P., MacKinnon, C. G., and Koochesfahani, M. M. (1995) Crossflow Velocity Measurements in a Wake Flow. *Bull. Am. Phy. Soc.* **40**(12): 1962.

19. Conger, R. N. and Ramaprian, B. R. (1994) Pressure Measurements on a Pitching Airfoil in a Water Channel. *AIAA J.* **32**(1): 108-115.

20. Currier, J. M. and Fung, K.-Y. (1992) Analysis of the Onset of Dynamic Stall. *AIAA J.* **30**(10): 2469-2477.

21. D'Arco, A., Charmet, J. C., and Cloitre, M. (1982) Nouvelle technique de marquage d'écoulement par utilisation de molécules photochromes. *Rev. Phys. Appl.* **17**(2): 89-93.

22. Davey, A. (1961) Boundary layer flow at a point of attachment. *J. Fluid Mech.* **10**: 593-610.

23. Degani, D. and Marcus, S. W. (1997) Thin vs. Full Navier-Stokes Computation for High-Angle-of-Attack Aerodynamics. *AIAA J.* **35**(3): 565-567.

24. Doligalski, T. L., Smith, C. R., and Walker, J. D. A. (1994) Vortex Interactions with Walls. *Ann. Rev. Fluid Mech.* **26**: 573-616.

25. Douglas, P., Enos, R. D., Azzopardi, B., and Hope, C. B. (1991) Characterisation of a photochromic triarylmethane dye sulphite and its application to the visualisation of water flows. *7th Int'l Topical Meeting on Photoacoustic and Photothermal Phenomena*, The Netherlands, August, 1991.

26. Ekaterinaris, J. A. (1995) Numerical Investigation of Dynamic Stall of an Oscillating Wing. *AIAA J.* **33**(10): 1803-1808.

27. Ekaterinaris, J. A. and Menter, F. R. (1994) Computation of Oscillating Airfoil Flows with One- and Two-Equation Turbulence Models. *AIAA J.* **32**(12): 2359-2365.

28. Elliott, J. W., Cowley, S. J., and Smith, F. T. (1983) Breakdown of boundary layers: (i) on moving surfaces; (ii) in semi-similar unsteady flow; (iii) in fully unsteady flow. *Geophys. Astrophys. Fluid Dyn.* **25**: 77-138.

29. Elliott, J. W. and Smith, F. T. (1987) Dynamic stall due to unsteady marginal separation. *J. Fluid Mech.* **179**: 489-512.

30. Falco, R. E. and Chu, C. C. (1987) Measurement of two-dimensional fluid dynamic quantities using a photochromic grid tracing technique. *SPIE* **814**: 706-710.

31. Fincham, A. M. and Spedding, G. R. (1995) Velocity bandwidth, discretization errors and peak-locking phenomena in DPIV measurements. *Bull. Am. Phy. Soc.* **40**(12): 2000.

32. Francis, M. S. and Keesee, J. S. (1985) Airfoil dynamic stall performance with large-amplitude motions. *AIAA J.* **23**(11): 1653-1659.

33. Gendrich, C. P., Bohl, D. G., and Koochesfahani, M. M. (1997) Whole-Field Measurements of Unsteady Separation in a Vortex Ring/Wall Interaction. **AIAA 97-1780.**

34. Gendrich, C. P. and Koochesfahani, M. M. (1996) A spatial correlation technique for estimating velocity fields using Molecular Tagging Velocimetry (MTV). *Exp. Fluids* **22**(1): 67-77.

35. Gendrich, C. P., Koochesfahani, M. M. and Nocera, D. G. (1994) Analysis of molecular tagging velocimetry images for obtaining simultaneous multi-point velocity vectors. *Bull. Am. Phy. Soc.* **39**(9): 1980.

36. Gendrich, C. P., Koochesfahani, M. M., and Nocera, D. G. (1997) Molecular tagging velocimetry and other novel applications of a new phosphorescent supramolecule. *Exp. Fluids* **23**(5): 361-372.

37. Gendrich, C. P., Koochesfahani, M. M., and Visbal, M. R. (1992) The visual and vortical signature of leading edge separation. *Bull. Am. Phy. Soc.* **37**(8): 1992.

38. Gendrich, C. P., Koochesfahani, M. M., and Visbal, M. R. (1995) Effects of Initial Acceleration on the Flow Field Development Around Rapidly Pitching Airfoils. *J. Fluids Eng.* **117**(3): 45-49.

39. Ghia, K. N., Yang, J., Osswald, G. A., and Ghia, U. (1991) Study of Dynamic Stall Mechanism Using Simulation of Two-Dimensional Unsteady Navier-Stokes Equations. **AIAA 91-0546.**

40. Ghosh Choudhuri, P., Knight, D. D., and Visbal, M. R. (1994) Two-Dimensional Unsteady Leading-Edge Separation on a Pitching Airfoil. *AIAA J.* **32**(4): 673-681.

41. Graham, G. M. and Strickland, J. H. (1986) An experimental investigation of an airfoil pitching at moderate to high rates to large angles of attack. **AIAA 86-0008.**

42. Green, R. B., Galbraith, R. A. McD., and Niven, A. J. (1992) Measurements of the dynamic stall vortex convection speed. *Aeronautical J.* **96**(10): 319-325.

43. Haralick, R. M. and Shapiro, L. G. (1993) *Computer and Robot Vision*, vol. 2. Addison-Wesley: 597.

44. Harris, S. R., Lempert, W. R., Hersh, L., Burcham, C. L., Saville, A., Miles, R. B., Gee, K., and Haughland, R. P. (1996a) Quantitative measurements on internal circulation in droplets using flow tagging velocimetry, *AIAA J.* **34**(3): 449-454.

45. Harris, S. R., Miles, R. B., and Lempert, W. R. (1996b) Observations of fluid flow produced in a closed cylinder by a rotating lid using the PHANTOMM (Photo-Activated Non Intrusive Tracking of Molecular Motion) flow tagging technique. *Proceedings of the Eighth International Symposium on Applications of Laser Techniques to Fluid Mechanics*, Lisbon, Portugal, July 8-11, 1996, 15.3.1-15.3.9.

46. Hartmann, W. K., Gray, M. H. B., Ponce, A. and Nocera, D. G. (1996) Substrate induced phosphorescence from cyclodextrin · lumophore host-guest complexes. *Inorg. Chim. Acta* **243**: 239-248.

47. Helin, H. E. and Walker, J. M. (1985) Interrelated Effects of Pitch Rate and Pivot Point on Airfoil Dynamic Stall. **AIAA 85-0130**.

48. Hilbert, H. S. and Falco, R. E. (1991) Measurements of flows during scavenging in a two-stroke engine. **SAE 910671**.

49. Hill, R. B. and Klewicki, J. C. (1994) Developments and Applications of Laser Induced Photochemical Anemometry. *ASME Fluid Egr Div.* **191**, Laser Anemometry-1994: Advances and Applications: 209-216.

50. Hill, R. B. and Klewicki, J. C. (1996) Data reduction methods for flow tagging velocity measurements. *Exp. Fluids* **20**(3): 142-152.

51. Huang, H. T., Fiedler, H. E, and Wang, J. J. (1993) Limitation and Improvement of PIV, Part I: Limitation of conventional techniques due to deformation of particle image patterns. *Exp. Fluids* **15**(3): 168-174.

52. Huang, H. T., Fiedler, H. E, and Wang, J. J. (1993) Limitation and Improvement of PIV, Part II: Particle image distortion, a novel technique. *Exp. Fluids* **15**(4/5): 263-273.

53. Huang, R. T. and Lin, C. L. (1995) Vortex Shedding and Shear-Layer Instability of Wing at Low-Reynolds Numbers. *AIAA J.* **33**(8): 1398-1403.

54. Huerre, P. and Monkewitz, P. A. (1990) Local and Global Instabilities in Spatially Developing Flows. *Ann. Rev. Fluid Mech.* **22**: 473-537.

55. Hunt, J. C. R., Abell, C. J., Peterka, J. A., and Woo, H. (1978) Kinematical studies of the flows around free or surface-mounted obstacles; applying topology to flow visualization. *J. Fluid Mech.* **86**: 179-200.

56. Inoue, O. (1981) MRS Criterion for Flow Separation over Moving Walls. *AIAA J.* **19**(9): 1108-1111.

57. Jameson, A., Schmidt, W., and Turkel, E. (1981) Numerical solutions of the Euler equations by finite volume methods using Runge-Kutta time stepping schemes. **AIAA 81-1259**.

58. Jones, W. P. and Launder, B. E. (1972) The Prediction of Laminarization with a Two-Equation Turbulence Model. *Intl. J. Heat and Mass Transfer* **15**(2): 301-314.

59. Jumper, E. J., Dimmick, R. L., and Allaire, A. J. S. (1989) The Effect of Pitch Location on Dynamic Stall. *J. Fluids Eng.* **111**(9): 256-262.

60. Jumper, E. J., Schreck, S. J., and Dimmick, R. L. (1987) Lift-curve characteristics for an airfoil pitching at constant rate. *J. Aircraft* **24**(10): 680-687.

61. Karim, M. A. and Acharya, M. (1991) Development of the Dynamic-Stall Vortex over a Pitching Airfoil. *Bull. Am. Phy. Soc.* **36**.

62. Karim, M. A. and Acharya, M. (1994) Suppression of Dynamic-Stall Vortices over Pitching Airfoils by Leading-Edge Suction. *AIAA J.* **32**(8): 1647-1655.

63. Katz, J. and Walters, R. (1995) Effects of Large Blockage in Wind-Tunnel Testing. *J. Aircraft* **32**(5): 1149-1152.

64. Keane, R. D. and Adrian, R. J. (1992) Theory of cross-correlation analysis of PIV images. *Appl. Sci. Rsch.* **49**(3): 191-215.

65. Ko, S. and McCroskey, W. J. (1997) Computations of Unsteady Separating Flows over an Oscillating Airfoil. *AIAA J.* **35**(7): 1235-1238.

66. Koochesfahani, M. M., Cohn, R. K., Gendrich, C. P., and Nocera, D. G. (1996) Molecular tagging diagnostics for the study of kinematics and mixing in liquid phase flows. *Proceedings of the Eighth International Symposium on Applications of Laser Techniques to Fluid Mechanics.* Lisbon, Portugal, July 8-11: 1.2.1-1.2.12.

67. Koochesfahani, M. M., Gendrich, C. P. and Nocera, D. G. (1993) A new technique for studying the Lagrangian evolution of mixing interfaces in water flows. *Bull. Am. Phy. Soc.* **38**(12): 2287.

68. Koochesfahani, M. M. and Smiljanovski, V. (1993) Initial acceleration effects on flow evolution around airfoils pitching to high angles of attack. *AIAA J.* **31**(8): 1529-1531.

69. Leishman, J. G. (1990) Dynamic stall experiments on the NACA 23012 aerofoil. *Exp. Fluids* **9**(1): 49-58.

70. Leishman, J. G. (1996) Seed Particle Dynamics in Tip Vortex Flows. *J. Aircraft* **33**(4): 823-825.

71. Lempert, W. R., Magee, K., Ronney, P., Gee, K. R., and Haugland, R. P. (1995) Flow tagging velocimetry in incompressible flow using photo-activated nonintrusive tracking of molecular motion (PHANTOMM). *Exp. Fluids* **18**(4): 249-257.

72. Lin, H., Vezza, M., and Galbraith, R. A. McD. (1997) Discrete Vortex Method for Simulating Unsteady Flow Around Pitching Aerofoils. *AIAA J.* **35**(3): 494-499.

73. Lorber, P. F. and Carta, F. O. (1988) Airfoil Dynamic Stall at Constant Pitch Rate and High Reynolds Number. **FJSRL-TR-88-0004**.

74. Lourenco, L. and Krothapalli, A. (1995) On the accuracy of velocity and vorticity measurements with PIV. *Exp. Fluids* **18**(6): 421-428.

75. Lu, L. J. and Smith, C. R. (1985) Image processing of hydrogen bubble visualization for determination of turbulence statistics and bursting characteristics. *Exp Fluids* **3**(6): 349-356.

76. Maas, H. G., Stefanidis, A. and Gruen, A. (1994) Feature tracking in 3-D fluid tomography sequences. *First IEEE Int'l Conf. on Image Processing*, Austin, Texas, Nov. 13-16, 1994.

77. Marvin, J. G. (1995) Perspective on Computational Fluid Dynamics Validation. *AIAA J.* **33**(10): 1778-1787.

78. McAlister, K. W. and Carr, L. W. (1978) Water Tunnel Visualizations of Dynamic Stall. In *Nonsteady Fluid Dynamics*, eds. D. E. Crow and J. A. Miller; ASME Fluids Eng. Div.: 103-110.

79. McCroskey, W. J. (1982) Unsteady airfoils. *Ann. Rev. Fluid Mech.* **14**: 285-311.

80. McCroskey, W. J., Carr, L. W., and McAlister, K. W. (1976) Dynamic Stall Experiments on Oscillating Airfoils. *AIAA J.* **14**(1): 57-63.

81. McCroskey, W. J., McAlister, K. W., Carr, L. W., and Pucci, S. L. (1982) An Experimental Study of Dynamic Stall on Advanced Airfoil Sections. **NASA TM-84245**.

82. McKenzie, R. L. (1993) Progress in Laser Spectroscopic Techniques for Aerodynamic Measurements: An Overview. *AIAA J.* **31**(3): 465-477.

83. Miles, R. Cohen, C., Conners, J., Howard, P., Huang, S., Markovitz, E., and Russel, G. (1987) Velocity Measurements by Vibrational Tagging and Fluorescent Probing of Oxygen. *Optics Letters* **12**(11): 861-863.

84. Miles, R. B., Connors, J. J., Markovitz, E. C., Howard, P. J. and Roth, G. J. (1989) Instantaneous profiles and turbulence statistics of supersonic free shear layers by Raman excitation plus laser-induced electronic fluorescence (Relief) velocity tagging of oxygen. *Exp. Fluids* **8**(1): 17-24.

85. Miles, R. B., Zhou, D., Zhang, B., Lempert, W. R., and She, Z. S. (1993) Fundamental turbulence measurements by Relief flow tagging. *AIAA J* **31**(3): 447-452.

86. Modi, V. J., Sun, J. L. C., Akutsu, T., Lake, P., McMillan, K., Swinton, P. G., and Mullins, D. (1981) Moving-Surface Boundary-Layer Control for Aircraft Operation at High Incidence. *J. Aircraft* **18**(11): 963-968.

87. Moore, F. K. (1958) On the separation of the unsteady laminar boundary layer. In *Boundary Layer Research*, ed. H. Görtler; Springer-Verlag: 296-311.

88. Mortellaro, M. A., Nocera, D. G. (1996) A turn-on for optical sensing. *ChemTech* **26**(2): 17-23.

89. Mueller, T. J., Pohlen, L. J., Conigliaro, P. E., and Jansen, B. J. (1983) The Influence of Free-Stream Disturbances on Low Reynolds Number Airfoil Experiments. *Exp. Fluids* **1**(1): 3-14.

90. Ojha, M., Cobbold, R. S.C., Johnston, K. W., and Hummel, R. (1989) Pulsatile flow through constricted tubes: an experimental investigation using photochromic tracer methods. *J. Fluid Mech.* **203**: 173-197.

91. Okamoto, K., Hassan, Y. A., and Schmidl, W. D. (1995) New tracking algorithm for particle image velocimetry. *Exp. Fluids* **19**(5): 342-347.

92. Oshima, H. and Ramaprian, B. R. (1997) Velocity Measurements over a Pitching Airfoil. *AIAA J.* **35**(1): 119-126.

93. Peridier, V. J., Smith, F. T., and Walker, J. D. A. (1991a) Vortex-induced Boundary-layer Separation. Pt. 1, the Limit Problem Re $\rightarrow \infty$. *J. Fluid Mech.* **232**: 99-131.

94. Peridier, V. J., Smith, F. T., and Walker, J. D. A. (1991b) Vortex-induced Boundary-layer Separation. Pt. 2, Unsteady Interacting Boundary-layer Theory. *J. Fluid Mech.* **232**: 133-165.

95. Perry, A. E. and Chong, M. S. (1987) A Description of Eddying Motions and Flow Patterns Using Critical-Point Concepts. *Ann. Rev. Fluid Mech.* **19**: 125-155.

96. Piziali, R. A. (1994) 2-D and 3-D Oscillating Wing Aerodynamics for a Range of Angles of Attack Including Stall. **NASA TM-4632.**

97. Ponce, A., Wong P. A., Way, J. J., and Nocera, D. G. (1993) Intense Phosphorescence Triggered by Alcohols upon Formation of a Cyclodextrin Ternary Complex. *J. Phys. Chem.* **97**: 11137-11142.

98. Popovich, A. T. and Hummel, R. L. (1967) A new method for non-disturbing turbulent flow measurement very close to a wall. *Chem. Eng. Soc.* **22**(1): 21-25.

99. Prandtl, L. (1904) Über Flüssigkeitsbewegung bei sehr kleiner Reibung. In *Verhandlungen des dritten internationalen Mathematiker-Kongresses, Heidelberg*, Leipzig: 484-491.

100. Press, W. H., Flannery, B. P., Teukolsky, S. A., and Wetterling, W. T. (1988) *Numerical Recipes in C: The Art of Scientific Computing*. Cambridge University Press: 305-309.

101. Raffel, M., Kompenhans, J., and Wernert, P. (1995) Investigation of the unsteady flow velocity field above an airfoil pitching under deep dynamic stall conditions. *Exp. Fluids* **19**(2): 103-111.

102. Reda, D. C. (1991) Observations of Dynamic Stall Phenomena Using Liquid Crystal Coatings. *AIAA J.* **29**(2): 308-310.

103. Reynolds, W. C. and Carr, L. W. (1985) Review of Unsteady, Driven, Separated Flows. **AIAA 85-0527.**

104. Rizzetta, D. P. and Visbal, M. R. (1992) Comparative Numerical Study of Two Turbulence Models for Airfoil Static and Dynamic Stall. **AIAA 92-4649-CP.**

105. Roesgen, T. and Totaro, R. (1995) Two-dimensional on-line particle imaging velocimetry. *Exp. Fluids* **19**(3): 188-193.

106. Ross, S. M. (1987) *Introduction to Probability and Statistics for Engineers and Scientists*. John Wiley and Sons: 44-69.

107. Rott, N. (1956) Unsteady Viscous Flow in the Vicinity of a Stagnation Point. *Quarterly of Appl. Math.* **13**(4): 444-451.

108. Schreck, S. J. and Helin, H. E. (1993) Unsteady Vortex Dynamics and Surface Pressure Topologies on a Pitching Wing. **AIAA 93-0435.**

109. Sears, W. R. (1956) Some Recent Developments in Airfoil Theory. *J. Aeronautical Sci.* **23**(5): 490-499.

110. Sears, W. R. and Telionis, D. P. (1975) Boundary Layer Separation in Unsteady Flow. *SIAM J. Appl. Math.* **28**(1): 215-235.

111. Shen, S.-F. (1978) Unsteady Separation of Three-Dimensional Boundary Layers from the Lagrangian Viewpoint. In *Nonsteady Fluid Dynamics*, eds. D. E. Crow and J. A. Miller; ASME Fluids Eng. Div.: 47-51.

112. Shih, C., Lourenco, L. M., and Krothapalli, A. (1995) Investigation of Flow at Leading and Trailing Edges of Pitching-Up Airfoil. *AIAA J.* **33**(8): 1369-1376.

113. Shih, C., Lourenco, L., Van Dommelen, L., and Krothapalli, A. (1992) Unsteady Flow Past an Airfoil Pitching at a Constant Rate. *AIAA J.* **30**(5): 1153-1161.

114. Smiljanovski, V. (1990) Flow Visualization of the Flow Field of an Airfoil Pitching to Large Angles of Attack. *Diplomarbeit, Dept. Mech. Egr., Michigan State University.*

115. Spalart, P. R. and Allmaras, S. R. (1992) A One-Equation Turbulence Model for Aerodynamic Flows. **AIAA 92-0439.**

116. Spedding, G. R. and Rignot, E. J. M. (1993) Performance analysis and application of grid interpolation techniques for fluid flows. *Exp. Fluids* **15**(6): 417-430.

117. Stier, B. (1994) An Investigation of Fluid Flow During Induction Stroke of a Water Analog Model of an IC Engine Using an Innovative Optical Velocimetry Concept — LIPA. *PhD Dissertation, Dept. Mech. Egr., Michigan State University.*

118. Stier, B., Koochesfahani, M. M., Nocera, D. G. and Schock, H. J. (1995) Molecular tagging velocimetry in gas phase flow. *Bull. Am. Phy. Soc.* **40**(12): 1962.

119. Strickland, J. H. and Graham, G. M. (1986) Dynamic Stall Inception Correlation for Airfoils Undergoing Constant Pitch Rate Motions. *AIAA J.* **24**(1): 678-680.

120. Tang, D. M. and Dowell, E. H. (1995) Experimental Investigation of Three-Dimensional Dynamic Stall Model Oscillating in Pitch. *J. Aircraft* **32**(5): 1062-1071.

121. Thomas, P. J., Bütefisch, K.-A., and Sauerland, K. H. (1993) On the motion of particles in a fluid under the influence of a large velocity gradient. *Exp. Fluids* **14**(1): 42-48.

122. Tokumaru, P. T. and Dimotakis, P. E. (1995) Image correlation velocimetry. *Exp. Fluids* **19**(1): 1-15.

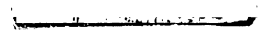

123. Utami, T., Blackwelder, R. F., and Ueno, T. (1991) A cross-correlation technique for velocity field extraction from particulate visualization. *Exp. Fluids* **10**(4): 213-223.

124. Van Dommelen, L. L. and Cowley, S. J. (1990) On the Lagrangian description of boundary-layer separation. Part 1. General Theory. *J. Fluid Mech.* **210**: 593-626.

125. Van Dommelen, L. L. and Shen, S.-F. (1983) An Unsteady Interactive Separation Process. *AIAA J.* **21**(3): 358-362.

126. Van Dyken, R. D., Ekaterinaris, J. A., Chandrasekhara, M. S., and Platzer, M. F. (1996) Analysis of Compressible Light Dynamic Stall Flow at Transitional Reynolds Numbers. *AIAA J.* **34**(7): 1420-1427.

127. Visbal, M. R. (1986a) Calculation of Viscous Transonic Flows About a Transonic Airfoil. **AFWAL-TR-86-3013**.

128. Visbal, M. R. (1986b) Evaluation of an Implicit Navier-Stokes Solver for some Unsteady Separated Flows. **AIAA 86-1053**.

129. Visbal, M. R. (1990a) Dynamic Stall of a Constant-Rate Pitching Airfoil. *J. Aircraft* **27**(5): 400-407.

130. Visbal, M. R. (1990b) On some physical aspects of airfoil dynamic stall. In *ASME Symposium on Non-Steady Fluid Dynamics*, eds. J. A. Miller and D. P. Telionis; ASME Fluids Eng. Div., **92**: 127-147.

131. Visbal, M. R. (1991) On the formation and control of the dynamic stall vortex on a pitching airfoil. **AIAA 91-0006**.

132. Visbal, M. R. and Knight, D. D. (1982) Generation of Orthogonal and Nearly-Orthogonal Boundary-Fitted Coordinates with Direct Control of Grid Spacing. *AIAA J.* **20**(3): 305-306.

133. Visbal, M. R. and Shang, J. S. (1989) Investigation of the flow structures around a rapidly pitching airfoil. *AIAA J.* **27**(8): 1044-1055.

134. Walker, J. D. A. (1978) The boundary layer due to rectilinear vortex. *Proc. R. Soc. Lond. A* **359**: 167-188.

135. Walker, J. D. A. (1987) The impact of a vortex ring on a wall. *J. Fluid Mech.* **181**: 99-140.

136. Walker, J. M., Helin, H. E., and Chou, D. C. (1985) Unsteady Surface Pressure Measurements on a Pitching Airfoil. **AIAA 85-0532**.

137. Westerweel, J. (1994) Efficient detection of spurious vectors in particle image velocimetry data. *Exp. Fluids* **16**(3/4): 236-247.

138. Wilder, M. C., Chandrasekhara, M. S., and Carr. L. W. (1993) Transition Effects on Compressible Dynamic Stall of Transiently Pitching Airfoils. **AIAA 93-2978**.

139. Williams, J. C. (1977) Incompressible Boundary-Layer Separation. *Ann. Rev. Fluid Mech.* **9**: 113-144.

140. Wu, J. C., Wang, C. M., and Tuncer, I. H. (1986) Unsteady Aerodynamics of Rapidly Pitched Airfoils. **AIAA 86-1105**.

141. Yu, H. Y., Lee, S., McAlister, K. W., Tung, C., and Wang. C. M. (1995) Dynamic Stall Control for Advanced Rotorcraft Application. *AIAA J.* **33**(2): 289-295.

142. Yurechko, V. N. and Ryazantsev, Yu. S. (1991) Fluid Motion Investigation by the Photochromic Flow Visualization Technique. *Exp. Thermal and Fluid Sci.* **4**: 273-288.

143. Zeldin, B. A. and Meade, A. J. (1997) Integrating Experimental Data and Mathematical Models in Simulation of Physical Systems. *AIAA J.* **35**(11): 1787-1790.

APPENDIX I

EXPERIMENTAL HARDWARE OPERATIONAL PARAMETERS

This appendix contains specific operational details regarding the cameras and the digital delay generators described in Section 2.3, as well as the airfoil motion controller described in Section 2.6.

Table 5: Xybion ISG-350-GW3 camera switch settings

switch	setting
Fld/Frm	Frm
AGC	off
Pk/Avg	disable

Table 6: Camera control unit (CCU) rear panel switch settings

switch	setting
Trigger Polarity	high-to-low transition
Auto Retrig	disable
Field/Frame	Frame
Composite	H&V

Table 7: Camera control unit (CCU) front panel switch and knob settings

switch or knob	setting
Delay	OFF
Range	10-100 μs
Trig Src	Bypass (Direct)
Camera gain	~ 75%
Camera control	Manual
Slow Gate Duration	50%
Fast Gate Duration	50%
Black level	~ 5%
Gain	(as low as possible)

Table 8: SRS DG535 digital delay generator (DDG) parameter settings.

parameter	value
Trigger	external
trigger threshold	+1.5V
trigger slope	(-)
trigger input termination	high Z
Output T0 load	50Ω
Output AB load	high Z
Output CD load	high Z
all output voltage levels	TTL / Normal
Delay A	T0 + 0.318 μs
Delay B	A + (exposure time)
Delay C	A + Δt; $\Delta t = N \times 63.6$ μs
Delay D	C + (exposure time)
GPIB	<not used>

Table 9: Airfoil motion control parameters

parameter	value
gain (GN)	150
integration constant (KI)	0.25
differentiation constant (KD)	0
zero (ZR)	0.913